Sodium and $T_{1\rho}$ MRI for molecular and diagnostic imaging of articular cartilage[†]

Arijitt Borthakur, Eric Mellon, Sampreet Niyogi, Walter Witschey, J. Bruce Kneeland and Ravinder Reddy*

MMRRCC, Department of Radiology, University of Pennsylvania, Philadelphia, PA 19104-6100, USA

ABSTRACT: In this article, both sodium magnetic resonance (MR) and $T_{1\rho}$ relaxation mapping aimed at measuring molecular changes in cartilage for the diagnostic imaging of osteoarthritis are reviewed. First, an introduction to structure of cartilage, its degeneration in osteoarthritis (OA) and an outline of diagnostic imaging methods in quantifying molecular changes and early diagnostic aspects of cartilage degeneration are described. The sodium MRI section begins with a brief overview of the theory of sodium NMR of biological tissues and is followed by a section on multiple quantum filters that can be used to quantify both bi-exponential relaxation and residual quadrupolar interaction. Specifically, (i) the rationale behind the use of sodium MRI in quantifying proteoglycan (PG) changes, (ii) validation studies using biochemical assays, (iii) studies on human OA specimens, (iv) results on animal models and (v) clinical imaging protocols are reviewed. Results demonstrating the feasibility of quantifying PG in OA patients and comparison with that in healthy subjects are also presented. The section concludes with the discussion of advantages and potential issues with sodium MRI and the impact of new technological advancements (e.g. ultra-high field scanners and parallel imaging methods). In the theory section on $T_{1\rho}$, a brief description of (i) principles of measuring $T_{1\rho}$ relaxation, (ii) pulse sequences for computing $T_{1\rho}$ relaxation maps, (iii) issues regarding radio frequency power deposition, (iv) mechanisms that contribute to $T_{1\rho}$ in biological tissues and (v) effects of exchange and dipolar interaction on $T_{1\rho}$ dispersion are discussed. Correlation of $T_{1\rho}$ relaxation rate with macromolecular content and biomechanical properties in cartilage specimens subjected to trypsin and cytokine-induced glycosaminoglycan depletion and validation against biochemical assay and histopathology are presented. Experimental $T_{1\rho}$ data from osteoarthritic specimens, animal models, healthy human subjects and as well from osteoarthritic patients are provided. The current status of $T_{1\rho}$ relaxation mapping of cartilage and future directions is also discussed. Copyright © 2006 John Wiley & Sons, Ltd.

KEYWORDS: cartilage; arthritis; spin-lock; T1rho; sodium; MRI

OSTEOARTHRITIS

Osteoarthritis (OA) affects more than half of the population above the age of 65 (1,2) and has a significant negative impact on the quality of life of elderly

Abbreviations used: DQF, double quantum filtered; DQFMA, double quantum filtered magic-angle; ECM, extracellular matrix; EFG, electric field gradient; FCD, fixed charge density; GAG, glycosaminoglycans; Gd-DTPA, gadolinium diethylenetriaminepentaacetic acid; MQF, multiple quantum filtered; MRI, magnetic resonance imaging; NMR, nuclear magnetic resonance; NQR, nuclear quadrupolar resonance; OA, osteoarthritis; PBS, phosphate buffered saline; PG, proteoglycan; RA, rheumatoid arthritis; RQI, residual quadrupolar interaction; SNR, signal-to-noise ratio; TQF, triple quantum filtered.
[†]This paper is published as part of a Special Issue entitled "NMR of the Musculoskeletal System".

individuals (3). The economic costs in the USA from OA have been estimated to be more than 1% of the gross domestic product (4). OA is now increasingly viewed as a metabolically active joint disorder of diverse etiologies. The biochemistry of the disease is characterized by the following changes in cartilage: reduced proteoglycan (PG) concentration, possible changes in the size of collagen fibril and aggregation of PG, increased water content and increased rate of synthesis and degradation of matrix macromolecules. The earliest changes in the cartilage due to OA result in a partial breakdown in the proteoglycan matrix with a decrease in total content. The total concentration of collagen remains unaltered in the earliest stages, although there are generally changes in the size and arrangement of the fibers. There is also a small increase in the total water content. All of these changes in the macromolecular matrix lead to an alteration in the mechanical properties of cartilage with the result that it can no longer serve as an effective load-bearing material. Current therapies of the disease have

been ineffective at halting or reversing its course and have largely been directed toward symptomatic relief. As the disease progresses to its late stages, joint surface replacement (arthroplasty) is the only effective treatment.

More recently, there have been efforts in developing novel techniques for the treatment of OA such as chondroprotective drugs and re-population of the cartilage defects by chondrocyte precursor cells with subsequent regeneration of the cartilage. Further, recent research has led to the development of drugs in animals that have shown the potential of protecting the macromolecules in cartilage from breakdown, effectively halting the progression of OA. Because of the long natural history of OA (10–20 years in humans), validating the efficacy of these drugs requires a noninvasive technique that can directly assess their effect on molecular changes associated with early stages of cartilage degeneration that precede morphological changes.

The current lack of adequate methods for quantifying these changes has hampered research directed towards the development of potential disease-modifying agents. An integrated, and noninvasive measurement of molecular (PG, collagen and water) and morphological (tissue volume) changes in cartilage will enable the detection of OA in its early stages. These measurements will help monitor disease progression, evaluate potential strategies for disease management and verify the efficacy of disease modifying drugs. Current diagnostic methods include radiography, arthrography, computed tomography (CT) and magnetic resonance imaging (MRI).

Joint space narrowing determined from conventional radiographs is widely accepted as an indication for early diagnosis of OA. However, it does not yield accurate and quantifiable results on molecular changes that precede morphological changes. Arthrography, which has these attributes, is an invasive technique that causes pain and discomfort to the subjects and is, therefore, not ideal for routine clinical use. CT, while quantitative, has the drawback of not providing biochemical information. MRI, on the other hand, provides excellent soft tissue contrast and superior delineation of intra-articular structures. From a morphological point of view, there has been substantial progress in improving our ability to study cartilage, using MRI. MRI can assess cartilage lesions and provide morphologic information about the cartilage damage. More specifically, changes such as fissuring, partial or full thickness cartilage loss and signal change within the residual cartilage can be detected. Several approaches have been developed and validated to use three-dimensional volumetric data to quantify articular cartilage in joints. Although MRI is one of the best noninvasive tools, conventional MRI (T_1-, T_2-, density-weighted and magnetization transfer imaging) has proven to be inadequate in quantifying early-stage molecular changes.

Very recently, studies on transgenic animal models have shown that ADAMTS5, an aggrecanase that cleaves the aggrecan at specific site, is responsible for the breakdown of PG and disease initiation (5,6). Although human studies are needed to confirm these studies from transgenic (tg) mice, they indicate that early molecular changes are reflected in a decrease of PG.

Several MR imaging methods have been advanced to detect and quantify such early molecular changes. Prominent in these are: proton–based methods such as T_2 relaxation mapping (7–20), delayed gadolinium-enhanced magnetic resonance imaging contrast (dGEM-RIC) (21,22), $T_{1\rho}$ relaxation mapping (23–26) and the direct MRI of sodium (27–30). T_2 is predominantly affected by changes in collagen content and to a smaller extent in PG in the tissue. Since the dominant contribution to T_2 relaxation is the dipolar interaction of protons of water associated with collagen, it is primarily useful in quantifying changes associated with collagen component of the ECM. dGEMRIC has been shown to be useful in quantifying changes in PG and this method and T_2 mapping have been extensively reviewed in recent review articles (31–34). A complete review of MRI of cartilage is beyond the scope of this article. Recent advances in MRI of cartilage have been reviewed extensively (32–43).

In the following sections, we provide: (i) a brief discussion on the structure of normal cartilage, (ii) theoretical aspects of sodium NMR and sodium multiple quantum NMR and MRI studies of cartilage and (iii) theoretical aspects of $T_{1\rho}$ weighted MRI, pulse sequences for relaxation mapping and review of $T_{1\rho}$ relaxation studies of cartilage.

The structure of normal articular cartilage (44)

Articular cartilage is a remarkable type of connective tissue that provides the synovial joints with lubrication and makes normal motion possible. It also serves to absorb mechanical shock and to distribute load over the underlying bone. Although articular cartilage will function over the lifetime of the joint under ideal circumstances, it can be damaged by trauma, osteoarthritis and inflammatory arthritis.

Articular cartilage consists of a small population of specialized cells called chondrocytes within a large extracellular matrix (ECM). The primary components of the ECM are water, collagen (15–20%) and PG (3–10%), which the chondrocytes serve to remodel continuously (Figure 1). The structure of the cartilage varies throughout its depth and consists of four histologic zones or layers. The structure and concentration of collagen and PG vary in these zones. Water is the most abundant component of articular cartilage with concentrations ranging from 80% of the volume on the surface to 65% in the deep zone. However, only a small fraction of the water is bound to collagen molecules. The affinity of cartilage for water arises primarily from the presence of the proteoglycans
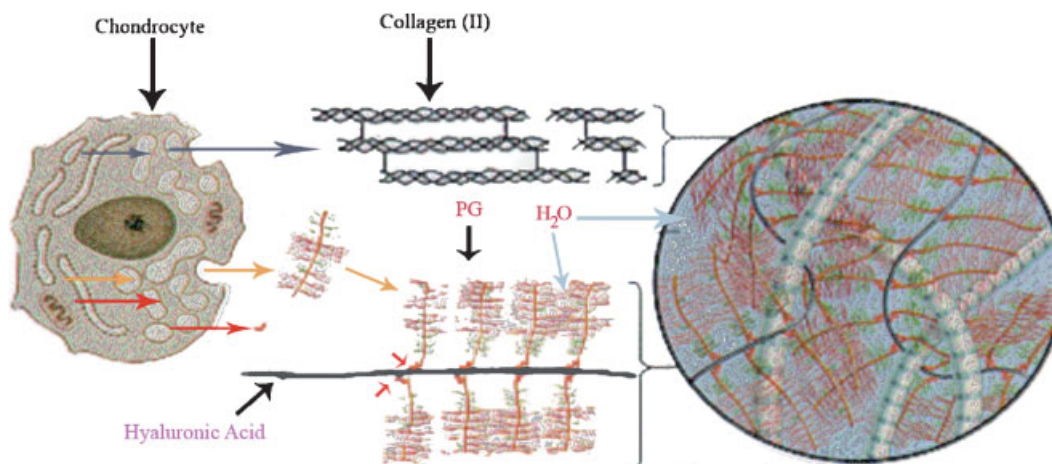
Figure 1. The extracellular matrix (ECM) of cartilage.

whose negative charges serve to attract free-floating positive ions in solution such as Na^+, which in turn attract water molecules through osmotic pressure (an example of the Donnan equilibrium).

Proteoglycans are complex macromolecules that consist of protein and polysaccharides. The most common of proteoglycans, making up 80–90% of the total, is called aggrecan [Figure 2(A)]. It consists of a protein core with a long extended domain to which many glycosaminoglycan (GAG) side chains are attached. Although both chondroitin sulfate (CS) and keratan sulfate (KS) are present in ECM, CS is the predominant GAG molecule found in cartilage [Figure 2(B)]. Several aggrecan molecules are in turn attached to hyaluronate, a long, linear polysaccharide. The resulting structure is described as having a 'lamp-brush' type of appearance. A large number of carboxyl and sulfate residues, present on the glycosaminoglycan side chains, are ionized under physiological conditions to give COO^- and SO_3^-. The negative charge density imparted by these groups is referred to as fixed charge density (FCD). These negative ions attract positive counter-ions and water molecules and provide a strong electrostatic repulsive force between the proteoglycans. These osmotic and electrostatic forces are responsible for the swelling pressure of cartilage. The configuration of the PG macromolecules also contributes to the resistance of the matrix to the passage of water molecules and hence affects the mechanics of the cartilage in this fashion.

Collagens are proteins with a characteristic triple-helical structure. Although many different types of collagen are found in cartilage, the most common is collagen type II (90–95% of the overall mass of collagen in cartilage). The collagen molecules aggregate into fibers that are 10–100 nm in diameter. The major role of the collagen II fibers is to provide a tensile force opposing the tendency of the proteoglycans to expand the cartilage and
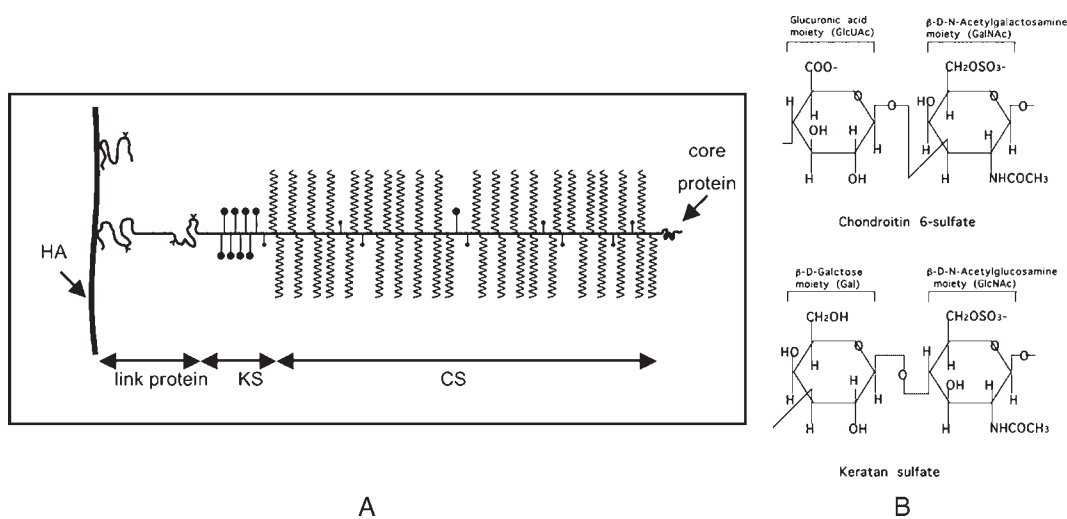
Figure 2. The aggrecan proteoglycan macromolecule (A) comprising hyaluronic acid (HA), keratan sulfate (KS) and chondroitin sulfate (CS). The molecular structures of chondroitin 6-sulfate and keratan sulfate moieties are shown in (B).
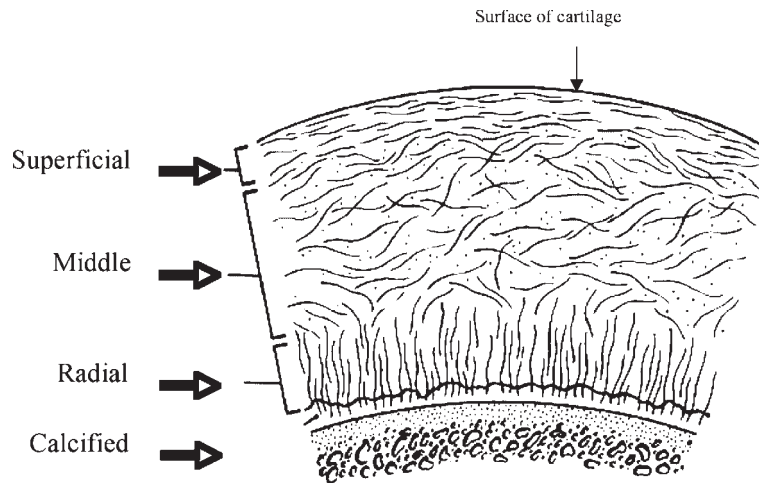
Figure 3. Arrangement of collagen fibers across different layers of the cartilage.

also serve to immobilize the proteoglycans. Since there are no net charges on collagen it does not impart any FCD to the ECM. Collagen fibers have different arrangement across the tissue (Figure 3). In the radial zone collagen arrangement is perpendicular to the surface of the tissue while in the superficial zone it is parallel to the surface. However, in the middle zone the arrangement is almost random. This characteristic arrangement leads to the so called 'magic angle effect' and laminar appearance in the proton MR images. Many other molecules are present in the ECM in low concentrations, most of whose functions are not clearly understood.

Features of articular cartilage during osteoarthritis

Osteoarthritis can affect virtually any joint that contains cartilage; however it is most commonly seen in the hands, knee, hip and spine, either isolated as localized OA or as generalized OA when it affects three or more joints (45). While specific conditions, such as trauma to the joint and congenital disease, may lead to secondary OA, most cases of OA are classified as idiopathic.

The affected joint is victim to a striking breakdown of the cartilage matrix and eventually a total loss of joint cartilage. The OARSI cartilage OA pathology assessment system provides six grades of OA involvement (46). In grade 1, the cartilage matrix undergoes swelling, abrasion and changes in the structure of the cartilage such as patchy condensation of collagen and gain or loss of chondrocytes. Stains such as Safranin O or Toluidene Blue, which are used semi-quantitatively in many studies as markers for proteoglycan, can be indicative of proteoglycan loss at this early point. While structural MRI is sometimes able to see synovial thickening at this early stage (47), only imaging techniques sensitive to molecular changes such as sodium imaging, $T_{1\rho}$-weighted imaging and dGEMRIC MRI can hope to regularly detect and track OA at this stage.

Grade 2 OA begins to see exfoliation of ECM from the surface of the joint and in grade 3 fissuring from the surface into the mid zone of the cartilage is observed. It is not until grade 4 that large-scale structural changes begin to occur. Increased fissuring and delamination of the surface leads to erosion and loss of the superficial zone. Chondrocyte death and metaplasia begin at stage 3, but are prominent at this point. It is at this time that larger structural changes can be regularly seen on T_2-weighted imaging, CT, and after joint space narrowing with loss of cartilage, X-Ray. Grades 5 and 6 OA exhibit almost a total loss of articular cartilage, and changes to the underlying bone structure such as osteophytes and microfracturing are evident.

The etiology of OA is thought to be a complex interplay of mechanical joint trauma and molecular factors where chondrocytes are unable to repair joint damage, leading to progressive cartilage loss (48). The classification of joint disease as OA is often meant to separate the disease process from other types of arthritis, such as rheumatoid arthritis (RA), that have better elucidated inflammatory components. Nevertheless, it is increasingly recognized that inflammatory or other molecular mediators may have a central role in the progression of OA. While it is beyond the scope of this article to discuss the myriad proteins implicated as markers or factors in OA pathogenesis, certain models of OA deserve attention for later discussion.

Models of osteoarthritis in articular cartilage

Early studies determined that a certain factor isolated from synovial fluid and produced by lymphocytes, later discovered to be interleukin-1 (IL-1), stimulates release of GAG from the ECM and suppresses new GAG synthesis in explant cultures (49). It was not long before IL-1β was being used frequently with *in vivo* and *ex vivo* cartilage as a model of arthritis for the testing of

pharmacotherapeutics and investigations of arthritis signaling (50). Genetic evidence for a role of IL-1β in OA came much more recently with the discovery of polymorphisms in the IL-1 gene cluster that act as risk factors for OA (51–53). In arthritis imaging research, IL-1β is now used to simulate osteoarthritis in animal models in order to track progression of mild disease by emerging techniques (54).

The interleukin-1 super-family includes the agonists IL-1α/IL-1F and IL-1β/IL-1F2 (55). IL-1α and IL-1β are produced as approximately 31 kDa precursor forms and are cleaved by IL-1β converting enzyme (ICE), also known as caspase-1, to forms weighing about 17.5 kDa. However, only IL-1β requires cleavage to have activity, while both the pro-form and the mature form of IL-1α are active (56). Activity is often conserved across higher mammals, as evidenced by homologous biological activity of recombinant human IL-1α and IL-1β on many other species, including cow (57), pig (58) and mouse (59).

Interleukin-1 is thought to stimulate breakdown of the ECM by causing the upregulation of two families of metalloproteinases. Messenger RNA of numerous members of the matrix metalloproteinase (MMP) family, including the collagenases MMP-1, MMP-8 and MMP-13, as well as MMP-14, MMP-3 and MMP-9, have been shown to be upregulated by IL-1 in human chondrocytes *in vitro* (60). The same study also showed upregulation of the aggrecanases ADAMTS-4 (aggrecanase-1) and ADAMTS-5 (aggrecanase-2) by IL-1. These proteins belong to the disintegrin and metalloprotease with thrombospondin motifs family (61), and are the only enzymes that have been shown to cleave aggrecan at a site that generates the Glu373-Ala374 fragments (62,63) seen in interleukin-1 stimulated bovine explant cultures (64) and human synovial fluid of OA patients (65).

Very recent studies of transgenic animal models suggest that ADAMTS5 may in fact be necessary for the induction or progression of symptomatic OA (5,6). Two groups working independently found that ADAMTS5 knockout mice were protected from experimentally induced arthritis by IL-1β, foreign antigen stimulation and joint instability. This provides an exciting target for development of medications targeting early mediators of arthritis that will slow or arrest the progression of OA. Testing of these new therapies may benefit from confirmation by noninvasive molecular imaging techniques that show a corresponding halt in ECM loss in tissue.

An alternative model of osteoarthritis is the use of trypsin to induce the degeneration of proteoglycan (66–68). Trypsin is a 24 kDa endopeptidase commonly produced in the pancreas for the digestion of dietary amino acids (69). It cleaves a wide range of proteins at the C-terminus of lysine or arginine except when followed by a proline residue. While collagen, due to its large number of prolines, is not susceptible to trypsin digestion under all but very harsh conditions (70), application of trypsin to explant cartilage cultures readily causes the degradation of PG and other extracellular molecules (71). It is unlikely that trypsin itself plays a major role in the pathogenesis of OA; however imaging techniques are frequently tested by their ability to detect trypsin-induced degeneration of cartilage (72,73).

Sodium NMR

Sodium is one of the most 'NMR-visible' nuclei in living systems. The NMR relaxation properties of a nucleus depend on its immediate environment and its interactions that perturb the dominant Zeeman Hamiltonian in a significant manner. The most important interaction experienced by sodium nuclei is that between the nonspherically symmetric nucleus and surrounding electric field gradients. This is called the quadrupolar interaction. In general, sodium in solids experience most of these interactions while in liquids, the static quadrupolar interaction is averaged to zero. In the intermediate regimes, e.g. in biological tissues, the quadrupolar interaction results in biexponential relaxation rates. Multiple quantum filtered ^{23}Na NMR can be used to analyze spectra from such systems. The following sections describe quadrupolar interaction and its effect on the ^{23}Na NMR spectrum and relaxation rates in greater detail.
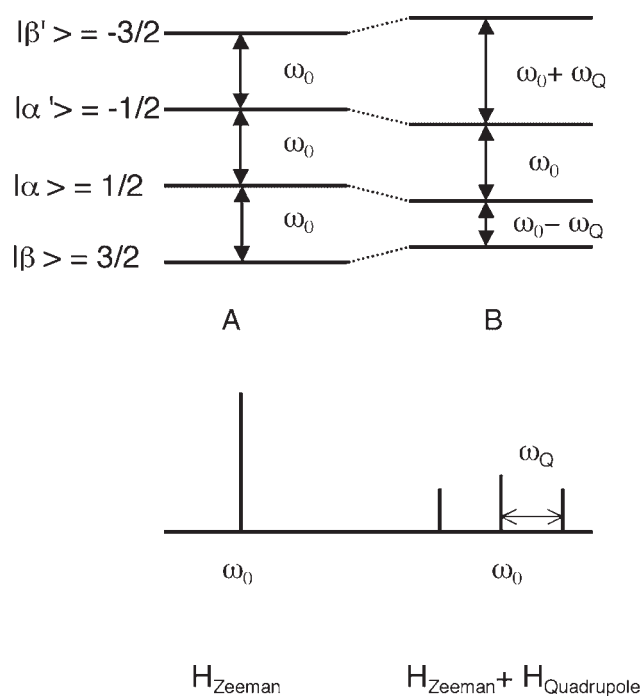
The quadrupolar interaction. Sodium is a spin 3/2 nucleus and possesses quadrupole moment (Q), which interacts with electric field gradient (EFG) generated by the electronic distribution around the nucleus. In the absence of external magnetic field, this interaction establishes degenerate energy states in solid state. Transitions induced by appropriate RF pulses (with a frequency that is resonant with the frequency separation of the states) are responsible for the pure nuclear quadrupole resonance (NQR). This has been reviewed extensively in several original articles and books (74–76) and will not be discussed here.

When Zeeman interaction is greater than the quadrupolar interaction, the degeneracy of the energy levels is lifted and the spin dynamics are dictated by the physical status of the material. The theory of NMR of quadrupolar nuclei (74,75,77–80), relaxation-induced sodium single and multiple quantum coherences (MQC) and their applications in the studies of biological systems has been extensively discussed in several original and review articles (81–91). Here a brief overview of steps involved in the calculation of spin dynamics using the density matrix approach is presented.

The nuclear quadrupole interaction is determined by the orientation, magnitude and temporal duration of EFG generated by the surrounding lattice and the electronic configuration around the nucleus and can be described by a tensor. In a system of rapid motion, e.g. fluid, all orientations of the EFG are equally probable. In this 'isotropic' system, the quadrupolar interaction is aver-

aged to zero on the time scale of $1/\omega_0$ (Figure 4). However, in an anisotropically oriented system, such as liquid crystals or oriented macromolecules, the sodium nuclei experience a nonzero average EFG. This static quadrupole coupling induces a shift in the energy levels of the spin system and consequently the spectrum shows multiple lines. The frequency separation between these lines provides indirect information about the magnitude of macroscopic ordering in the system.

In the Redfield regime, where the relaxation of spin 3/2 is described by second-order perturbation theory, the spin dynamics can be solved analytically. It is well known that longitudinal relaxation gives information about relatively fast motions (in MHz) and its dispersion can be studied by measuring relaxation rates at different field strengths. Slow dynamics (frequencies in the range of 0 to a few kHz) can be probed by transverse relaxation (T_2) or relaxation under the influence of a spin-locking pulse ($T_{1\rho}$) known as the 'spin-lattice relaxation in the rotating frame'. Here, we closely follow the treatment by van der Marrel (83,84,92). It is convenient to describe the dynamics of spin $I > 1$, the effects of RF pulses and the evolution under the action of static and fluctuating quadrupolar interactions using the irreducible tensor operator (T_p^l) representation. Where l represents the rank and p represents the order of the tensor. We use the

orthonormal unit tensor operators as defined in van der Marrel (83,84). We define symmetric and anti-symmetric combinations as:

$$\begin{aligned} T_p^l(s) &= (1/\sqrt{2})(T_{-p}^l + T_p^l) \\ T_p^l(a) &= (1/\sqrt{2})(T_{-p}^l - T_p^l) \end{aligned} \qquad (1)$$

for spin 3/2, the density operator is expanded in terms of 16 orthonormal basis operators, which are shown in Table 1.

In the principal axis system of the spin 3/2 nucleus and for an axially symmetric electric field gradient, the static quadrupolar Hamiltonian is given by:

$$H_{QS} = \omega_Q T_0^2 \qquad (2)$$

where ω_Q and represents the static residual quadrupolar interaction (RQI), only the part of the interaction that persists after motional averaging and not the r.m.s. average of the fluctuating part.

Several models have been explored to describe the role of static quadrupolar interaction in biological systems. If this nonaveraged interaction is uniform, as in the case of liquid crystals, then clear quadrupolar splitting is observed in the spectra provided the splitting exceeds the linewidths of the individual peaks. The interaction can be heterogeneous across the sample, as in the case of nonuniformly aligned systems. In this situation, the sample may be modeled as made from individual domains, each characterized by a local director but all possessing the same dynamic properties. The exchange among the domains usually is slow on a time scale of the inverse of the linewidths and the splitting, so that the observed spectrum represents a static average over all domains. Each domain is characterized by a residual quadrupolar coupling (RQC) given by:

$$\omega_Q = \overline{\omega_Q}\left(\frac{3\cos^2\theta - 1}{2}\right) \qquad (3)$$

Figure 4. Energy level diagram of spin 3/2 nucleus. The frequency difference between adjacent energy levels is the same, ω_0 (A). It represents the isotropic solution state, where quadrupolar interaction is averaged to zero. (B) Nonzero static quadrupolar interaction shifts the energy levels, producing three spectral peaks. This represents the situation in solids, liquid crystals and oriented macromolecules. The frequency separation between adjacent energy level are given by: $(\omega_0 - \omega_Q)$, ω_0 and $(\omega_0 + \omega_Q)$.

Table 1. The 16 orthonormal basis operators of a spin-3/2 system

Operator	Definition
T_0^0	Identity
$T_0^1 = (1/\sqrt{5})I_z$	Longitudinal magnetization
$T_1^1(a) = (1/\sqrt{5})I_x$, and $T_1^1(s) = (-i/\sqrt{5})I_y$	Proportional to x- and y-magnetization, respectively
T_0^2	Quadrupolar spin polarization
$T_1^2(s)$ and $T_1^2(a)$	Rank 2 single quantum coherences
$T_2^2(s)$ and $T_2^2(a)$	Rank 2 double quantum coherences
T_0^3	Octopolar spin polarization
$T_1^3(s)$ and $T_1^3(a)$	Rank 3 single quantum coherences
$T_2^3(s)$ and $T_2^3(a)$	Rank 3 double quantum coherences
$T_3^3(s)$ and $T_3^3(a)$	Rank 3 triple quantum coherences

where θ is the angle between the local director and the direction of the main magnetic field B_0 and $(\overline{\omega_Q}) = \omega_Q^{loc}$ denotes the maximum splitting measured (in the local director frame) for $\theta = 0°$.

The frequency of the central transition is unaffected in the first order approximation of this interaction, but the satellite transitions are spread out over a large frequency range depending on the distribution in values of θ. The broadening of satellites due to an inhomogeneous static quadrupolar coupling makes it difficult to measure the position of the satellite transitions using conventional methods. Several pulse sequences have been developed to extract this information based on the detection of the formation of the even rank double quantum coherence (86). The spin system evolves under the influence of Zeeman, radiofrequency, static quadrupolar and fluctuating quadrupolar Hamiltonians.

In NMR, the detected signals are equivalent to those obtained by performing the calculations in the rotating frame or interaction representation given by:

$$U = e^{-iH_Z t} \tag{4}$$

$$H_Z = -\omega_0 T_0^1 \tag{5}$$

$$\omega_0 = -\gamma B_0 \tag{6}$$

in which the Zeeman Hamiltonian vanishes.

The total interaction Hamiltonian for spin 3/2 in the interaction representation (represented with '*') is:

$$H_T^* = H_{RF}^* + H_{QS}^* + H_{QF}^* \tag{7}$$

where H^*_{RF} represents the RF field applied in the transverse plane with a phase ϕ.

$$H_{RF}^* = -\omega_{RF}[\sqrt{5}\{-T_1^1(a)\sin\phi + iT_1^1(s)\cos\phi\}] \tag{8}$$

$$H_{QS}^* = \omega_Q T_0^2 \tag{9}$$

Since H_Q commutes with H_z, it remains unaffected in the interaction representation:

$$H_{QF}^*(t) = C_Q \sum_{m=-2}^{2} (-1)^m T_m^2 e^{im\omega_0 t} \left[F_{-m}^2(t) - <F_{-m}^2> \right] \tag{10}$$

where $C_Q = eQ/(\hbar\sqrt{6})$ and Q is the quadrupole moment of the nucleus and EFG components are given by:

$$\begin{aligned}
F_2^0 &= (1/2)V_{zz} \\
F_{\pm 1}^2 &= \mp(1/\sqrt{6})(V_{xz} \pm iV_{yz}) \\
F_{\pm 2}^2 &= (1/2\sqrt{6})(V_{xx} - V_{yy} \pm 2iV_{xy})
\end{aligned} \tag{11}$$

and $\langle F_m^2 \rangle$ represents their average values.

Macromolecular motions impart fluctuations and hence a time dependence in the EFG components. Having established the Hamiltonians in the interaction representation, we are ready to discuss the spin dynamics. Spin dynamics of quadrupolar nuclei can be described by solving the Liouville equation over a range of motional regimes and following the time evolution of density operator (ρ) in response to RF pulses and in the presence of quadrupolar relaxation and static quadrupolar interaction (75,81–84,93–97). The time evolution of density operator under a static Hamiltonian, such as the static quadrupolar Hamiltonian is given by (74):

$$\frac{d\rho^*}{dt} = -i[H_{QS}^*, \rho^*] \tag{12}$$

The time evolution of the fluctuating quadrupolar Hamiltonian $H_{QF}^*(t)$ can be treated according to the Redfield relaxation theory (98,99). Changes in the density operator are small on the time scale τ_c of the lattice motions i.e. $<H_{QF}^{*2}> \tau_c \ll 1$. Therefore we can justify the use of second-order perturbation theory for our calculations. In most of the biological systems this condition is satisfied because of the rather long correlation times associated with macromolecular motions and relatively small values of corresponding coupling constants. We can also include the contribution from relaxation:

$$\frac{d\rho^*}{dt} = -i[H_{QS}^*, \rho^*] + \Gamma(\rho^*) \tag{13}$$

where the relaxation superoperator is given by:

$$\begin{aligned}
\Gamma(\rho^*) = \int_0^\infty &< [H_{QF}^*(t), [\exp(-iH_{QF}^*\tau)H_{QF}^*(t-\tau) \\
&\times \exp(iH_{QF}^*\tau), \rho^*(t)]] > \delta\tau
\end{aligned} \tag{14}$$

Since the static quadrupolar Hamiltonian commutes with $H_{QF}^*(t)$, it vanishes in the relaxation superoperator. If the EFG is completely averaged to zero by molecular motion, then $H_{QS}^* = 0$ and the spin dynamics are governed exclusively by relaxation. This equation can be recast into a more familiar master equation in terms of the Redfield relaxation matrix **R** as:

$$\frac{d\rho_{\alpha\alpha'}^*}{dt} = -i[H_{QS}^*, \rho_{\alpha\alpha'}^*] + \sum_\alpha \sum_{\alpha'} R_{\alpha\alpha'\beta\beta'}\rho_{\alpha\alpha'}^* \tag{15}$$

where $|\alpha>$ and $|\beta>$ are the eigenfunctions of unperturbed Hamiltonian (in the presence of nonaveraged static quadrupolar interaction), identifies the phase coherence between states α and α' which is the $\alpha - \alpha'$th element of spin density operator, and is defined as:

$$\langle \alpha | \rho(t) | \alpha' \rangle = \rho_{\alpha\alpha'}(t) \tag{16}$$

Several authors have solved this equation and described the spin evolution in response to RF pulses, under pure quadrupolar relaxation and in the presence of both quadrupolar relaxation and nonaveraged static quadrupolar interaction. Expressions for single, double and triple quantum-filtered signals have been derived under different limiting conditions. Following an RF pulse, the density matrix evolves in the presence of quadrupolar relaxation and static quadrupolar interaction and can be solved using the solutions to eqns (13) and (15).

Energy levels of sodium nuclei

The energy level diagram shown in Figure 4 depicts the energy level pattern of a spin 3/2 nucleus in different motional regimes. The following three motional regimes are possible.

Case 1: Isotropic motion with motional narrowing ($\omega_0\tau_c \ll 1$).

Figure 4(A) illustrates the spectrum from sodium in an isotropic solution state (τ_c is the rotational correlation time). The rapid tumbling of molecules containing sodium lead to a fluctuation of the EFG more rapidly than the Larmor period ($2\pi/\omega_0$), hence the quadrupole interaction is 'motion-narrowed' to zero. Consequently, the Zeeman interaction alone will result in four energy levels with equal frequency separation ω_0. Transitions induced by RF pulses at this frequency lead to a single resonance line at ω_0. Both transverse and longitudinal relaxations are simple exponential decays (100).

Case 2: isotropic motion without motional narrowing ($\omega_0\tau_c \approx 1$).

In biological tissues where the macromolecular motion associated with the nucleus is isotropic but $\omega_0\tau_c \approx 1$, the quadrupolar interaction dominates the relaxation. In this case, the satellite and central transitions will have different relaxation rates $R_1^{(\pm 1)}$ and $R_2^{(\pm 1)}$, respectively, with $R_1^{(\pm 1)} > R_2^{(\pm 1)}$. These fast and slow decaying components are dynamically shifted from the Larmor frequency with shifts K_1 and $K_2 - K_1$, respectively. However, these shifts are much smaller than the line-widths and very difficult to detect. Hence, in the subsequent discussion we will ignore these dynamic shifts. This situation is still described by Figure 4(A) with the difference that the relaxation is now bi-exponential.

$$\begin{aligned} R_1^{(\pm 1)} &= J_0 + J_1 \pm iK_1 \\ R_2^{(\pm 1)} &= J_1 + J_2 \mp i(K_1 - K_2) \end{aligned} \tag{17}$$

where

$$\begin{aligned} J_m(m\omega) &= \frac{(2\pi)^2}{20}\left(\frac{\chi^2\tau_c}{1+(m\omega)^2\tau_c^2}\right) \\ K_m(m\omega) &= \omega\tau_c J_m(m\omega) \end{aligned} \tag{18}$$

where the spectral densities J_m and K_m are the real and imaginary parts of the Fourier transform of the EFG correlation function (83). χ_2 is the root mean square coupling constant.

Even in the absence of any quadrupolar splitting, biexponential relaxation can create multiple quantum coherences (MQC), which can be detected (82,101,102). In this case, the observed double quantum coherence is solely due to odd rank, $T_{\pm 2}^3$, and the even-rank double quantum state ($T_{\pm 2}^2$) is never created. Owing to its higher sensitivity, triple quantum filtered (TQF) sodium spectroscopy is well suited for measuring bi-exponential transverse relaxation rates (96).

Case 3: anisotropic motion ($\omega_0\tau_c > 1$).

In this case, the single quantum relaxation eigenvalues are given by

$$\begin{aligned} R_1^{(1)} &= J_0 + J_1 + J_2 - \sqrt{(J_2^2 - \omega_Q^2)} \\ R_2^{(1)} &= J_1 + J_2 \\ R_3^{(1)} &= J_0 + J_1 + J_2 + \sqrt{(J_2^2 - \omega_Q^2)} \end{aligned} \tag{19}$$

$R_3^{(1)}$ is present due to the formation of even rank two-quantum coherence, T_2^2.

The following three situations can be identified based on the magnitude of J_2:

(1) If $\omega_Q < J_2$, the relaxation eigenvalues are real and line splitting is absent, despite the presence of a nonzero EFG. The single quantum spectrum is a sum of three Lorentzians and ω_Q influences the line-widths and amplitudes of these components but it is difficult to fit these lines to determine individual line-widths.

In ordered biological tissues where the molecular motion is slow ($\omega_0\tau_c > 1$), there is an RQI that arises as a result of the ions interacting with structural proteins such as collagen fibers in connective tissues and proteins that are part of cell membranes. This results in a very small splitting in the spectrum of sodium, which is masked by the larger single quantum line-widths. Further, the dominant presence of sodium in surrounding fluids in isotropic motion complicates the detection of RQC. Thus, measuring the relatively small RQC from motion-restricted sodium in biological tissues using conventional single quantum NMR is difficult and alternative approaches are required. However, if the residual ω_Q is comparable to line-widths, then it does not lead to line splitting but it still creates double quantum coherence due to the even-rank coherence ($T_{\pm 2}^2$). In this case, the double quantum filtered (DQF) signal due to even rank coherence ($T_{\pm 2}^2$) can be used to detect and measure the RQC (103–105).

(2) If $\omega_Q > J_2$, the satellite signals do not overlap with the central transition and the relaxation eigenvalues $R_1^{(1)}$ and $R_3^{(1)}$ corresponding to outer transitions are complex and the satellite transitions are shifted by $\pm(\omega_Q^2 - J_2^2)^{1/2}$ from the central line. The satellite signals in the single quantum spectrum will have complete amplitudes and are phase twisted with respect to the central line. In this case too, the DQF signal from $T_{\pm 2}^2$ can be used to measure ω_Q.

(3) If $\omega_Q \gg J_2$, the energy levels are all shifted by ω_Q resulting in three distinct frequency separations between the energy levels [see Figure 4(B)]. The transitions between these energy levels are governed by the allowed selection rule ($\Delta m = \pm 1$) and lead to three distinct resonance lines: a central transition and two satellite transitions separated by ω_Q. The nuclear spin relaxation rates of the central line and the
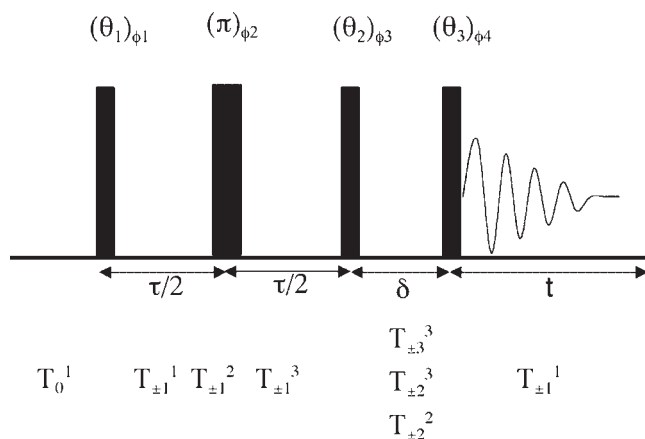
Figure 5. Pulse sequence for multiple quantum filtering. τ, δ and t are preparation, evolution and detection times, respectively. Tensor components during each time period represent the possible coherences. Appropriate phase cycling of the RF pulses is used to select either double or triple quantum coherences.

satellite lines are given by:

$$R_s^{(1)} = J_0 + J_1 + J_2$$
$$R_c^{(1)} = J_1 + J_2 \qquad (20)$$

It should be noted that in the presence of a static quadrupolar interaction, the relaxation rate of satellite lines ($R_s^{(1)} = J_0 + J_1 + J_2$) are different from the corresponding ones in the isotropic situation $R_1^{(1)} = J_0 + J_1$.

Multiple quantum filtered (MQF) NMR

An example of a multiple quantum filter pulse sequence is shown in Figure 5. There is a preparation period (τ) during which time the longitudinal magnetization (T_0^1) magnetization is flipped by an RF pulse of angle θ_1 and phase ϕ_1 into the transverse plane. The new transverse magnetization ($T_{\pm1}^1$) evolves in the presence of relaxation and/or RQC, creating single quantum coherences (SQC) with different rank ($T_{\pm1}^1, T_{\pm1}^2, T_{\pm1}^3$) but with the same order, and a second θ_2 and phase ϕ_3 pulse will convert them into multiple quantum coherences ($T_{\pm1}^1, T_{\pm2}^2, T_{\pm2}^3, T_{\pm3}^3$). The second RF pulse changes the order of the coherences while keeping the same rank. The π-pulse applied at $\tau/2$ does not affect coherences and is used to refocus any resonance offsets and field inhomogeneities. During the evolution period (δ), the MQCs will evolve with a characteristic relaxation time depending upon the order of the coherence. Generally, the evolution time is kept very short to avoid their decay. Since the MQCs cannot be detected directly, the final (θ_3)$_{\phi4}$ pulse converts the MQCs into SQCs ($T_{\pm1}^1, T_{\pm1}^2, T_{\pm1}^3$) which then evolve under relaxation and RQC to detectable SQC ($T_{\pm1}^1$) during the acquisition time. One may choose to detect the desired order of coherence using appropriate choice of flip angles and phases of the RF pulses (86,106).

Single quantum signal expression. Consider a spin 3/2 nucleus in biological tissues with bi-exponential relaxation and nonzero RQC in a magnetic field. Immediately following the application of a nonselective 90° pulse, the longitudinal magnetization is flipped into transverse plane and then evolves under the influence of biexponential relaxation rates and RQC during the acquisition period, t. Dropping the factors representing temperature, the signal expression following a 90° pulse is given by (83,84,92),

$$S(t) \sim M_0 \frac{1}{5}\left(\frac{3}{2}e^{-(R_s^{(1)}-i\omega_Q)t} + 2e^{-R_c^{(1)}t} + \frac{3}{2}e^{-(R_s^{(1)}+i\omega_Q)t}\right)$$
(21)

where M_0 is the thermal equilibrium magnetization, $R_s^{(1)}$ and $R_c^{(1)}$ are relaxation rates of satellite and central transitions respectively and are given above. Here, for the ease of illustration, it is assumed that the nonzero quadrupole interaction is large enough to create line splittings.

Triple quantum filtered signal expression. The triple quantum filtered signal is detected by setting $\theta_1 = \theta_2 = \theta_3 = \pi/2$, and $\phi_1 = \phi_2 = \phi$; $\phi_3 = \phi + \pi/2$, $\phi_4 = 0°$ where ϕ is cycled through 30, 90, 150, 210, 270 and 330° while alternating the receiver phase between 0 and 180°. The addition of all six acquisitions produces the TQF signal:

$$S(\tau, t) \sim M_0 \frac{9}{80}\left[(e^{-(R_s^{(1)}-i\omega_Q)\tau} - 2e^{-R_c^{(1)}\tau}\right.$$
$$+ e^{-(R_s^{(1)}+i\omega_Q)\tau)}$$
$$\left.\times (e^{-(R_s^{(1)}-i\omega_Q)t} - 2e^{-R_c^{(1)}t} + e^{-(R_s^{(1)}+i\omega_Q)t})\right] \qquad (22)$$

A series of TQF spectra are collected (for a fixed δ, usually in few µs) as a function of preparation time, τ, and the resulting spectral amplitudes are fitted to the signal expression to compute the relaxation rates (an example is shown in the case of *in vivo* data). The triple quantum filtered signal has 50% higher sensitivity than the DQF signal and is preferred for measuring biexponential relaxation. It does not have complications of mixing of odd and even rank coherences associated with the DQF signal. Furthermore, it can be used with surface coils, which have inhomogeneous B_1 fields, to study relaxation in biological tissues (106,107).

Double quantum filtered signal expression. A double quantum filtered magic angle (DQF-MA) signal is detected by setting $\theta_1 = \pi/2$, $\theta_2 = \theta_3 = 54.7°$ and $\phi_1 = \phi_2 = \phi_3 = \phi$ and $\phi_4 = 0°$ where ϕ is cycled through 0, 90, 180 and 270° while the receiver phase is alternated between 0 and 180°. This sequence exclusively detects T_2^2 and is important for studying ordered structures.
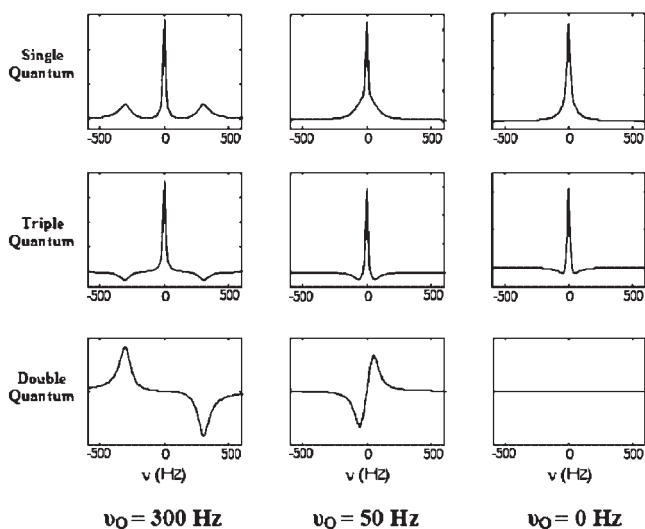
Figure 6. Simulated SQ, TQF and DQF-MA spectra [from eqns (21)–(23)] for different quadrupolar splitting frequencies ($\nu_Q = \omega_Q/2\pi$). The evolution time $\tau = 2$ ms, $T_{2\text{fast}} = 1$ ms, $T_{2\text{slow}} = 15$ ms. At low ω_Q values greater than 0, clear splittings are absent and experimental DQF-MA spectra can be fitted to extract ω_Q directly.

However, if the flip angles of the last two pulses are set to $90°$ then the detected DQF signal will be a combination of both T_2^2 and T_2^3. Addition of all four acquisitions produces the DQF-MA signal:

$$S(\tau, t) \sim M_0 \frac{1}{10} \left[\left(e^{-(R_s^{(1)} - i\omega_Q)\tau} - e^{-(R_s^{(1)} + i\omega_Q)\tau} \right) \right.$$

$$\left. \times \left(e^{-(R_s^{(1)} - i\omega_Q)t} - e^{-(R_s^{(1)} + i\omega_Q)t} \right) \right] \qquad (23)$$

Situations corresponding to different motional regimes can be arrived at by choosing appropriate values for ω_Q and spectral densities and the above signal expressions. The DQF-MA sequence has been used to study ordered structures in cartilage, and cytoskeleton (93,103,105, 108,109). Typical simulated spectra using the above signal expressions are shown in Figure 6, and Fig. 7 shows typical SQ, DQF and TQF sodium spectra from articular
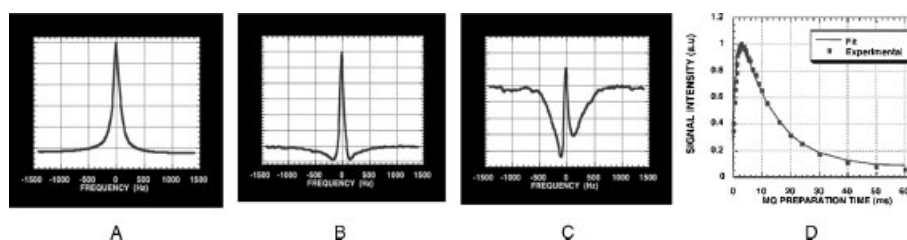
cartilage. The pronounced negative lobes of DQF spectra are due to the presence of ($T_{\pm 2}^2$) contribution in addition to $T_{\pm 2}^3$.

Other pulse sequences that are useful in studying ordered structures are based on the Jeener-Broekaert (108,110) and spin-locking sequences (84,111). In both these sequences, the signal is detected by filtering through the quadrupolar order T_0^2. The efficiency of both DQF-MA and JB sequences in detecting ordered sodium depends on the precision of the flip angles and hence these methods are very susceptible to B_1 inhomogeneities. The spin-locking method is independent of flip angle precision and is more tolerant to B_1 inhomogeneities. Recently, newer methods have been introduced to study sodium in ordered systems based on suppression of the central transition by applying soft pulses and employing double frequency sweep pulses. These sequences suppress signal from sodium in the isotropic regime and detect only the satellite signals (112) or convert them to a central transition signal (113,114). These methods are robust in spite of B_1 inhomogeneities. Other methods that are promising in detection of ordered sodium ions include quadrupolar filter by nutation (QFN) (115). QFN exploits the dependence of quadrupolar interaction on nutation frequencies to suppress isotropic sodium and detect the central transition of ordered sodium.

Single and multiple quantum sodium NMR has been used extensively to study various biological tissues such as brain (89,90,104,116–120), breast (121) heart (122–128), muscle (129,130), tumors (131–133), blood (122) and cartilage (27,93,134–136) and reviewed in several articles (86,87,91,108,119,137–141). In this review, however, we restrict our discussion to sodium NMR of cartilage.

Sodium NMR of cartilage

Owing to the sparse cellular content ($\sim$2% by volume) and highly ordered nature of cartilage, most of the sodium in ECM of cartilage is in a slow motion regime and exhibits multiple quantum coherences. The sodium NMR

Figure 7. Sodium multiple quantum coherences from articular cartilage: (A) single quantum, (B) double quantum coherence ($T_2^2 + T_2^3$) and (C) triple quantum coherence (T_2^3). Pronounced negative lobes in double quantum coherence ($T_2^2 + T_2^3$) compared with triple quantum coherence is due to the nonaveraged quadrupolar interaction. (D) Normalized triple quantum spectral intensity from human articular cartilage *in vivo* plotted as a function of preparation time. The solid line is the fitted to the TQF signal expression (142).

signal from biological tissues is governed by the relevant values of M_0, R_s, R_c and ω_Q of the system. It should be noted here that 40% of total sodium is observed directly through the central transition, which decays with a longer time constant (T2 slow = T2 fall = $1/R_c^{(1)}$) compared with the 60% of sodium that contributes to the satellite transitions, which decay with a faster relaxation time (T2fast = T2rise = $1/R_s^{(1)}$). Therefore, in order to quantify the absolute sodium concentration from biological tissues, one has to use ultra-short RF pulses and fast acquisition schemes. Otherwise, significant amount of the fast-decaying signal will be lost before detection and this will lead to an underestimation of the total [Na].

Sodium MQF NMR of cartilage

MQ spectroscopy. As stated above, anisotropic motion due to an averaged quadrupolar interaction in biological tissues can be detected via the even-ranked double quantum coherence T_2^2. In the presence of anisotropic motion, transverse relaxation times of the satellite and central transitions measured via TQF sequence are referred to as T_{2rise} and T_{2fall}. The RQC constant can serve as the local order parameter for a given tissue. Although the SQC signal is sum of exponentials and influenced by RQC, it is difficult to determine the relaxation times accurately from this signal. However, as described above, MQ spectroscopy with ultrashort duration RF pulses enables the measurement of all the parameters that govern sodium spin dynamics in tissues. To this end, TQF spectroscopy has been used to measure biexponential relaxation rates of cartilage both *in vitro* (142) and *in vivo* (143). In this study, a flip-angle independent TQF pulse sequence was employed that permitted the use of a surface coil to transmit and receive. Transverse relaxation times of sodium obtained from asymptomatic volunteers were found to be: $T_{2rise} = 1 \pm 0.12$ ms, $T_{2fall} = 12.0 \pm 0.75$ ms (mean ± SD).

Anisotropic motion of sodium ions was also detected via $T_{\pm2}^2$ in cartilage and in collagen fibers. DQF spectroscopy was used to measure the RQC constant in nasal cartilage (93). Analytical expressions for the DQF spectra were obtained by calculating the evolution of the second and third rank tensors by solving a modified Redfield equation. It was shown that anisotropy was due to local rather than macroscopic order. The observed spectra were fitted to DQF signal expressions from several models by assuming an isotropic distribution of the local directors of the locally ordered sites. They showed that a model that assumes a Gaussian-weighted distribution of ω_Q values provided the best fit for the MQF-NMR spectra from fresh bovine nasal cartilage. In this analysis, the local RQC was found to be 550 Hz in nasal cartilage. Using isolated models of cartilage, it was shown that the contribution to RQC in cartilage was due to the ordering of collagen bundles and that PG did not

contribute to the RQC. A similar model provided the best fit for Jeener–Broekaert spectra obtained from bovine articular cartilage (144).

The effect of interleukin-1β (IL-1β), a cytokine known to induce matrix degradation, was studied in bovine cartilage explants using TQF and double quantum filtered magic angle (DQF-MA) methods (109). Changes on relaxation times and RQC are measured in bovine cartilage specimens. T_{2rise} ranged between 2.26 and 3.5 ms, decreasing with increased PG loss. T_{2fall} increased from 12.3 to 14.9 ms and T_1 increased from 16 to 21 ms while σ (RMS ω_Q) decreased from 180 to 120 Hz over the range of PG depletion investigated. These results indicate that the IL-1β-induced macromolecular depletion has resulted in changes in the local ordering of the tissue. The effect of mechanical compression of cartilage on the MQF sodium spectral line shapes was also analyzed (135). A nonmagnetic compression cell, which enables the NMR experiments while the tissue is compressed, is employed in this study. Bovine cartilage plugs were subjected to single and MQF sodium NMR spectroscopy during a uni-axial compression at 0.7 MPa for 1 h. Compression, although affected the signal amplitude, did not influence the lineshapes of the SQ and TQF spectra significantly. The DQF spectra showed marked line shape changes in the compressed samples, which were attributed to the reduced RQC in compressed samples.

MQ imaging. Feasibility of performing TQF sodium imaging of articular cartilage was first demonstrated on bovine cartilage samples (142) then TQF imaging of the human knee was performed *in vivo* (143). In the *in vivo* study, a twisted projection imaging (TPI) sequence with an ultra-short 400 μs echo time was employed. Unlike SQ, TQF signal reaches a maximum at a preparation time of $\tau \approx 3$ ms. Images were acquired with a voxel size of 0.5 cm. The total imaging time for a three-dimensional data set of 16 slices was ~20 min and provided images with a SNR of 8:1. Single quantum images were also acquired with a voxel size of 0.06 cm. Total SQ imaging time for a three-dimensional data set with SNR of 16:1 was ~10 min. The TQF signal obtained a particular τ value was fitted to the TQF signal expression to calculate the transverse relaxation times. T_{2rise}^* and T_{2fall}^* (the asterisk indicates a measurement of T_2 in the presence of static B_0 inhomogeneities) measured from these studies are 0.84 and 9.6 ms, respectively. These studies clearly demonstrate the importance of a short-echo imaging sequence like TPI in imaging SQ as well as TQF signal from sodium. It also shows that it takes almost three times the total imaging time to acquire TQF images with the same SNR (but 10 times larger voxels) than SQ images, i.e. the TQF signal is an order of magnitude weaker than the SQ signal. In spite of this, MQF sodium NMR studies are indispensable in the quantification of critical parameters (such as relaxation rates and RQC) that characterize sodium dynamics in biological tissues (137).

Sodium MRI of cartilage fixed charge density (FCD)

As discussed in the Introduction, loss of PG is the initiating event in the OA. The ability to quantify these molecular changes will provide a handle for the early diagnosis and treatment monitoring. Based on the fact that Donnan equilibrium holds for cartilage equilibrated in very dilute solutions, Maroudas *et al.* have shown that FCD of cartilage is correlated to the GAG content of cartilage (145). Since the FCD is counter-balanced by the Na^+ ions, loss of PG (hence GAG and FCD) due to cartilage degeneration results in the loss of sodium ions from the tissue. The loss of the negatively charged PG lowers the FCD in the tissue, thereby releasing positively charged sodium ions. Using ideal Donnan equilibrium conditions, FCD can be related to tissue sodium concentration according to the following equation:

$$FCD \ (mM) = \frac{[Na_{SF}^+]^2}{[Na_{tissue}^+]} - [Na_{tissue}^+] \qquad (24)$$

where $[Na_{SF}^+]$ is the sodium concentration in the synovial fluid and $[Na_{tissue}^+]$ is the sodium concentration in the tissue. $[Na_{SF}^+]$ is typically in the range 140–150 mM, while in phosphate-buffered saline (PBS) it is 154 mM.

Healthy human cartilage FCD ranges from -50 to -250 mM, depending on the age and location in the tissue (136). The FCD from [GAG] can be calculated by the following equation by assuming 2 mol of negative charge per mole of chondroitin sulfate (one from sulfate and one from carboxylate) and a molecular weight of chondroitin sulfate of 502.5 g/mol (136):

$$FCD \ (mM) = -2 \times \frac{[GAG \ (mg/L)]}{502.5 \ (mg/mM)} \qquad (25)$$

Because of very short relaxation time of outer (satellite) transitions, one has to perform spectroscopic and imaging experiments with ultrashort echo times. Since invariably NMR and MRI experiments involve finite pulse lengths, some of the fast decaying components are lost and the signal detected following an RF pulse underestimates the true sodium content. In spite of this, as long as the observed signal is calibrated with appropriate relaxation matched reference sodium phantoms, it is possible to measure absolute sodium content of the tissue.

In an early work, sodium NMR spectroscopy was used to study changes in sodium content and relaxation rates in cartilage. In preliminary studies on cartilage, it was found that loss of PG can cause a decrease in FCD and mobility of sodium ions in the ECM. Paul *et al.* (146) and Jelick *et al.*'s (147) measured sodium relaxation rates using single-quantum NMR in nasal cartilage subjected to proteolytic enzymes, trypsin or papain to degrade PG. In this study, it was observed that both T_1 and T_2 relaxation rates were increased following the trypsin or papain treatment. Sodium NMR visibility in cartilage was determined by measuring sodium content using NMR and comparing it with that measured from inductively coupled plasma emission spectroscopy and it was found that sodium in cartilage was 100% NMR visible (136). Sodium content measured using NMR was then used with ideal Donnan theory to estimate FCD and for calf articular cartilage, near physiological conditions, calculated FCD was found to be -280 ± 30 mM. In the epiphyseal cartilage, FCD varied with the position of origin of the tissue within the joint, ranging from -190 to -350 mM in a manner that correlated with tissue GAG content. Similar variations of sodium concentration were also found in a low-resolution sodium image of intact ulnar epiphyseal cartilage.

Changes in sodium content and relaxation times using single quantum sodium MRI and TQF spectroscopy were investigated (148). Over a 50% PG depletion induced by trypsin from bovine cartilage, sodium content changed almost linearly and T_1 increased from 18 to 26 ms, T_{2s} increased from 7.5 to 12 ms and T_{2f} decreased from 2 to 1 ms. These results indicate that care must be taken to account for these changes in the relaxation times with PG depletion/degeneration of the tissue when sodium MRI is used to quantify tissue [Na]. Also in this study, sodium images of bovine cartilage plugs were presented that displayed reduced sodium intensity with increased PG depletion. However, no attempts were made to calculate the FCD of the tissue.

Low-resolution sodium MRI was acquired from human knee *in vivo* (149) at 1.5 T. Reddy *et al.* (27) were the first to demonstrate the feasibility of acquiring a high-resolution (voxel size of 6.25 µl) three-dimensional data set of sodium images of the knee of healthy human volunteers with excellent SNR (16:1) at 4 T (Figure 8). Sodium images were also compared with corresponding proton images to demonstrate the differences in tissue contrast. It was further demonstrated that high-resolution images obtained on bovine patellar cartilage, half of which was subjected to trypsin-induced PG depletion, clearly demarcated the intact tissue (with high sodium content) from PG-depleted tissue (which had lower sodium content). However, in these studies neither sodium nor FCD measurements were performed.

The effect of mechanical compression on sodium and proton NMR relaxation times of bovine articular cartilage specimens was measured as a function of PG depletion. Uni-axial mechanical compressions were performed with an MR-compatible pressure cell and evaluated dynamically via interleaved one-dimensional proton and sodium MR projection imaging (150). Upon full compression, in normal cartilage, sodium T_1 and T_2 relaxation times were decreased by 38 and 37%, respectively, whereas in PG depleted tissue, following full compression, sodium T_1 and T_2 were decreased by 20 and 39%, respectively.

The sensitivity of sodium and proton MRI in detecting trypsin-induced PG changes in bovine articular cartilage
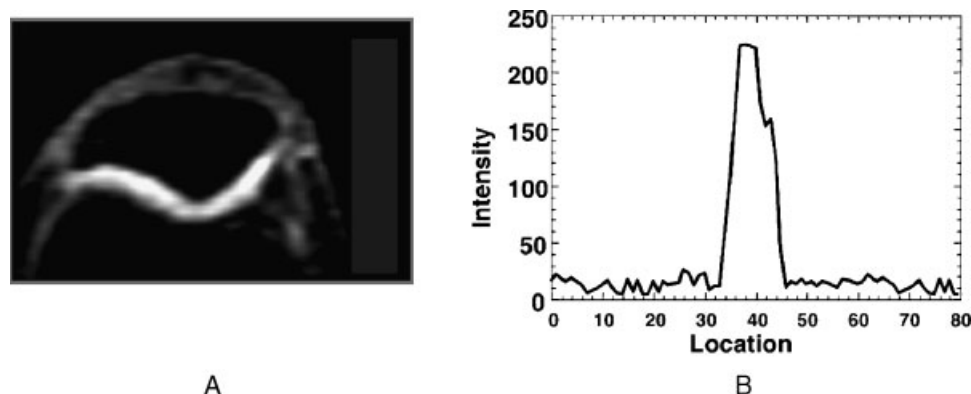
Figure 8. (A) Axial slice of sodium image of a healthy human knee. The high sodium content in articular cartilage is clearly visible. The signal profile across the cartilage is shown in (B) (27).

specimens was investigated at 4 T (151). Over a $\sim 20\%$ PG depletion, sodium image signal change correlated well with the observed PG loss ($r^2 = 0.85$, $p < 0.01$) while proton density-weighted image intensity change did not exhibit a definite trend ($r^2 = 0.10$, $p < 0.8$). The change in proton T_1 and T_2 between depleted and nondepleted tissue regions also did not correlate with PG loss ($r^2 = 0.07$ and $r^2 = 0.06$ respectively). Results from this study indicate that sodium MRI is both sensitive and specific in detecting small changes in PG content, whereas proton density and relaxation properties are not sensitive to small changes in cartilage PG.

Shapiro *et al.* described a method to quantify sodium concentration in cartilage (29). Sodium concentration in bovine patellar cartilage was measured by three different methods: NMR spectroscopy of whole cartilage, NMR spectroscopy of liquefied cartilage in concentrated HCL and inductively coupled plasma emission spectroscopy.

Using a three-dimensional fast gradient-echo (FGRE) pulse sequence, intact bovine patellae were imaged along with relaxation normalized calibration phantoms to map sodium concentration in cartilage (Figure 9). It was found that sodium concentrations in intact articular cartilage ranged from ~ 200 mM on the articular and sub-chondral bone surfaces to 390 mM in the middle with an average of 320 mM in several patellae studied. Average measurements from these sodium maps correlated well with those obtained from the spectroscopic methods and sodium was found to be 100% NMR visible in cartilage plugs. In another study, macromolecular depletion was induced in bovine cartilage plugs using trypsin, and the change in [Na] was measured via sodium MRI using the same approach. Following the imaging experiments, the tissue and PG depletion media were subjected to standard dimethylmethylene blue PG assay. A high correlation (slope $= 0.89$ and $r^2 = 0.81$) between the FCD measure-
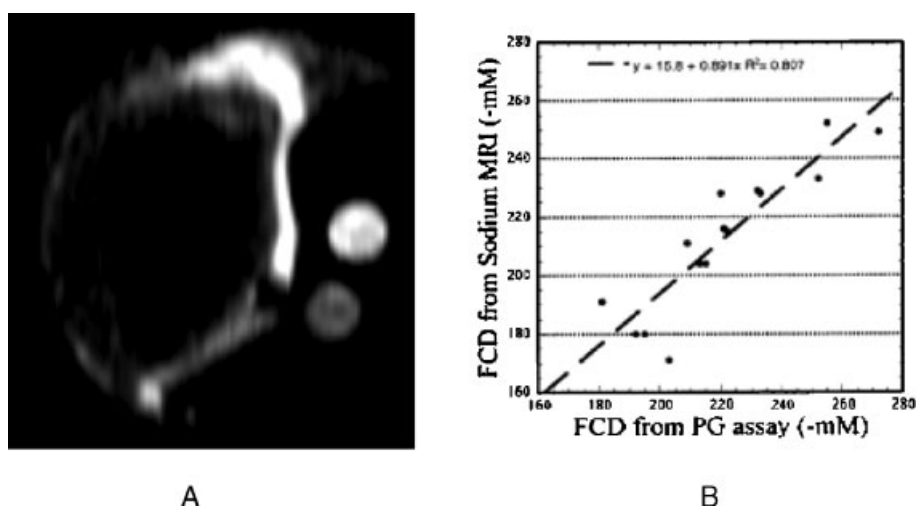
Figure 9. Quantitation and calibration of sodium concentration in articular cartilage. Sodium image of bovine cartilage (A). Trypsin-treated region has low [Na] due to reduced GAG. Circular sodium agarose phantoms that were used to quantify [Na] are also seen in this figure. A plot of FCD measured from sodium MR and that obtained from DMMB assay (B) shows a strong linear correlation between these measurements (29).
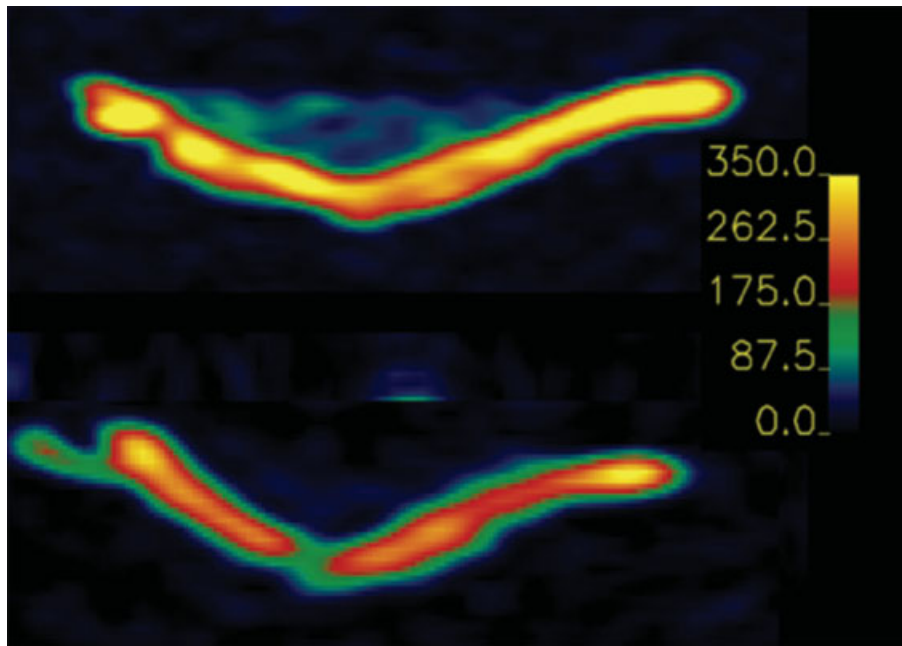
Figure 10. Sodium concentration maps of human patellar cartilage specimens obtained following knee replacement surgery. The top image is from a healthy cartilage while the bottom image is that from an osteoarthritic patient. The scale bar indicates sodium concentration in mM.

ments obtained by ^{23}Na MRI and those obtained by the PG assay (Figure 9) was found. Using the above-described approach involving calibration phantoms, sodium concentration was measured from human cartilage specimens obtained from knee replacement surgery. Clear differences in sodium concentrations in healthy and osteoarthritic specimens were noted (Figure 10).

The same group measured FCD from articular cartilage in the knee of healthy volunteers using two different RF coils, a birdcage coil and a transmit/receive surface coil. High-resolution sodium imaging data (voxel size = 14.6 μL, SNR ≈ 12:1 and a total imaging time of 30 min) obtained with both methods gave similar results, with an average FCD of −158 to −182 mM(152). This variation in FCD has been interpreted as being due to differences in PG content across the tissue. The calibration studies from this work form the basis for computing FCD using sodium MRI. In surface coil experiments, phantom positions were adjusted to match the distance of cartilage from the plane of the surface coil (141).

Although this approach avoids the necessity of compensating for signal drop-off from the inhomogeneous B_1 of a surface coil, any mismatch would lead to erroneous results, a problem that was corrected in a subsequent study by Wheaton *et al.* (30). In this method, the signal intensity of each sodium MR image was corrected for B_1 inhomogeneity, as well as for T_1 and T_2^* weighting, on a pixel-by-pixel basis using a factor derived

from the following equation:

$$S_{\text{cor}}(x,y) = \frac{S_{\text{ori}}(x,y)}{B_{1\text{map}}(x,y)\mathrm{e}^{-TE/T_2^*}(1-\mathrm{e}^{-TR/T_1})} \quad (26)$$

where $S_{\text{cor}}(x,y)$ and $S_{\text{ori}}(x,y)$ are the corrected and original signal intensities, respectively, and $B_{1\text{map}}$ is the value of the B_1 sensitivity map.

The T_1 and T_2^* values of the phantoms measured in progressive saturation experiments were 22 and 8 ms, respectively. The T_1 and T_2^* values used for the human patellar cartilage were 23 and 4.5 ms, respectively, as estimated from data obtained in progressive saturation experiments performed in *ex vivo* bovine patellae. Using this approach, sodium MRI experiments were performed on the knee cartilage of healthy as well as early stage OA patients at 4 T and demonstrated the feasibility of sodium MRI in computing PG loss in early stage OA. The sodium three-dimensional image data set was acquired with a voxel size of 5.3 μL with an SNR of 12:1 in about 20 min. In comparison, it took 30 min to obtain a three-dimensional data set using a volume coil with the same SNR but an increased voxel size of 14.6 μL. With the effects of B_1 inhomogeneity and voxel size accounted for, the surface coil provides an improvement in SNR by a factor of 2. Alternately, an image can be obtained with a surface coil in 25% of the time that it takes to acquire one with a volume coil image with an identical SNR and voxel size. Results from this study revealed that cartilage of healthy subjects had a mean FCD of −182 ± 9 mM

Table 2. Sodium concentration and FCD of healthy human subjects measured from sodium MRI (30)

Sodium concentration (mmol/l)	FCD (mmol/l)
248 ± 39	-175 ± 50
248 ± 29	-175 ± 35
259 ± 24	-187 ± 68
262 ± 60	-192 ± 69
245 ± 48	-171 ± 80
249 ± 49	-176 ± 64
254 ± 36	-182 ± 45
260 ± 60	-190 ± 75
265 ± 56	-196 ± 74

Table 3. FCD measured from sodium MRI of symptomatic osteoarthritic subjects. Percentage change is measured w.r.t the values obtained from healthy subjects (30)

Subject	FCD (mmol/l)[a]	Percentage change[b]
1	-108 ± 56	-41
2	-114 ± 30	-38
2	-144 ± 43	-22

[a]Mean FCDs $\pm$ SDs.
[b]Percentage change in mean FCD from normal value—that is, relative to mean FCD of patellae of the healthy subjects (-182 mmol/l).

(Table 3). Data from the symptomatic subjects shown focal regions of decreased FCD ranging from -108 to -144 mm (Table 3), indicating PG loss. Comparisons of axial sodium images of healthy and symptomatic subjects are also shown in Figure 11. Table 3 and 4.

Borthakur and co-workers demonstrated the feasibility of quantifying sodium in the human wrist joint *in vivo* on a 4 T whole-body scanner (153). Employing a fast gradient echo sequence, a three-dimensional data set of 16 slices with 16 averages was obtained in 22 min. The pixel size was 6 μL and it was found that, in healthy human wrist, sodium concentration ranged from 115 to 150 mm in noncartilaginous regions and from 200 to 210 mm in cartilaginous regions. Wheaton *et al.* (154) also demonstrated the
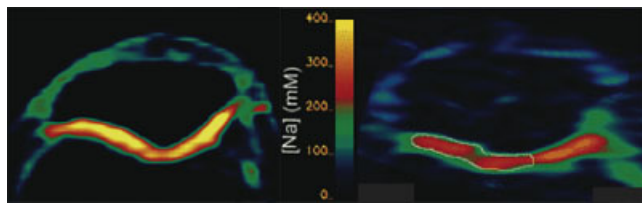
Figure 11. Sodium images of the human knee joint *in vivo* acquired in the axial plane. Cartilage in the patellar–femoral joint is visible in yellow in the image on the left. The scale bar indicates sodium concentration in mm. The image on the left was obtained on a healthy volunteer where uniform high sodium content was observed. The right image is from a symptomatic osteoarthritic subject, demonstrating heterogeneous and low [Na] that reflects a loss of GAG in this subject (30).

**Table 4. $T_{1\rho}$ relaxation data from osteoarthritic subjects (239)**

Subjects	$T_{1\rho}$ (ms), mean $\pm$ SD	$T_{1\rho}$ elevation (%)
1	63 ± 4	26
2	64 ± 3	28
3	65 ± 5	30
4	72 ± 4	44
5	75 ± 6	50
6	95 ± 12	90

feasibility of detecting cytokine-induced arthritic changes in an animal model using sodium MRI. In this study, a biochemical condition similar to OA was created by an intra-articular injection of recombinant porcine interleukin-1β (IL-1β) into the knee joint of Yorkshire pigs. The contralateral knee joint was given a saline injection to serve as the control. Sodium MRI data was acquired at 4 T after 6 h following the injection of IL-1β. Following *in vivo* imaging, the tissue and joint fluid were harvested and subjected to *in vitro* sodium MRI and histologic and immunohistochemical analyses as independent measurements of the cytokine activity and PG loss. Sodium images obtained from treated and untreated joints of pigs are shown in Figure 12. Sodium image data was used to generate FCD maps. On average, the FCD of cytokine-treated cartilage was 49% lower than that of saline-treated cartilage, reflecting a loss of PG content. These results were supported by histologic and immunochemical findings, most notably a reduction in staining for PG and an increase in matrix metalloproteinases in the synovial fluid.

Summary

The sodium spectroscopy work described above was performed at varying field strengths ranging from 2 to 9.4 T. MQF spectroscopy is ideally suited for measuring all the parameters that govern sodium dynamics in cartilage. These are indispensable in obtaining accurate quantification of relaxation rates and RQC, and hence information about ordered tissue. However, the order of magnitude lower SNR of MQF signals restricts them to spectroscopy mode. Most MQF spectroscopy to date has been carried out at magnetic fields greater than 4 T.

The majority of sodium MRI experiments, however, have been performed at 3 and 4 T. In these studies, three-dimensional sodium MRI of 16 slices in the knee joint was performed with volume RF coils in less than half an hour with a voxel size of 6 μL with an SNR of 12:1. The echo times employed in these experiments was a little over 2 ms. However, by exploiting the increased sensitivity of surface coils, it was possible to improve the SNR to 16:1 and the imaging time was reduced to less than 20 min. Sodium imaging at 4 T clearly demonstrated the feasibility of measuring cartilage FCD *in vivo* in
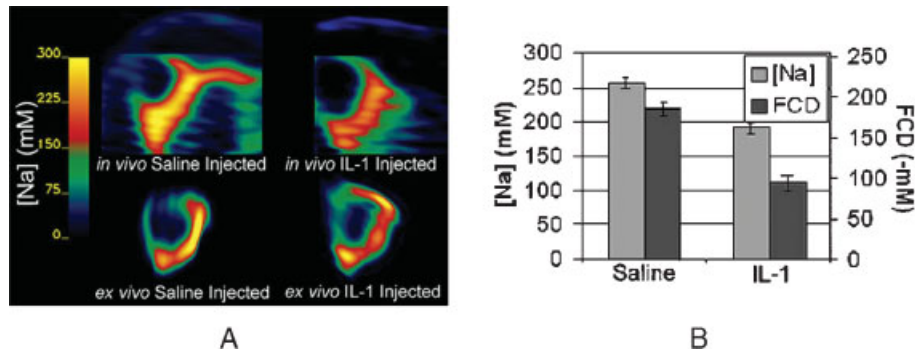
Figure 12. Sodium concentration maps of saline and IL-1β-treated knee joints in swine. The maps shown were acquired from a single specimen, but are representative of the data acquired from all six animals. The resolution of the *in vivo* and *ex vivo* maps were kept identical to allow direct comparison (154). [Na] and FCD from cartilage of saline-treated and IL-1β-treated joints of all six animals (B) demonstrates a significant reduction in FCD from treated cartilage.

healthy as well as osteoarthritic patients. Further, its utility in measuring FCD changes in an animal model of OA has been described. The major advantage of sodium MRI, especially of cartilage, is that it is highly specific to PG content and, since the sodium from surrounding structures in the joint is low (<50 mM), cartilage can be visualized with very high contrast without the requirement for any exogenous contrast agent such as that in dGEMRIC (155). It can be used to quantify early molecular changes in osteoarthritis.

The disadvantages of sodium MRI are that it requires field strengths of ≥ 3 T to obtain quality sodium images that enable accurate quantification of cartilage FCD. Furthermore, due to the limitations of gradient strengths and other hardware requirements, most of the sodium imaging experiments reviewed here employed echo times of ≥ 2 ms. Since the T_{2f} of cartilage lies in the range 1–2 ms, substantial signal is lost before the acquisition. This is a major contributor to the low SNR of sodium compared with conventional proton MRI. Additionally, the sodium gyromagnetic ratio, γ, is one-quarter that of protons, hence sodium MRI requires four times stronger gradients to obtain images with identical resolution to that of proton MRI. With the exception of MQF-prepared TPI imaging, sodium MQF imaging is currently not clinically feasible due to the low sensitivity of the technique and has therefore been relegated to spectroscopic methods to quantify structures of materials and specimens.

However, recent advances in the gradient technology (with a gradient strength of >4 G/cm) may enable one to achieve ultrashort *TE* ($<200\,\mu s$) that can significantly improve resolution and SNR. Radiofrequency coil technology (multiple channel capability) and parallel imaging approaches such as SENSE (156) and SMASH (157) and tuned pre-amplifiers would further contribute to high SNR. These advances may potentially make clinical sodium MRI feasible on 3 T scanners. Further, the recent

proliferation of 7 T whole-body MRI scanners in clinical research centers could have a significant impact on sodium MRI and its potential for clinical use. Since SNR scales as $B_0^{7/2}$ (158–161) and the lack of B_1 penetration and B_0 susceptibility are issues that plague proton imaging, sodium MRI can be particularly advantageous at higher fields. Further, unlike proton T_1, which increases with field, as the T_1 of sodium is predominantly due to quadrupolar interaction, it may not change appreciably at higher field. This retains the rapid averaging capability of sodium MRI even at high fields. The low γ of sodium will also mean significantly lower power deposition compared with proton imaging. It is therefore very likely that, with the improved SNR, sodium MRI at 7 T and higher fields would emerge as a robust tool for quantitative imaging of cartilage integrity.
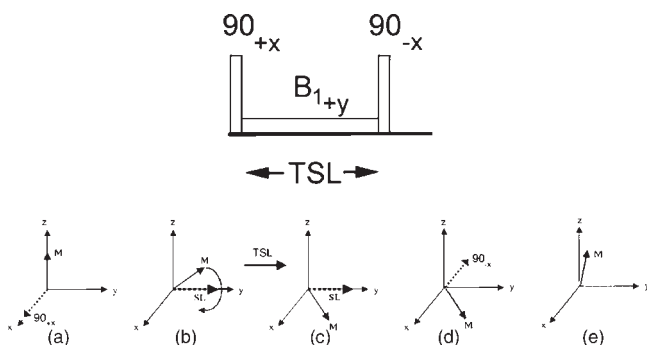
$T_{1\rho}$ MRI

In $T_{1\rho}$ MRI, a long-duration, low-power RF pulse referred to as the 'spin-lock' (SL) pulse is applied to the magnetization in the transverse plane. The magnetization undergoes relaxation in the presence of the applied B_1 field in the rotating frame, a situation similar to that of the longitudinal magnetization in the B_0 field. This spin-locked magnetization will relax with a time constant $T_{1\rho}$, the spin-lattice relaxation in the rotating frame, during the time of the spin-lock pulse (TSL). The B_1 field attenuates the effect of dipolar relaxation, static dipolar coupling, chemical exchange and background gradients on the signal. $T_{1\rho}$ is always greater than T_2. In a typical $T_{1\rho}$ MRI experiment, the TSL time is incremented while the amplitude of SL pulse ($\gamma B_1 \approx 0.1$ to a few kHz) is fixed. Alternatively, the measurement of $T_{1\rho}$ as a function of the B_1 amplitude, for a fixed spin-lock length, is also possible. The '$T_{1\rho}$-dispersion' curve obtained in this case is
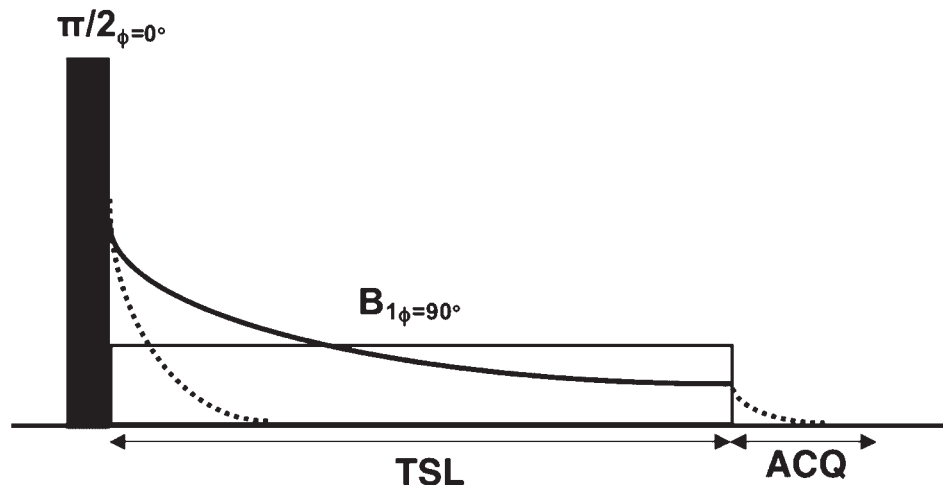
Figure 13. Pulse sequence for spin-locking magnetization in the transverse plane. Initially, a $\pi/2$ pulse flips the longitudinal magnetization into the transverse plane. The open rectangle pulse represents the spin lock (SL) pulse and TSL and B_1 are its duration and amplitude, respectively. The dotted line represents the decay of the magnetization in the absence of spin-locking and is governed by time constant, T_2^*. However, if the magnetization is spin-locked, it decays according to $T_{1\rho}$ (solid line) for the duration of time TSL. But after the SL pulse the decay is again T_2^*, during which time the signal may be acquired.

governed by the spectral density components of the sample that are in the neighborhood of γB_1.

Measurement of the MR signal following the SL pulse (Figure 13) is ideal for spectroscopic measurement of $T_{1\rho}$ of a sample. However for imaging applications, it is often more convenient to prepare the magnetization using a pulse cluster shown in Figure 14. The thermal equilibrium magnetization vector (M_0), initially along the z-axis (panel a), is nutated by the first hard $90°$ pulse which is applied along the x-axis in the rotating frame of reference, into the transverse plane (panel b). The magnetization, now along the y-axis, is immediately spin-locked by the SL pulse (panel c). For the duration of the TSL period, the magnetization decays with a time constant $T_{1\rho}$ (panel d). The magnetization thereby becomes '$T_{1\rho}$-prepared'

and results in a $T_{1\rho}$-weighted signal as a function TSL. This $T_{1\rho}$-prepared magnetization is then restored to the longitudinal axis by the second hard $90°$ applied along the negative x-axis (panel e) and can be spatially encoded by appending any imaging pulse sequence to this $T_{1\rho}$ pulse cluster. A pixel-by-pixel fit of the spin-locked signal to an appropriate expression provides $T_{1\rho}$. In the above description, on-resonance condition is assumed. The $T_{1\rho}$ experiment can also be performed in off-resonance condition to quantify $T_{1\rho}^{\text{off}}$, where the magnetization is spin-locked at an effective field given by:

$$\omega_{\text{eff}} = \sqrt{\omega_1 + \Delta\omega} \qquad (27)$$

where $\Delta\omega$ is the resonance offset.

In biological tissues, off-resonance RF pulse, in addition to spin-locking, also leads to 'magnetization transfer' effect (162) which may complicate the analysis of $T_{1\rho}^{\text{off}}$. The details of off-resonance experiments can be found in the literature (163–165). However, for the rest of the sections we restrict ourselves to describing $T_{1\rho}$ in the on-resonance condition. $T_{1\rho}$ studies in solution-state NMR have been reviewed extensively (166–168). There has been a considerable amount of work on biological tissues using $T_{1\rho}$-spectroscopy and imaging dealing with tumors, muscle, myocardium, blood flow and cartilage (26,165,169–179).

Figure 14. Radiofrequency pulse cluster for $T_{1\rho}$ pre-encoding (left). TSL and B_1 are the length and amplitude of the spin-lock (SL) pulse, respectively. Vector diagram (below) of the evolution of the magnetization during the spin-lock pulse cluster.

Imaging pulse sequences

Two-dimensional $T_{1\rho}$ MRI. Initial $T_{1\rho}$ imaging experiments were performed on articular cartilage using a $T_{1\rho}$

sequence based on a spin-echo, or SE (24), and fast spin echo, or FSE (26). Both these sequences have been implemented on multiple clinical MRI systems and field strengths to produce a single-slice $T_{1\rho}$-weighted image. A typical image data set containing four or five images acquired at different TSL times can be fitted to the following expression to generate a pixel-by-pixel $T_{1\rho}$map:

$$S_y(\text{TSL}) = S_0 \exp\left(\frac{-\text{TSL}}{T_{1\rho}}\right) + C \qquad (28)$$

Three-dimensional $T_{1\rho}$ MRI. Recently, a $T_{1\rho}$-prepared three-dimensional gradient-echo (GRE) based pulse sequence was developed and implemented using either adiabatic pulses (131) or hard pulses (180) in the $T_{1\rho}$ preparation period. In the three-dimensional sequence, the magnetization is $T_{1\rho}$-prepared just as in the case of the two-dimensional sequences. However, in place of the 90° slice-selective pulse of the SE or FSE sequence, a small angle α pulse is used instead to excite a slab; this is followed by a conventional three-dimensional GE readout.

Signal intensities from three-dimensional data sets obtained at varying spin-lock lengths are fitted to the following signal expression:

$$S(TSL) \propto \frac{e^{\frac{-TSL}{T_{1\rho}}}\left(1 - e^{\frac{-(TR-TSL)}{T_1}}\right)}{1 - e^{\frac{-TSL}{T_{1\rho}}} e^{\frac{-(TR-TSL)}{T_1}} \cos\alpha} \sin\alpha \qquad (29)$$

where $S(TSL), TSL, TR, T_1$ and α represent signal intensity at a given spin-lock duration and frequency, spin-lock length, pulse repetition time, longitudinal relaxation time and flip angle of the slice selective pulse, respectively.

Like most three-dimensional GE-based sequences, the three-dimensional $T_{1\rho}$ sequence enables rapid data collection but produces images with a reduced SNR compared with SE-based images. Further, to accelerate the acquisition, a short *TR* is typically employed, which introduces significant T_1 weighting in the resultant image and may obscure $T_{1\rho}$-based contrast.

Advantages of this sequence are that it provides volumetric $T_{1\rho}$ maps and that one of the early data set can be used to compute cartilage volume.

Multi-slice $T_{1\rho}$ MRI with spin-echo readout. To overcome the limitations, such as low SNR and poor $T_{1\rho}$ contrast, associated with volumetric data acquisition with a three-dimensional $T_{1\rho}$ prepared sequence, a two-dimensional multi-slice spin-lock (MS-SL) pulse sequence was developed (181). One of the challenges in implementing the $T_{1\rho}$ sequence in multi-slice mode is due to the nonselective nature of the spin-lock pulse, which saturates the longitudinal magnetization from nonexcited regions. In this sequence, saturation of longitudinal magnetization by the application of non-selective SL pulses is experimentally measured and

theoretically modeled as $T_{2\rho}$ decay. The saturation data was used to correct the image data as a function of the SL pulse duration to make quantitative measurements of $T_{1\rho}$. It was found that $T_{1\rho}$ measured using saturation corrected MS-SL data is identical to that measured using SS-SL sequence (182). $T_{1\rho}$ relaxation maps are computed for each slice by fitting the image data pixel-by-pixel to eqn (28). During the period between each SL pulse, $\tau = TR/N$, where N is the total number of slices acquired, the longitudinal magnetization recovers according to T_1. After each τ delay, the magnetization becomes saturated by a factor of M^{sat}. Therefore, at the end of the Nth re-growth delay period, the longitudinal magnetization, $M_{z,n}$, is given by:

$$M_{z,n} = M^{\text{sat}}(TSL)$$
$$\times \left[M_{z,n-1} \exp\left(\frac{-\tau}{T_1}\right) + M_0\left(1 - \exp\left(\frac{-\tau}{T_1}\right)\right)\right] \qquad (30)$$

where

$$M^{\text{sat}}(TSL) = \exp\left(\frac{-TSL}{T_{2\rho}}\right) \qquad (31)$$

and

$$\frac{1}{T_{2\rho}} = \frac{1}{2}\left[\frac{1}{T_1} + \frac{1}{T_2}\right] \qquad (32)$$

Multi-slice $T_{1\rho}$ MRI with spiral readout. Recently a multi-slice $T_{1\rho}$ mapping with spiral readout was implemented at 3 T (183,238). In this sequence, $T_{1\rho}$-prepared magnetization was read by a multi-slice spiral readout. Acquiring a second image that has an inverted longitudinal magnetization compensated for T_1-weighting. The total imaging time for collecting a three-dimensional data set of 14–16 slices was ~13 min. Representative data obtained with this sequence is shown in Figure 34 and was limited to an axial orientation because spiral acquisition does not allow the use of an anti-aliasing filter that is necessary for sagittal or coronal plane acquisition with a knee coil.

Rapid volumetric $T_{1\rho}$ MRI with SSFP readout. In order to implement any research sequence in a clinical setting for quantitative imaging, it should provide three-dimensional coverage and have high precision and high temporal efficiency without exceeding SAR limits. Since $T_{1\rho}$ mapping involves the collection of at least four three-dimensional data sets at varying SL times, it is inherently inefficient. Although the three-dimensional FGRE and multi-slice sequences described above have been implemented on clinical scanners, they typically require 20–25 min to gather a single $T_{1\rho}$ map. Further, three-dimensional $T_{1\rho}$ maps are typically collected with 2–4 mm slice thickness as it is too time-consuming to
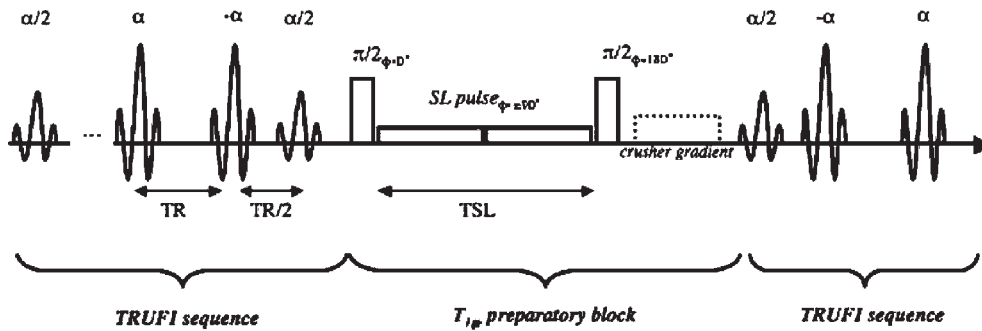
Figure 15. The pulse sequence for acquiring $T_{1\rho}$-weighted true FISP (or TRUFI) images. The steady-state magnetization is stored in the z-direction by the last $\alpha/2$ pulse of the TRUFI sequence and then recalled by the $T_{1\rho}$ preparatory cluster and returned to the z-axis by the second hard $\pi/2$ pulse. A string crusher gradient (indicated by the dotted box) in then applied at that point to destroy any residual magnetization in the transverse plane.

collect three-dimensional maps with isotropic voxel sizes. Therefore, at least two views, e.g. sagittal and axial, are required to properly visualize anatomical structures in three-dimensional $T_{1\rho}$ maps.

To accomplish this, we recently incorporated $T_{1\rho}$ imaging with a balanced steady-state true precession (SSFP or true FISP or TRUFI) pulse sequence (192). The performance of this sequence (Figure 15) was verified by comparing the $T_{1\rho}$ relaxation maps obtained with this sequence with that of a standard single slice $T_{1\rho}$-TSE sequence. The error in computing $T_{1\rho}$ with $T_{1\rho}$-TRUFI was $\sim$5%. At the same time, the total imaging time for collecting three-dimensional $T_{1\rho}$ maps in both axial and sagittal views was $\sim$20 min. The average $T_{1\rho}$ of cartilage was insignificantly different between the $T_{1\rho}$-TRUFI (39.4 ms) and $T_{1\rho}$-TSE (38.4 ms) readout methods (Figure 16). Integrating this sequence with parallel imaging techniques is expected to further reduce imaging time.

SAR considerations

During MRI, the power of the applied RF pulses has to be monitored at all times to ensure that the energy deposited in the patient remains below Food and Drug Administration (FDA) mandated safety levels for the specific absorption rate. As a safety precaution, invariably all the clinical scanners have built in mechanism to stop the scan if the FDA-mandated power level is exceeded at any point. While the most accurate method would be to measure the power output to the RF coil in real time, *a priori* knowledge of the specific absorption rate (SAR) of a pulse sequence can provide additional safety and save valuable experiment time. A method to calculate SAR has been proposed by Collins *et al.* (193), in which the SAR was calculated from the electric field generated by a typical quadrature coil on a simulated head of known tissue electrical properties and material density. Using this method, the maximum SAR for a 3 ms long
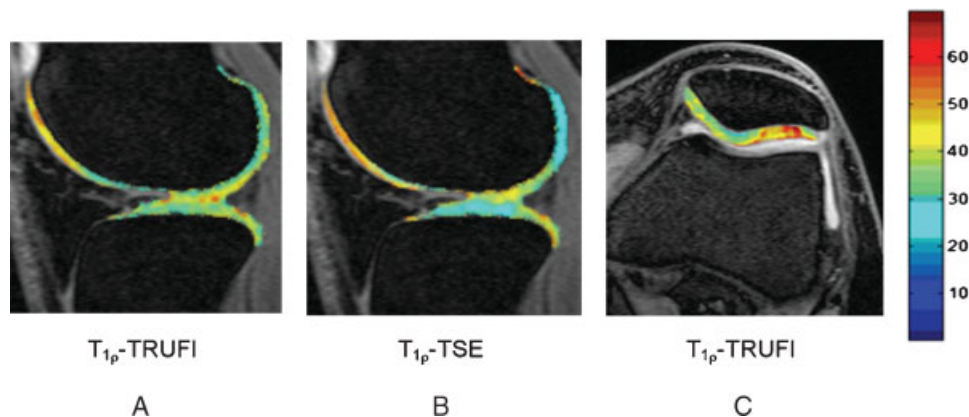
Figure 16. Sagittal $T_{1\rho}$-TRUFI (A) and $T_{1\rho}$-TSE (B) maps (in color) are overlaid on a grayscale image of the femor–tibial cartilage of a 22-year-old healthy volunteer. Also shown is an axial $T_{1\rho}$-TRUFI map from another healthy volunteer's patellar–femoral cartilage (C). The color bar on the right indicates $T_{1\rho}$ values in milliseconds. Although reduced values are observed in parts of the $T_{1\rho}$-TSE map, the average $T_{1\rho}$ is not significantly different between the $T_{1\rho}$–TRUFI (39.4 ms) and $T_{1\rho}$–TSE (38.4 ms) maps. A region of elevated $T_{1\rho}$ is evident on the lateral facet of the patellar cartilage in (C) and could be an indication of early-stage cartilage degeneration.

rectangular pulse that achieves a flip angle of 90°, or SAR(90°,3), in a simulated quadrature head coil was determined to be 1.46 W/kg in 1 g of tissue. The value was actually smaller (0.708 W/kg in 1 g of tissue) if a sphere containing only muscle tissue was used in the simulation instead. The SAR, of a single pulse of flip angle α and duration τ (in ms), may be calculated using the eqn (193):

$$\text{SAR}(\alpha, \tau) = f\left(\frac{3}{\tau}\right)^2 \left(\frac{\alpha}{90°}\right)^2 \text{SAR}(90°, 3) \qquad (33)$$

where f is a shape factor and equals 1 for a hard pulse or equals the width of the central lobe at the zero crossing point for a sinc pulse.

The minimum *TR* for the pulse sequence was determined from the equation:

$$TR_{\min} = \frac{\sum_{n=1}^{N} \text{SAR}(\alpha_n, \tau_n) \times \tau_n}{\text{SAR}_{\text{FDA}}} \qquad (34)$$

where $\text{SAR}(\alpha_n, \tau_n)$ was calculated from eqn (33) for all $N = 4$ pulses in the sequence and SAR_{FDA} is the FDA-suggested maximum *SAR* level and equals 12 W/kg in 1 g of tissue in the extremities (193).

SAR measurements for three-dimensional $T_{1\rho}$-weighted MRI at 1.5 T are described. The signal expression required to fit the data is introduced and critical analysis of energy deposition of the RF pulses in the sequence was performed and validated with experimental data on a known phantom. The temperature increase in the phantom resulting from the sequence was 0.015°C, which is well below the established safety guidelines. Performance of the three-dimensional $T_{1\rho}$ pulse sequence was shown by computing $T_{1\rho}$ maps of bovine patellar cartilage and comparing the data with that obtained with two-dimensional $T_{1\rho}$ mapping sequence. The calculated $T_{1\rho}$ of articular cartilage in the specimen was similar for both three-dimensional and two-dimensional methods (84 ± 2 and 80 ± 3 ms, respectively). Three-dimensional $T_{1\rho}$-weighted images obtained from human knee joint *in vivo* demonstrate an improved contrast between cartilage and surrounding structures.

A low SAR $T_{1\rho}$ pulse sequence

Recently, a reduced SAR version of a $T_{1\rho}$ mapping sequence was developed (194). This method exploits a partial *k*-space acquisition approach in which a full power spin-lock pulse is applied only to the central phase-encode lines of *k*-space, while the remaining phase encode lines receive a low-power (50% amplitude of the maximum) spin-lock pulse. Acquisitions of high- and low-power phase-encode lines are interleaved temporally to minimize average power deposition. This strategy ensures that the majority of signal energy in the central portion of the *k*-space was fully $T_{1\rho}$-weighted, while at the same time the overall SAR of the acquisition was lower,

and consequently, total imaging time was reduced. It was demonstrated that, using this approach in the human brain, the SAR could be reduced by 40% while the measurements of $T_{1\rho}$ changed by only 2%. Similarly, a 'keyhole' acquisition approach was exploited in reducing the overall imaging time by 40% for $T_{1\rho}$ mapping (195). These approaches can be combined with any of the acquisition sequences described above to reduce SAR and/or improve temporal resolution.

Mechanism of $T_{1\rho}$ relaxation in cartilage

The spin interactions with different internal Hamiltonians (*J*-coupling, chemical shift, dipole–dipole interaction, chemical exchange, etc.) will take place in the presence of continuous RF fields of SL pulse, thereby imparting time dependence to the interaction Hamiltonians. Thus the RF field not only introduces time dependence into the Hamiltonian, but also changes the axis of quantization of the spins and modifies other characteristics that determine the relaxation behavior. Redfield first demonstrated the spin-lock phenomenon in solid materials and presented relaxation theory in the presence of a time-dependent Hamiltonian (196,197). Later, several investigators developed the theory for applications in liquid state in different conditions (167).

The interactions that are studied using this methodology can be broadly categorized into (i) scalar-coupling, (ii) dipole–dipole and (iii) chemical exchange processes. In NMR, the spin-lattice relaxation in the laboratory frame or rotating frame, the dynamical information is contained in spectral density functions. Depending upon the method used, the experiment may be simultaneously sensitive to more than one time scale. One method of probing relaxation mechanisms is to use the so-called NMR 'dispersion', which measures relaxation times at different field strengths using a field cycling approach (198). Although this method has provided insights into relaxation phenomena of tissues, it is limited to measuring T_1 at different field strengths. With this method, study of slow motions on the order of kHz is difficult as they suffer from poor SNR. On the other hand, $T_{1\rho}$ experiments can be performed at high fields and have the potential to provide information about the low frequency motions (~few kHz) in biological systems with high SNR. Although there is abundant literature on studies of T_1 and T_2 relaxation times in biological systems, there are relatively few studies on $T_{1\rho}$ mechanisms in biological tissues at high static fields.

In biological tissues, the $T_{1\rho}$ relaxation may have contributions from several interactions. Depending upon the tissue type, more than one mechanism may be operative simultaneously but with different relative contributions. In what follows, a brief description of individual relaxation mechanism that may be operative in biological tissues is provided.

Dipolar relaxation. Since the first introduction by Redfield, spin-lattice relaxation in the rotating frame has been studied extensively under different limiting conditions. Using the density matrix approach assuming stochastic time dependence for the lattice variables, a general equation representing the contribution of nuclear spin relaxation due to fluctuating magnetic dipoles to $T_{1\rho}$, in weak collision limit was obtained by Kelly and Sholl (199):

$$\frac{1}{T_{1\rho}} = \frac{3}{8}\gamma^4\hbar^2 I(I+1)$$
$$\times \left[\frac{\tau_r}{1+4\omega_1^2\tau_r^2} + 10\frac{\tau_r}{1+\omega_0^2\tau_r^2} + \frac{\tau_r}{1+4\omega_0^2\tau_r^2}\right] \quad (35)$$

and

$$\frac{1}{T_1} = \frac{3}{2}\gamma^4\hbar^2 I(I+1)\left[\frac{\tau_r}{1+\omega_0^2\tau_r^2} + \frac{\tau_r}{1+4\omega_0^2\tau_r^2}\right] \quad (36)$$

where I is the nuclear spin number, $\omega_1 = \gamma B_1$, and $\omega_0 = \gamma B_0$, γ is the gyromagnetic ratio of the nuclei, B_0 the Zeeman static magnetic field and τ_r is the molecular rotational correlation time.

From the $T_{1\rho}$ equation, it is clear that it is sensitive to two different time scales, ω_1 and ω_0. Therefore, if the experiment is carried out at constant Zeeman field, the last two terms of the equation will be constant. The last two terms, representing the spectral densities at ω_0 and $2\omega_0$ (J_1 and J_2) can be determined from combination of T_1 and T_{1D} (Jeener–Broekaert) experiments at the same Zeeman field. Then $J(2\omega_1)$ can be determined by measuring $1/T_{1\rho}$ at different B_1 fields. In general, dipolar relaxation is mostly governed by molecular rotational motion with rotational correlation time τ_r. In biological tissues, frequency dependence on relaxation rates, relaxation-dispersion, may arise from (i) rotational motion of a fraction of water bound to proteins, (ii) exchange of protons on macromolecules with bulk water and (iii) the nonaveraged residual dipolar interaction (RDI) of spin associated with oriented macromolecules in the tissue.

Effect of diffusion. It has been shown that, in biological tissues, diffusion (rotational and translational) contributions to all relaxation rates are constant and independent of frequency (200).

Effect of chemical exchange. In proteins and biological tissues, exchange between protons in different environments is expected to contribute to $T_{1\rho}$ relaxation. Prominent exchange mechanisms may be classified as exchange between (i) water molecules in bulk and hydration water on proteins, (ii) hydration water and -OH and -NH protons on proteins (exchange between two sites) and (iii) $H_2{}^{17}O$ and $H_2{}^{16}O$ molecules (scalar relaxation).

Simple exchange of protons between water molecules causes $T_{1\rho}$ dispersion provided the exchange times (τ_e)

satisfy the condition that $\omega_1^2\tau_e^2 \approx 1$. When this is valid, $\omega_0^2\tau_e^2 \gg 1$. This type of exchange contribution to the T_1 relaxation rate is zero, it contributes a constant to the T_2 relaxation rate [$1/T_1 \approx 0$: $1/T_2 \approx A\tau_e$] and the $T_{1\rho}$ relaxation rate has a frequency dependence form as shown below:

$$\frac{1}{T_{1\rho}} \approx A\frac{\tau_e}{1+\omega_1^2\tau_e^2} \quad (37)$$

Several groups have investigated exchange mechanisms in a variety of cases using $T_{1\rho}$ and Carr–Purcell–Meiboom–Gill (CPMG) pulse sequences (201–206). Hills and Virta *et al.* (207–213) performed $T_{1\rho}$ studies on proteins, carbohydrates, gelatin, glucose and dextran solutions and demonstrated that the primary mechanism operative in these systems is the exchange between protons in -OH groups on carbohydrates and -OH groups on water molecules. Starting with the Bloch–McConnell equations, Trott *et al.* have derived new expressions for the spin-lattice relaxation rate constant in the rotating frame ($1/T_{1\rho}$), $R_{1\rho}$, for chemical exchange between two sites, A and B, that have distinct magnetic environments and Larmor frequencies (214,215).

$$R_{1\rho} = R_1\cos^2\theta + R_2\sin^2\theta + \frac{\sin^2\theta p_a p_b \delta^2 k}{\omega_{aeff}^2\omega_{beff}^2/\omega_{eff}^2 + k^2} \quad (38)$$

$$\delta = \delta_b - \delta_a = \Omega_b - \Omega_a$$
$$\omega_{aeff}^2 = \delta_a^2 + \omega_1^2 \quad (39)$$
$$\omega_{beff}^2 = \delta_b^2 + \omega_1^2$$

$$\omega_{eff}^2 = \Delta\Omega^2 + \omega_1^2$$
$$\theta = \arctan\left(\frac{\omega_1}{\Delta\Omega}\right) \quad (40)$$

$$\overline{\Omega} = p_a\Omega_a + p_b\Omega_b$$
$$\Delta\Omega = \overline{\Omega} - \omega_{rf} \quad (41)$$

where R_1 and R_2 are the intrinsic longitudinal and transverse relaxation rates respectively, resulting from processes other than chemical exchange.

If R_1 and R_2 are assumed to be population averages, then the effect of difference between the intrinsic relaxation rates for species in sites A and B on $R_{1\rho}$ is negligible. Ω_a and Ω_b are the Larmor precession frequencies of sites A and B, respectively, and $k = k_a + k_b$ is the exchange rate and site populations are $p_a = k_b/k$ and $p_b = k_a/k$.

This equation is simplified if one of the sites is much more populated than the other. In this asymmetric populations limit, $p_a \gg p_b$; $\delta_a \approx \Delta\Omega$ and $\omega_{eff} \approx \omega_{aeff}$:

$$R_{1\rho} = R_1\cos^2\theta + R_2\sin^2\theta + \frac{\sin^2\theta p_a p_b \delta^2 k}{\omega_{beff}^2 + k^2} \quad (42)$$

This equation generalizes the expression previously reported for the special case $R_1 = R_2$ and $\overline{\Omega} = \omega_{rf}$. When

'θ' is 90°, which is the on-resonance condition, then it simplifies to more familiar expression with R_2 representing 'exchange free' transverse relaxation rate:

$$R_{1\rho} = R_2 + \frac{p_a p_b \delta^2 k}{\omega_1^2 + k^2} \qquad (43)$$

These results are accurate provided that the spin relaxation decay is dominated by a single exponential damping constant, and are applicable to a wider range of conditions than existing theoretical descriptions. These $R_{1\rho}$, expressions will be useful in analyzing experimental data when exchange is not fast and site populations are unequal. Since this expression involves a chemical-shift difference term that is field-dependent, there will be an increase in $R_{1\rho}$ with field strength. Field-dependent $T_{1\rho}$ relaxation studies can also be used to tease out any contribution from exchange between two chemically shifted nuclei. This exchange model has been used to analyze $T_{1\rho}$ dispersion in cartilage (216).

Scalar relaxation (74). *(a) Scalar relaxation of the first kind:* this is described in the context of two spins, I and S, that are scalar coupled with a spin–spin coupling constant J_{IS}. The exchange time constant between these two spins is denoted by τ_e. If the relaxation time, T_1, of each spin and τ_e is much larger than $1/(2\pi J_{IS})$ then the resonance line of each spin acquires a multiplet structure due to coupling with each other. If $1/T_1$ of either spin or $1/\tau_e$ is much larger than $2\pi J$, then the multiplet structure disappears and each spin will exhibit a single line spectrum and the scalar coupling (J_{IS}) can become a mechanism of relaxation. When the coupling is modulated by (fast) exchange, this type of relaxation is referred to as 'scalar relaxation of the first kind'.

(b) Scalar relaxation of the second kind: if the S spin's T_1 is much shorter than $1/(2^\pi J_{IS})$ and τ_e due to anything other than scalar coupling, then the splitting due to scalar coupling is absent and the I spin spectrum will have a single resonance line. This type of situation can occur if S is quadrupolar nuclei. Quadrupolar nuclei couple to the EFG within the molecule in which they are present. In solution state, the fast rotation of the molecules produces a rotating EFG, which leads to a fluctuation of the local magnetic field experienced by the nuclei and results in a short T_1. When the rate of these fluctuating local magnetic fields of quadrupolar nuclei is greater than the coupling constant, the splitting will average to zero. This type of relaxation mechanism is known as 'scalar relaxation of the second kind'.

Contribution of both these types of scalar relaxation leads to broadening of the I spins' spectral lines and an identical effect on the relaxation rate of the I nuclei. An example of scalar relaxation of the first kind is proton relaxation in $H_2{}^{17}O$. The ^{17}O nucleus has spin 5/2 and its T_1 is dominated by quadrupolar relaxation shortening T_1 to ~4 ms. Protons on $H_2{}^{17}O$ are in constant exchange with

those on $H_2{}^{16}O$ and at neutral pH $\tau_e \approx 1.0$ ms. Taking into consideration the concentration differences between $H_2{}^{17}O$ and $H_2{}^{16}O$, Meiboom (201) derived equations for proton $T_{1\rho}$ in ^{17}O-enriched water under conditions of [^{17}O–^1H] scalar coupling and chemical exchange. In the fast-proton-exchange regime (i.e. $\delta\tau \ll 1$, where 2δ is the J-coupling constant and τ is the proton exchange time), it can be shown that:

$$\frac{1}{T_{1\rho}(\omega_1)} = \frac{1}{T_{1\rho}^0} + \tau \sum_i \frac{p_i \delta_i^2}{(1 + \tau^2 \omega_1^2)} \qquad (44)$$

where p_i is the relative intensity of the *i*th spectral line of an ^{17}O multiplet, and $1/T_{1\rho}^0$ is the rate of all ^{17}O-independent relaxation processes.

Substituting for δ_I and letting $p_i = f/6$, where f is the ^{17}O atom fraction in $H_2{}^{17}O$, the above equation becomes:

$$\frac{1}{T_{1\rho}(\omega_1)} = \frac{1}{T_{1\rho}^0} + \frac{(35/12)\tau J^2 f}{(1 + \tau^2 \omega_1^2)} \qquad (45)$$

where $J = 2\delta$.

An imaging method that uses $T_{1\rho}$-weighted images to quantify [$H_2{}^{17}O$] based on this theory has been developed (217). Scalar relaxation of the second kind has been demonstrated in the case of amide protons in farmamide (218). Since quadrupolar relaxation and scalar coupling are both independent of the static field, scalar relaxation of either kind is not field-dependent.

In biological tissue, the protons on amide and amine groups are expected to be influenced by the scalar relaxation (second kind) from the quadrupolar nucleus ^{14}N ($I = 1$) and their exchange with bulk water could influence water $T_{1\rho}$ and T_2 relaxation times.

Nonaveraged or residual dipolar coupling. In biological tissues, the presence of nonaveraged RDI can contribute to '$T_{1\rho}$ dispersion'-variation of $T_{1\rho}$ as a function of the spin-locking field. Since the RDI stems from the ordered structures in the tissues, computation of the residual dipolar coupling (RDC) provides information about the structural integrity of tissue. Previously, different types of multiple quantum (MQ) coherence transfer methods have been developed to characterize this interaction. However, due to an order of magnitude low SNR of MQ filtered methods, their applications have been largely limited to *ex vivo* studies and some imaging experiments that were performed on highly ordered tissue such as tendons (86,219). Spin-locking methods to characterize this interaction offer high SNR (comparable to single quantum coherence) and can be implemented *in vivo* with relative ease.

Recently it has been shown that, because of the changing ratio of the residual dipolar coupling to the B_1 of the spin lock pulse, even in the absence of slow motional frequencies, RDI leads to $T_{1\rho}$ dispersion (220).

Theoretical analysis of the $T_{1\rho}$ relaxation, in the presence of RDI, in the simplest model of two chemically

equivalent dipolar coupled nuclear spins under the influence of spin-locking, has been described (221). During spin-locking, the presence of RDI creates anti-phase magnetization, zero and double quantum coherences and longitudinal two spin-order, some of which evolve into observable coherences with different relaxation rates. The signal expression for a dipolar-coupled spins following spin-locking can be written as (221):

$$S(t) = X_1 \exp(-R_{1\rho}^{app}t)$$
$$+ X_2 \exp(-R_{1\rho}^*t)\cos(2\pi\nu_{osc}t + \phi) \quad (46)$$

where

$$X_1 = \frac{(R_{1\rho} - R_{1\rho}^*)^2 + 4\pi^2(\nu_{osc}^2 - \nu_d^2)}{(R_{1\rho}^{app} - R_{1\rho}^*)^2 + 4\pi^2\nu_{osc}^2} \quad (47)$$

and

$$X_1 + X_2\cos\phi = 1 \quad (48)$$

and

$$\tan\phi = \frac{(R_{1\rho} - R_{1\rho}^*) + (R_{1\rho}^* - R_{1\rho}^{app})X_1}{2\pi\nu_{osc}(1 - X_1)} \quad (49)$$

where

$$x_o = -R_{1\rho}^{app} = -R_m$$
$$+ \left\{-q/2 + \left[(q/2)^2 + (p/3)^3\right]^{1/2}\right\}^{1/3} \quad (50)$$
$$+ \left\{-q/2 - \left[(q/2)^2 + (p/3)^3\right]^{1/2}\right\}^{1/3}$$

where

$$p = -\frac{(R_{1\rho}^2 + R_{1\rho}'^2 + R_{1\rho}''^2 - R_{1\rho}R_{1\rho}' - R_{1\rho}R_{1\rho}'' - R_{1\rho}'R_{1\rho}'')}{3}$$
$$+ 4\pi^2\nu_d^2 + 16\pi^2\nu_1^2 \quad (51)$$

and

$$q = (R_{1\rho} + R_{1\rho}' + R_{1\rho}'')$$
$$\times \frac{(2R_{1\rho}^2 + 2R_{1\rho}'^2 + 2R_{1\rho}''^2 - 5R_{1\rho}R_{1\rho}' - 5R_{1\rho}R_{1\rho}'' - 5R_{1\rho}'R_{1\rho}'')}{27}$$
$$+ R_{1\rho}R_{1\rho}'R_{1\rho}'' - \frac{(R_{1\rho} + R_{1\rho}' - 2R_{1\rho}'')4\pi^2\nu_d^2}{3}$$
$$+ \frac{(2R_{1\rho} - R_{1\rho}' - R_{1\rho}'')16\pi^2\nu_1^2}{3} \quad (52)$$

$$x_{1,2} = \frac{-3R_m}{2} - \frac{x_o}{2} \pm 2i\pi\nu_{osc} \quad (53)$$

where

$$\nu_{osc} = \frac{1}{4\pi}\sqrt{4p + 3(x_o + R_m)^2} \quad (54)$$

$R_{1\rho}$ is the relaxation rate of single quantum coherence $(I_x + S_x)$, $R_{1\rho}'$ is the relaxation rate of anti-phase two spin order $(2I_yS_z + 2I_zS_y)$ and $R_{1\rho}''$ is the relaxation rate of $(2I_yS_y - 2I_zS_z)$, which is a mixture of zero, double quantum coherences, $2I_yS_y = (I_+S_- + I_-S_+ - I_+S_+ - I_-S_-)/2$, and longitudinal two-spin order.

$$R_m = \frac{(R_{1\rho} + R_{1\rho}' + R_{1\rho}'')}{3} \quad (55)$$

The following three parameters can be measured from the signal expression:

(1) The damping factor of the slowly decaying part of the evolution curve that yields the apparent rotating frame relaxation rate, $R_{1\rho}^{app}$.
(2) The initial oscillation frequency, ν_{osc}, corresponding to nutation phenomena [due to the presence of two modes: $(2I_yS_y - 2I_zS_z)$ and $(2I_yS_z + 2I_zS_y)$] with respect to the inhomogeneous spin-locking RF field and associated relaxation rate $R_{1\rho}^*$ which, is similar to the R_2^* when one is dealing with precession with respect to an inhomogeneous B_0 field. When spin-locking field is zero, $R_{1\rho}^* \approx R_2^*$.
(3) The relative contributions of the fast and slow decaying components X_1 and X_2.

Limiting cases. *Case 1:* when a small molecule is dissolved into a liquid crystalline solvent, the relaxation rates are expected to be much smaller than ν_1 and ν_d. In this limiting situation:

$$R_{1\rho}^{app} = \frac{4\nu_1^2}{4\nu_1^2 + \nu_d^2}R_{1\rho} + \frac{\nu_d^2}{4\nu_1^2 + \nu_d^2}R_{1\rho}'' \quad (56)$$

and

$$\nu_{osc} = \sqrt{4\nu_1^2 + \nu_d^2} \quad (57)$$

when $\nu_1 \gg \nu_d$, $R_{1\rho}^{app}$ is equal to the true rotating frame relaxation rate, $R_{1\rho}$, whereas for $\nu_1 \ll \nu_d$, $R_{1\rho}^{app}$ tends toward the third-mode relaxation rate, $R_{1\rho}''$.

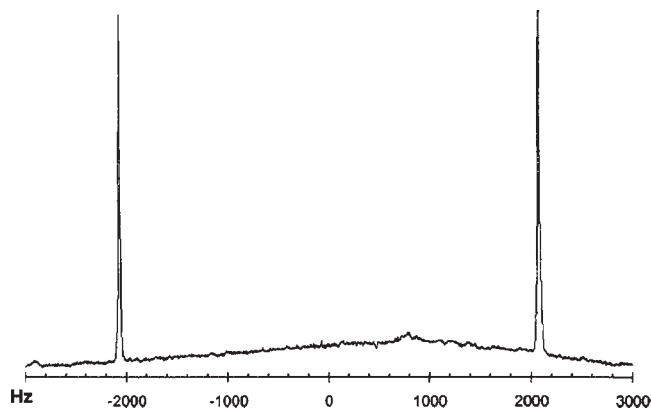$$X_1 = \frac{R_{1\rho}^{*2} + 16\pi^2\nu_1^2}{R_{1\rho}^{*2} + 4\pi^2\nu_{osc}^2} \quad (58)$$

and

$$\tan\phi = \frac{-R_{1\rho}^*}{2\pi\nu_{osc}} \quad (59)$$

Case 2: when $\nu_1 \gg \nu_d$ and both are distributed over a range of values as in any polycrystalline, amorphous solid, or in ordered biological tissues. In this limiting situation:

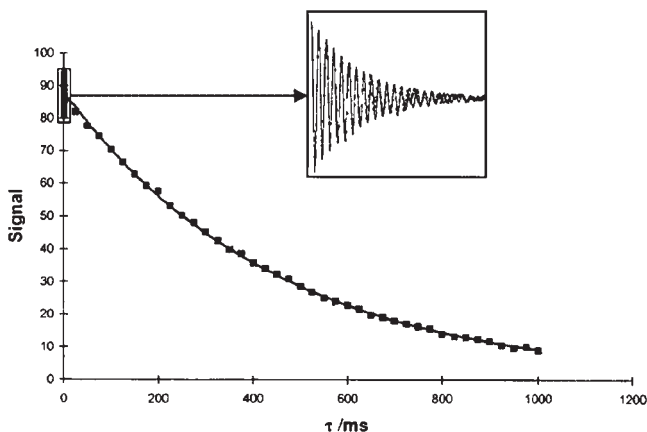$$R_{1\rho}^{app} = R_{1\rho} + \frac{\nu_d^2}{4\nu_1^2}(R_{1\rho}'' - R_{1\rho}) \quad (60)$$

Several experiments have shown the feasibility of measuring the residual dipolar coupling using spin-

Figure 17. Pulse-acquire proton NMR spectrum of CH_2Cl_2 in a nematic solvent (doublet of 4.2 kHz, arising from the dipolar interaction between the two protons). The distorted baseline is due to the broad NMR spectrum of the liquid crystal (221).

locking techniques in a liquid crystal (Figure 17 and Figure 18 spectra and early portion of oscillations). As shown in this example, in single and liquid crystals the dipolar coupling is manifested as resolved resonance splitting in a pulse-acquired spectrum. Hence, spin-locking or other experiments involving complex pulse sequences are not required to measure RDI. However, biological tissues exhibit a distribution of RDI and it may be difficult to resolve the resulting small splitting. Further, due to RF inhomogeneities during spin-locking, the dipolar oscillation frequency will be damped faster and thereby mask the intrinsic relaxation rates. Dominant bulk water, without any RDI, may mask these small and unresolved splittings. In these cases, the spin-locking experiment is well suited to computing the RDI and associated relaxation rates.

Depending upon the limiting case that is applicable for a given tissue, one has to include the appropriate $R_{1\rho}^{app}$ in
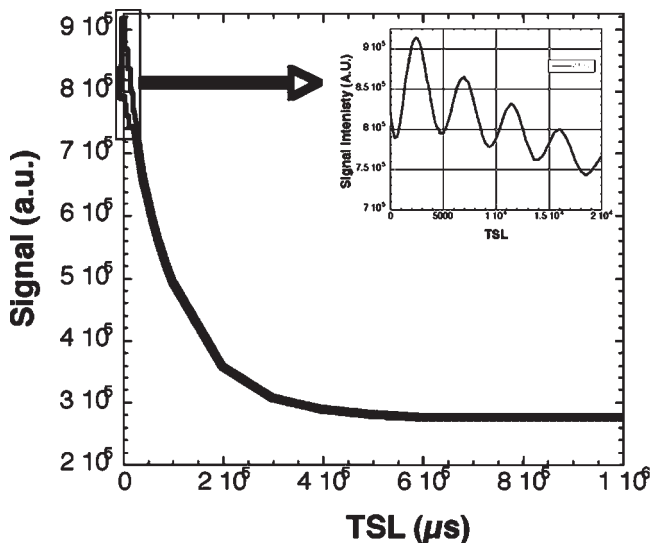
the expression for observed $T_{1\rho}$ in biological tissues. As long as ω_1 is on the order of a few kHz, dipolar relaxation due to molecular rotational processes such as fluctuating dipolar fields and diffusion do not contribute to the $T_{1\rho}$ dispersion but they add as constants to the overall value of $T_{1\rho}$. The T_1 contribution can either be calculated as mentioned above or treated as a constant. The remaining terms are due to the exchange processes that are associated with water protons and other exchangeable protons on macromolecules (such as -OH and -NH), and residual static dipolar coupling. As discussed above, depending upon the tissue type and limiting cases, appropriate contributions due to dominant exchange interaction and static dipolar interaction terms should be included in the total expression for $T_{1\rho}$. Therefore, the observed $T_{1\rho}$ in biological tissues can expressed as:

$$\left[\frac{1}{T_{1\rho}}\right]_{tissue}$$
$$= \left[\frac{1}{T_{1\rho}}\right]_{fD} + \left[\frac{1}{T_{1\rho}}\right]_{Diff} + \left[\frac{1}{T_{1\rho}}\right]_{exchange} + \left[\frac{1}{T_{1\rho}}\right]_{RDI} \quad (61)$$

Dipolar interaction in cartilage

Using the approach described above (221), the existence of dipolar oscillation frequency due to static dipolar interaction and its origin in the case of cartilage and model systems is demonstrated (222).

Figure 19 shows the $T_{1\rho}$-weighted spectral intensity from a native bovine cartilage specimen as a function of spin-lock pulse length (for ω_1 of 200 Hz). The inset shows

Figure 18. Evolution of dipolar doublet as function of the spin-lock period duration; spin-lock amplitude: $w_1 = 4$ kHz. These experimental results were obtained by subtracting the anti-phase doublet signal. Note the initial rapidly damped oscillations and the mono-exponential decay for the major part of the evolution curve (221).

Figure 19. $T_{1\rho}$-weighted signal intensity from a bovine cartilage as a function SL length is shown. The ω_1 used for this study is 250 Hz. The inset shows the expanded version of the initial portion of the signal. The oscillation pattern is characteristic of the presence of RDI in the tissue (240).

the expanded initial portion of the data that has persisting oscillation pattern for $\sim$20 ms. This data, with a fast decaying component with dipolar oscillations and a slow decaying component, has a striking resemblance to the one obtained from liquid crystalline sample with resolved dipolar splitting. This clearly demonstrates the presence of RDI in cartilage. As shown in the inset, in the bovine cartilage the dipolar oscillations lasts $\sim$20 ms during the spin locking. However, since in human cartilage $T_{1\rho}$ relaxation time is about 50% smaller than that in bovine tissue, the oscillation pattern may lasts for about $\sim$10 ms. Since there is a distribution of RDI in cartilage, it should be modeled to fit the observed oscillation pattern to quantify RDI from the tissue similar to the analysis presented by Chaumette *et al.* (221).

Several studies have demonstrated that the static RDI between water molecules associated with fibrillar collagen is the primary source of laminar appearance (alternating bright-dark pattern of signal intensity variation across cartilage) in T_2-weighted images (31,223–225). Given the $\sim$20% (of wet weight) collagen content in cartilage ECM, water proton T_2 relaxation is expected to be dominated by the RDI and therefore masks any small changes in the relaxation times due to alterations in other matrix properties. Further, there are several studies indicating that PG changes in cartilage either do not influence the T_2 or the changes in T_2 do not follow a particular trend (226–228). These observations have led to the argument that T_2 relaxation mapping is either more sensitive to collagen content or only sensitive to changes in collagen (11,228).

$T_{1\rho}$ Dispersion in cartilage

There are only a few studies dealing with $T_{1\rho}$ dispersion in cartilage. In one of the spectroscopic studies of $T_{1\rho}$ dispersion in bovine cartilage, it was suggested that the exchange between protons on -OH and -NH of GAG with bulk water may be the dominant source for the low frequency (0–1.5 kHz) $T_{1\rho}$ dispersion in cartilage (229). Low-frequency dispersion changes are correlated with loss of PG from the ECM of cartilage. Supplementing the experimental data with literature results, logical arguments were presented in support of the mechanism in model systems. However, the data in support of the exchange mechanism in cartilage was extrapolated from that of isolated protein model systems and therefore may not be translated to the case of cartilage with ordered structures. Another problem with this study is that the data was gathered using spectroscopy rather than imaging methods. This will provide an average $T_{1\rho}$ value from the entire sample and could mask subtle regional changes in the tissue characteristics and is highly susceptible to tissue handling (e.g. un-blotted excess water). These experimental and data analysis aspects have to be taken into account when inferring anything from this study.

Recently, $T_{1\rho}$ mapping at two different scanner field strengths was analyzed using a two-site exchange model as described above. It was demonstrated that the $T_{1\rho}$ dispersion is primarily due to RDI and contribution due to chemical exchange between -OH and -NH protons on GAG and bulk water $\leq$3 T is only $\sim$6% (216). Their data also shows that the exchange contribution may increase to $\sim$25% at higher fields of $\sim$7 T. The effect of refocusing the dipolar interaction on the measured T_2 of articular cartilage was also investigated using spectroscopic methods and demonstrated that dipolar interaction contributes significantly to $T_{1\rho}$ dispersion in cartilage. $T_{1\rho}$ dispersion in bovine cartilage and its effect on cartilage contrast, and the effect of spin-locking on the laminar appearance in MRI of cartilage, were also investigated at 4.7 T using orientation-dependent studies (222).

It was found that, when the normal to the surface of cartilage was parallel to B_0, a typical laminar appearance was present in T_2-weighted images but was absent in $T_{1\rho}$-weighted images of the same specimen (Figure 20). At the 'magic angle' orientation (when the surface normal was 54.7° with respect to B_0), neither T_2 nor $T_{1\rho}$ images demonstrated laminae (Figure 21). However, $T_{1\rho}$ values were greater than T_2 at both orientations throughout the cartilage layers. These studies imply that, while RDI contributes to a laminar appearance in T_2 images, its effect is attenuated by spin-locking. Further, if the dipolar interaction is the only contributor to the observed dispersion, then at the magic angle all T_2 values should be equivalent to $T_{1\rho}$ obtained at a spin-lock field at $\sim$2 kHz. They observed significantly higher $T_{1\rho}$ values compared with T_2 even at the magic angle. This may indicate that there are other relaxation mechanisms that contribute to $T_{1\rho}$ in addition to RDI.

Although there are conflicting reports in the literature on the contribution to $T_{1\rho}$ dispersion on cartilage, the bulk of the existing data in the literature and data presented here support the nonaveraged dipolar interaction between water protons associated with collagen being the predominant contributor. However, the dipolar interaction alone cannot account for the complete dispersion observed. Contributions from other sources including exchange cannot be ruled out completely, especially at higher static fields. Further work in this area is required to address this issue.

Small variations in $T_{1\rho}$ dispersion profiles were observed in spectroscopic studies of cartilage specimens (229). However, except for a constant shift, there were no significant changes observed in the $T_{1\rho}$ dispersion curve with varying levels of GAG depletion by trypsin (25). Discrepancy between these results may be due to the measurement of global (spectroscopic) vs (imaging) regional $T_{1\rho}$ and difference in static field strength. In imaging experiments, $T_{1\rho}$ mapping is performed at a particular spin-lock frequency (e.g. 500 Hz) and $T_{1\rho}$ relaxation time, not dispersion, is measured. In spin-locking experiments, as long as the $B_1 > \Delta B_0$, field
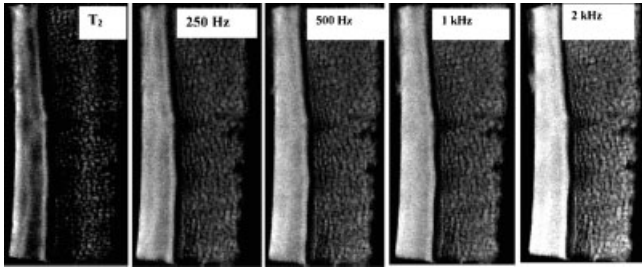
Figure 20. T_2- and $T_{1\rho}$-weighted images of bovine articular cartilage. In T_2-weighted images, laminae of alternating high and low signal intensity pattern are evident. In $T_{1\rho}$-weighted images, the laminar appearance is gradually reduced with increasing ω_1, making the signal more homogeneous across the cartilage (222).

inhomogeneities are refocused. In most of the *in vivo* experiments, this condition is often fulfilled because typical ΔB_0 values are between 100 and 200 Hz and B_1 values used are >250 Hz. At about 500 Hz, (i) reduced dipolar interaction by spin-locking minimizes or eliminates laminae (or relaxation effects due to oriented collagen). At this field, it is likely that scalar-relaxation due to proton exchange between $H_2{}^{17}O$ and $H_2{}^{16}O$ and or between -NH and H_2O may also be attenuated substantially (217). As a consequence of the attenuation of the ΔB_0, RDI and exchange broadening increases the

dynamic range of the $T_{1\rho}$ relaxation time scale by ∼200% in bovine cartilage and by 60% in human cartilage compared with T_2. This improved dynamic range (due to the attenuation of background relaxation of oriented collagen matrix) of $T_{1\rho}$ may facilitate the detection of small changes in relaxation times due to the loss of PG or other matrix component from the tissue. At this point, available data on measured $T_{1\rho}$ in CS phantoms and trypsin-treated cartilage (226) suggest that it may be predominantly due to a combination of changes in [GAG] (221) and, to a lesser extent, from exchange between protons on GAG and bulk water. Further work is required to tease out these contributions. Since the relaxation rate is measured at a fixed B_1 amplitude of the spin-lock pulse, the static dipolar effect adds as a constant. However, $T_{1\rho}$ dispersion maps measured from data obtained as a function of varying B_1 is expected to demonstrate the otherwise dominant dipolar effects and may provide information about the ordered collagen.

Experimental $T_{1\rho}$ studies

***Ex vivo* animal specimens.** Potential of proton $T_{1\rho}$ imaging of cartilage and its applications to study of cartilage degeneration was first proposed by Reddy *et al*. (230). In this study at 2 T, $T_{1\rho}$ mapping and dispersion was
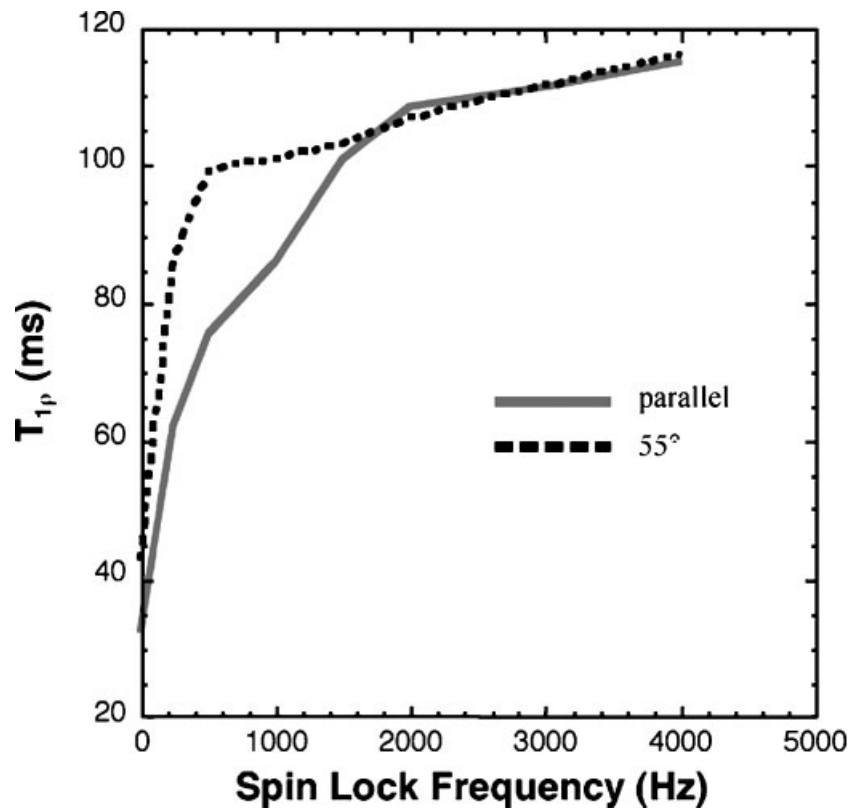
Figure 21. $T_{1\rho}$ dispersion in bovine cartilage; the cartilage surface was oriented parallel to B_0 and at the magic angle ∼55°. The data at spin-lock frequency of zero correspond to the respective T_2 values (222).
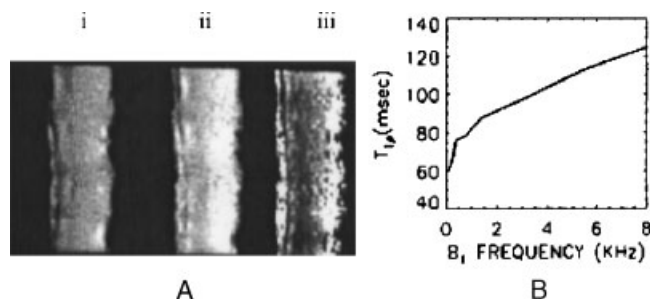
Figure 22. (A) A T_2-weighted (i) and corresponding $T_{1\rho}$-weighted image (ii) and $T_{1\rho}$ map (iii) of a slice through bovine articular cartilage. The $T_{1\rho}$ dispersion collected for spin-lock amplitude (B_1) from 0 to 8 kHz is shown in (B). where a two-fold increase in $T_{1\rho}$ was observed with increasing B_1 amplitude, demonstrating $T_{1\rho}$ dispersion in cartilage (230).

performed on bovine cartilage specimens and the observed dispersion was interpreted by invoking the presence of exchange-modulated dipolar coupling of water protons associated with macromolecules in the tissue (Figure 22). Later studies were performed by subjecting bovine articular cartilage specimens to trypsin- and collagenase-induced PG and collagen degradation, respectively (24). Results demonstrated that the $T_{1\rho}$-weighted images had improved contrast and SNR compared with T_1- and T_2-weighted images and $T_{1\rho}$-weighted images are sensitive to PG change in the tissue. In the same study, it was suggested that collagenase-induced collagen degradation did not exhibit changes in $T_{1\rho}$. However, later it was found that there were errors in the protocol of the collagenase degradation and the conclusions about effect of collagenase on $T_{1\rho}$ were not reliable.

In an elegant study on bovine articular cartilage patellae, sequential trypsin-induced PG depletion was performed (25). Proton $T_{1\rho}$ maps were generated at

varying B_1 fields at 4 T using a home-built RF coil. Depleted PG in the medium was quantified using standard dimethyl methylene blue (DMMB) assay and histology. $T_{1\rho}$ computed from region of interest analysis was found to increase linearly with the amount of PG depleted. $T_{1\rho}$ maps clearly demonstrated the PG depleted regions and corresponded well with the histological analysis performed with Safranin-O staining. In another study at 4 T, $T_{1\rho}$ and T_2 relaxation rates were computed from bovine cartilage subjected to sequential PG depletion (226). $T_{1\rho}$ and T_2 maps were correlated with PG in the tissue (Figure 23) and it was found that there was an excellent correlation ($r^2 = 0.89$) between $1/T_{1\rho}$ and [GAG] while the correlation between $1/T_2$ and [GAG] was rather poor ($r^2 = 0.01$). The $T_{1\rho}$ maps reflected clear changes in PG depleted regions of the tissue (Figure 24). Later on, spectroscopic studies were also demonstrated to have the same trend, although as they are based on global relaxation numbers they underestimate the magnitude of the change in the relaxation rates (231). These studies form the basis for using the $T_{1\rho}$ mapping studies in studying cartilage pathology.

$T_{1\rho}$, T_2 and T_1 studies were also performed on osteoarthritic human specimens obtained following the knee replacement surgery (173). In these studies spin-locking frequency used was ~ 2.5 kHz. It was found that neither T_2 nor $T_{1\rho}$ were significantly changed from studies performed on *ex vivo* human cartilage. These results were in contradiction to the results from several studies described above. The primary reason for this discrepancy appeared to be the status of the osteoarthritic tissue. Prior to the surgery, the patients were intravenously administered GdDTPA^{2-}, a contrast agent known to dominate the relaxation mechanism of water protons. Since the tissues were imaged in the presence of the contrast agent it dominates the relaxation contribution to both $T_{1\rho}$ and T_2
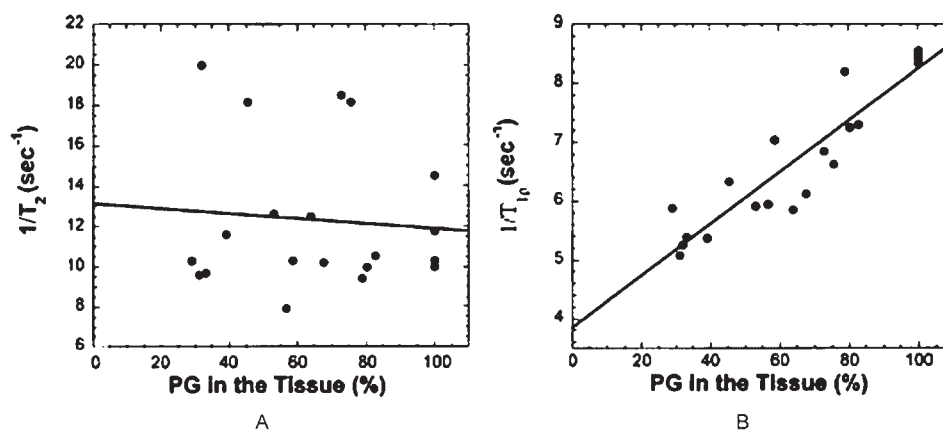
Figure 23. These figures show a plot of $1/T_2$ vs PG and $1/T_{1\rho}$ vs PG loss from a group of bovine cartilage patellae subjected to serial depletion of PG. The solid line indicates the linear fit to the experimental data. Although T_2 did change with PG content, there was no clear trend ($r^2 = 0.01$, $p < 0.7$). $T_{1\rho}$ data from the same set of cartilage specimens, however, demonstrated a strong correlation ($r^2 = 0.9$, $p < 0.001$) between changes in PG and $1/T_{1\rho}$ (226).
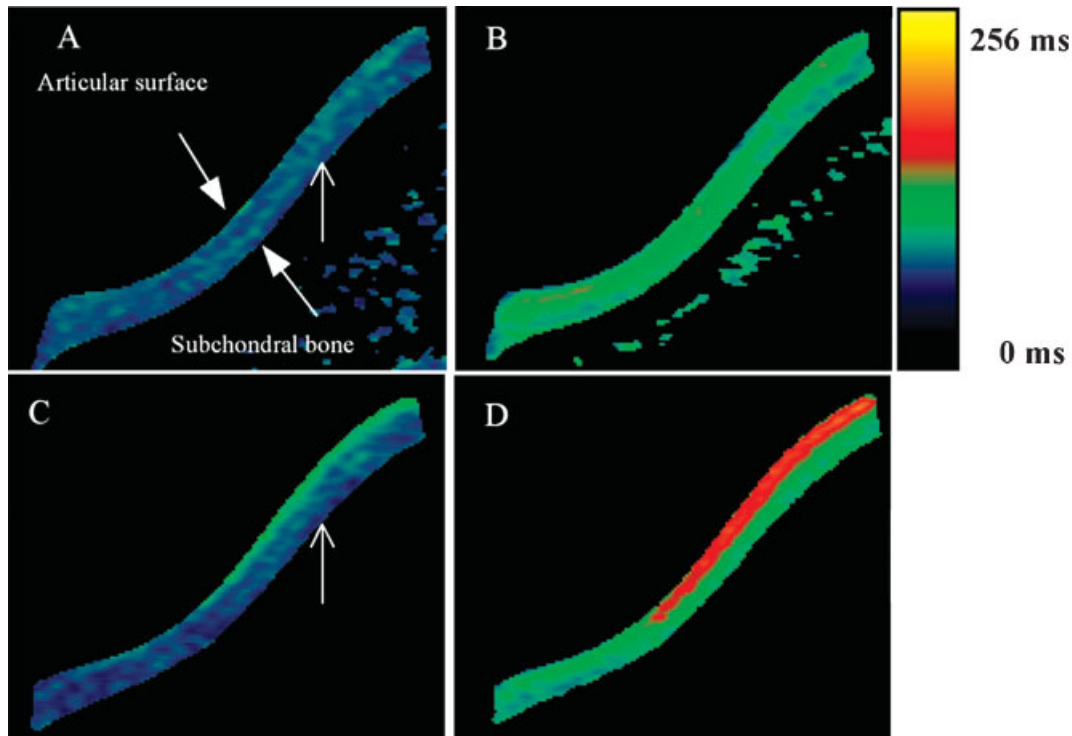
Figure 24. Comparison of T_2, and $T_{1\rho}$ maps of control and 40% of PG depleted bovine patellae. (A) Control T_2 map; (B) control $T_{1\rho}$ map; (C) 40% PG depleted T_2 map; (D) 40% PG depleted $T_{1\rho}$ map. The color scale bar shows the relaxation numbers from 0 to 256 ms (25).

as well and masks any changes due to the loss of PG/ macromolecules from the tissue. These studies clearly demand a thorough investigation of the influence of contrast agents like $GdDTPA^{2-}$ on the magnitude of relaxation contribution to $T_{1\rho}$ and T_2

$T_{1\rho}$ and T_2 measurements were made in collagen and GAG suspensions, and an exponential decrease in $T_{1\rho}$ and T_2 was found with the increasing [collagen] and/or [GAG]. Relaxation time measurements were made in native and trypsin- and interleukin-1β-induced bovine cartilage and some human OA specimens as well (227). In these studies, it was found that $T_{1\rho}$ and T_2 are sensitive to biologically meaningful changes in cartilage. However, they are not specific to any one inherent tissue parameter. In this study, data from phantoms show that both PG and collagen contribute to $T_{1\rho}$ rate ($R_{1\rho}$) in a concentration-dependent manner (at low concentrations, <20%, this is almost linear). However, there are several differences between this study and other $T_{1\rho}$ mapping studies in the literature and the following factors should be taken into account when drawing conclusions from this study:

(1) The experiments were performed at a very high (8.5 T) field strength where other mechanisms, e.g. exchange from -OH and -NH to H_2O, will dominate and could contribute to $T_{1\rho}$ [see above and ref. (173)]. Most other $T_{1\rho}$ studies in the literature were performed between 1.5 and 4 T.

(2) Cartilage samples subjected to IL-1β exhibited decreased T_2 but unchanged $T_{1\rho}$ when compared with healthy and trypsin-treated cartilage. This is completely in conflict with several results from IL-1β studies on a larger group of samples and on an *in vivo* animal model where a significant increases in $T_{1\rho}$ (Figure 25) were observed (54,177).

(3) At the higher field (8.5 T), $T_{1\rho}$ should be lower than that at 1.5 T, but the $T_{1\rho}$ numbers measured in human cartilage in this study are almost 50% higher than those observed at 1.5 T. This result was not explained.

(4) In one of the human specimens, the GAG-depleted region shows 19% elevated $T_{1\rho}$ compared with the healthy-appearing region in the same tissue. In fact, even though a suboptimal color scaling was used and there was a possibility of slice mismatch and associated partial volume effects, the $T_{1\rho}$ map almost mirrors the dGEMRIC map, indicating that there is indeed an elevated $T_{1\rho}$ in regions with lower GAG. At the same time, the observed $T_{1\rho}$ values in two other samples [Fig. 2(C) and (D) with more advanced OA] are not consistent with those observed in the GAG-depleted regions. Given the thin sections of the images (2 mm thick) gathered in two different imaging sessions there is a possibility that the slice mismatching and partial voluming effects may be present in the data.

(5) $T_{1\rho}$ imaging on human specimens was performed in multi-slice mode but there are no details of the
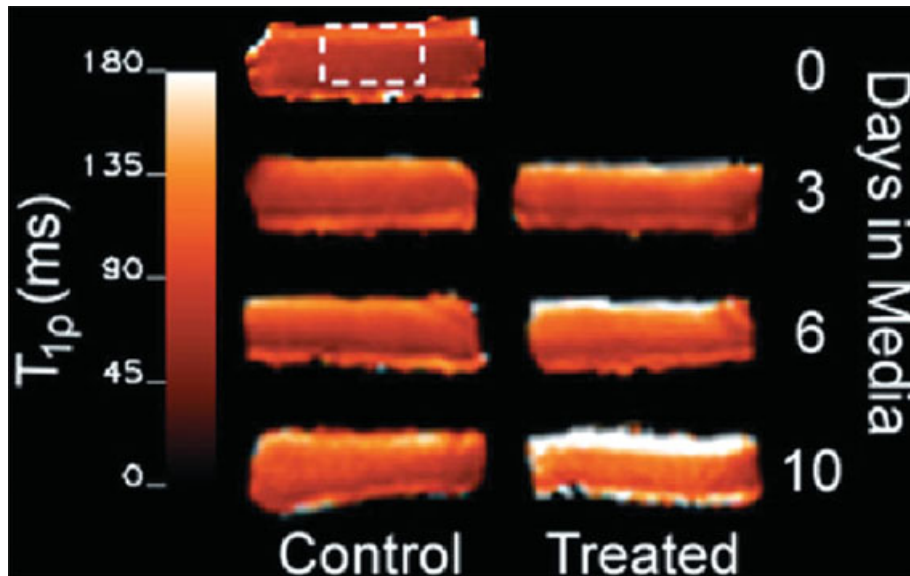
Figure 25. $T_{1\rho}$ maps of representative bovine cartilage specimens in culture media. The treated group represents the treatment with 30 ng/mL of IL-1β over a 10-day period. Significant elevation in $T_{1\rho}$ maps of specimens compared with control specimens is evident (241).

sequence. In fact, in multi-slice mode, there is a substantial $T_{2\rho}$ saturation that, uncorrected, will lead to erroneous results (237).

In direct contradiction to the above study, in human OA specimens ($n = 7$) with different Mankin grades (0–3), a strong correlation between $T_{1\rho}$ rate and FCD measured from sodium MRI was observed (Figure 28), indicating that $T_{1\rho}$ relaxation rate may be useful in studying the OA process in humans (177). Nevertheless, a study on a large group of human osteoarthritic specimens is needed to obtain statistically significant results.

Correlation of changes in cartilage biomechanical and biochemical properties with $T_{1\rho}$ relaxation rate was made in a cytokine-induced model of osteoarthritic condition (54). $T_{1\rho}$ mapping was performed at 4.7 T, and PG, collagen and water content were measured via biochemical assays. Stress-relaxation biomechanical tests were conducted with confined compression apparatus to measure uni-axial aggregate modulus (H_A) and hydraulic permeability (k_0) using linear bi-phasic theory. Results from this study demonstrated that $T_{1\rho}$ relaxation rate was strongly correlated with PG content ($r^2 = 0.93$), H_A ($r^2 = 0.83$) and $\log_{10}k_0$ ($r^2 = 0.86$), demonstrating the potential of $T_{1\rho}$ relaxation as a surrogate index for changes in cartilage biochemical and biomechanical properties as well (Figure 26). These studies clearly provide a link between $T_{1\rho}$ relaxation rate and [GAG] content of the tissue and biomechanical properties. These results are significant because they suggest that non-invasive $T_{1\rho}$ mapping may be used to obtain biomechanical properties of the tissue without subjecting the tissue to compression in magnet, a difficult task to begin with.

Results from this work clearly show the potential of $T_{1\rho}$ relaxation mapping in providing information about biomechanical properties *in vivo*.

***Ex vivo* human specimens.** Studies on isolated chondroitin sulfate and collagen suspensions show that $T_{1\rho}$ is sensitive to both the components of cartilage matrix (227). Owing to a well-ordered structure of collagen and the swelling pressure of PG in intact cartilage, the observed proton $T_{1\rho}$ relaxation rates in the intact cartilage cannot be extrapolated to those obtained from isolated PG and collagen suspensions. Therefore, in order to tease out
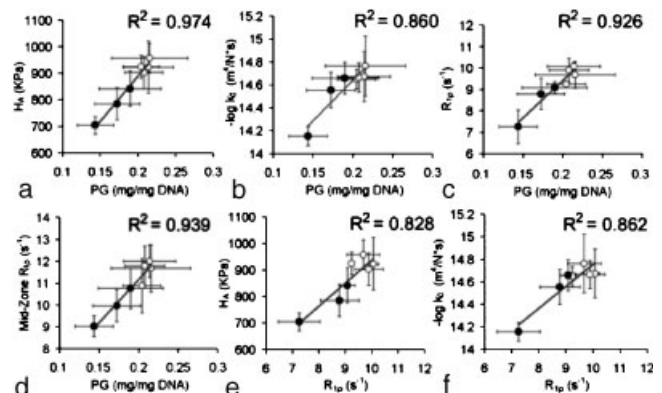
Figure 26. Linear regression plots of average data from each group of (a) H_A vs PG, (b) $\log_{10}k_0$ vs PG, (c) bulk $R_{1\rho}$ vs PG, (d) mid-zone $R_{1\rho}$ vs PG, (e) H_A vs $R_{1\rho}$ and (f) $\log_{10}k_0$ vs $R_{1\rho}$. Open data points represent control groups and closed data points represent IL-1β-treated groups. The correlation coefficient (R^2) is listed on each corresponding plot. Error bars on both axes represent the SD of each measurement (241).
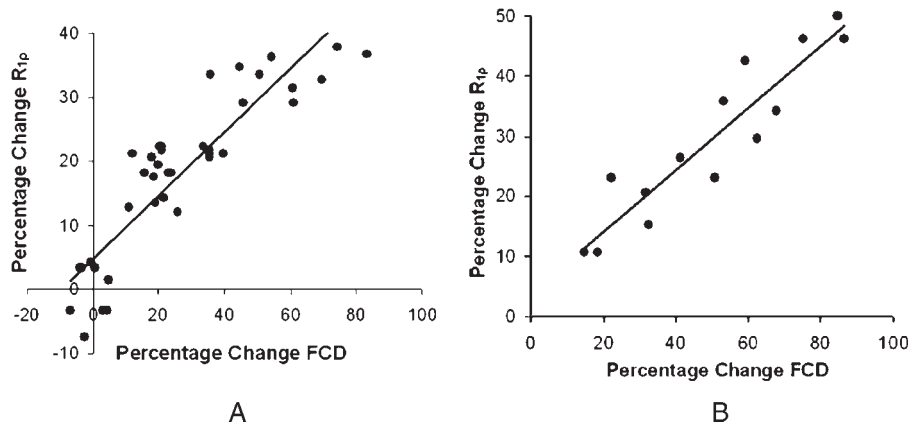
Figure 27. Correlation of normalized FCD and $R_{1\rho}$ data obtained from the trypsin treated model (A). The slope of the linear regression was 0.48 ± 0.004 with $r^2 > 0.75$ ($p < 0.001$). The data are arranged in four clusters representing the four groups of trypsin concentration. The cluster about zero, including negative values, represents the distribution of the mean of the control data. Correlation of normalized FCD and $R_{1\rho}$ data obtained from the natural OA model (B). The slope of the linear regression was 0.51 ± 0.06 with $r^2 > 0.85$ ($p < 0.001$) (177).

the individual contribution of PG and collagen to the observed $T_{1\rho}$, selective depletion studies are needed. It is relatively easy to quantify PG's exclusive contribution to $T_{1\rho}$; however, it is difficult to discern the collagen contribution alone to the $T_{1\rho}$ relaxation. This is because depletion of collagen from cartilage is not feasible without affecting PG content. To overcome this limitation, an indirect approach was used (177) in which spatial maps of proton $T_{1\rho}$ and sodium maps of FCD were computed on bovine specimens subjected to trypsin-induced PG degradation and human OA specimens with different Mankin grade (232). The loss of PG was confirmed by histology in these specimens. Since trypsin predominantly degrades cartilage PG and leaves collagen almost intact, changes induced in $T_{1\rho}$ in this model are primarily from PG loss. In human OA specimens; however, while there may be a predominant contribution from loss of PG, there may also be changes in collagen content and structure depending on the Mankin grade of the tissue. Plots of normalized $1/T_{1\rho}$ rate vs FCD (Figure 27) were found to be strongly correlated with $r^2 > 0.75$ and 0.85, respectively, in both tissue types with nearly identical slope of ~ 0.5 ($p > 0.51$) The strong correlation of the FCD and $T_{1\rho}$ data, with identical slopes, in both the models has interpreted as that the contributions to $T_{1\rho}$ changes are predominantly from PG and any contribution from collagen may be rather small even in natural OA cartilage. A similar trend is shown in the sodium image and $T_{1\rho}$ map of OA specimen (Figure 28).
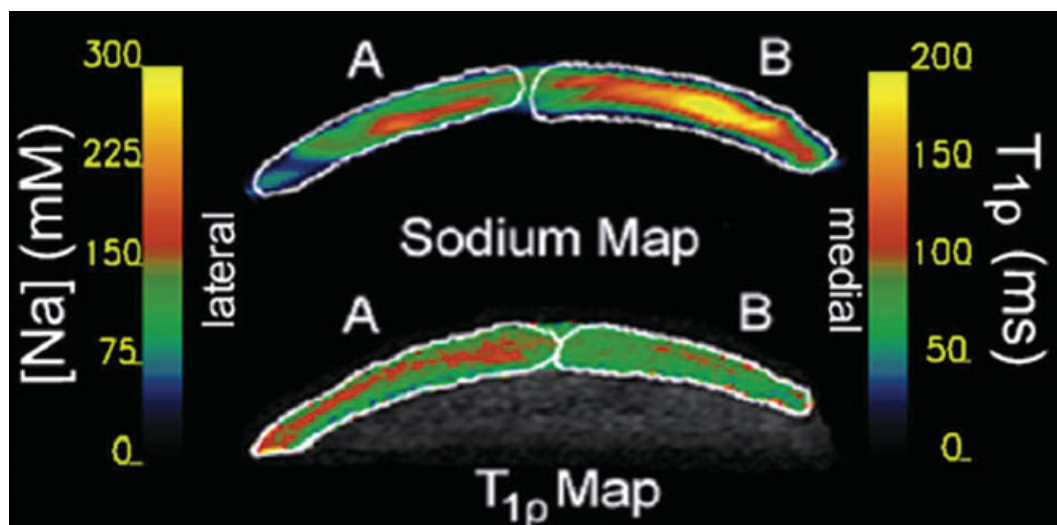

Figure 28. Comparison of sodium concentration and $T_{1\rho}$ maps of a representative *ex vivo* patella from an osteoarthritic joint. The sodium map reveals a distinct reduction in FCD on the lateral side of the patella (ROI A) indicating a reduction of PG content. Elevation of $T_{1\rho}$ in ROI A is observed as an analogous measure of PG loss (177).

Studies on animal models *in vivo*. Animal models serve as a bridge between tissue culture and human disease. The advantage of the animal models is that the disease can be controlled. Therefore, animal models are ideal for research in developing, optimizing and validating therapies, stimulating repair of damaged tissues and understanding the disease process, as well as developing noninvasive diagnostic tools to detect early OA.

The potential of $T_{1\rho}$ mapping in detecting rapidly induced cytokine-mediated cartilage degeneration in porcine animal model *in vivo* was investigated (54). Six Yorkshire pigs were given an intra-articular injection of recombinant porcine interleukin-1β in the knee joints before imaging. The contra-lateral knee joints were given a saline injection to serve as an internal control. Six hours following the injection, $T_{1\rho}$ mapping was performed using $T_{1\rho}$-prepared FSE sequence and sodium imaging was performed using a previously validated method at 4 T. The effect of IL-1β, primarily loss of PG, was confirmed by histological and immunohistochemical analysis (Figure 29). It was found that the average $T_{1\rho}$ rate ($1/T_{1\rho}$) of the IL-1β-treated patella was about 25% lower than that of saline-injected patella. There was an average reduction of 49% in FCD, measured via sodium MRI. These results demonstrate that changes seen in both $T_{1\rho}$ and FCD indicate the loss of PG.

Studies on guinea pig model of spontaneous OA. The advantages of the guinea pig model are that OA occurs spontaneously, it is an inexpensive model compared to anterior cruciate ligament (ACL) transection model, and it has been well studied (233). Initial studies
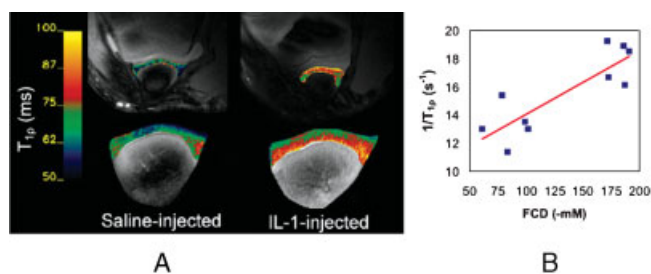
Figure 29. $T_{1\rho}$ maps of saline- and IL-1β-injected patellae of a Yorkshire pig (A) *in vivo* (top row) and the same *ex vivo* (bottom row). Color-coded $T_{1\rho}$ maps corresponding to cartilage are overlaid on the original $T_{1\rho}$-weighted MR image, indicating elevated $T_{1\rho}$ in each IL-1 treated case (54). Also shown is a plot of $1/T_{1\rho}$ measured *in vivo* and FCD measured by post-mortem PG assay from animals (B).

demonstrating the feasibility of performing $T_{1\rho}$ mapping on guinea pig cartilage (Figure 30) exhibited excellent contrast between the cartilage and the surrounding tissues. The in-plane resolution in axial image is $60\,\mu m$ and that in sagittal images is $117\,\mu m$. The signal-to-noise ratio in these images is $\sim25:1$. The color scheme and $T_{1\rho}$ values are shown in the bar-scale. A clear region with elevated $T_{1\rho}$ number (possibly a lesion) can be seen on the femoral cartilage (indicated by an oval shape). In this map, $T_{1\rho}$ numbers of the load-bearing (LB), nonload-bearing (NLB) and lesion regions are: 44 ± 5, 58 ± 5 and 97 ± 14 ms, respectively. The imaging parameters are: spin-lock pulse power $= 500\,Hz$, $TR = 200\,ms$, slice thickness $= 1\,mm$. The spin-lock duration varied from 1 to 40 ms. Average $T_{1\rho}$ relaxation
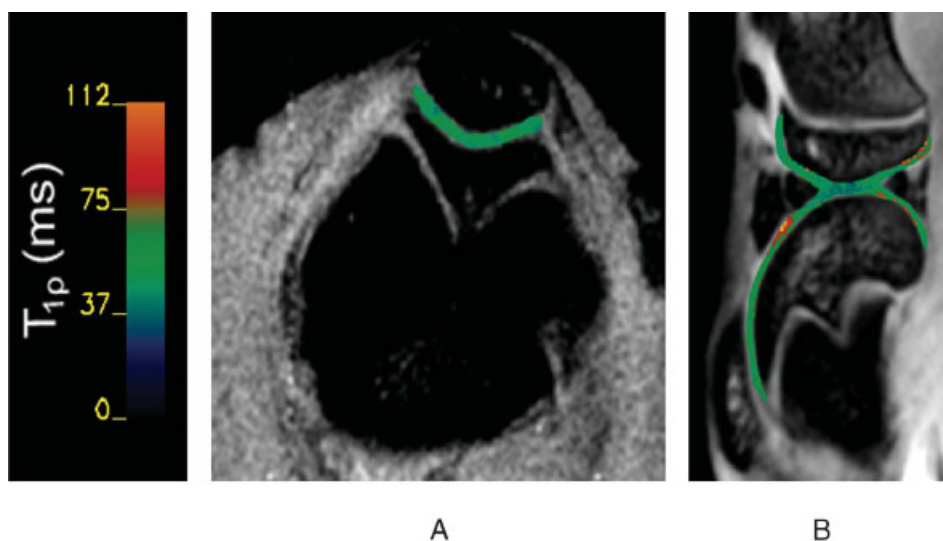
Figure 30. Representative $T_{1\rho}$-weighted images of a guinea pig (age ~4 months) and corresponding color-coded $T_{1\rho}$maps (overlaid on the $T_{1\rho}$-weighted images). (A) An image of the knee joint showing the $T_{1\rho}$ map of patellar cartilage in color. The average $T_{1\rho}$ of patellar cartilage was measured at 57 ± 5 ms. (B) A sagittal slice of the same animal's knee joint showing both femoral and tibial cartilage.

numbers from different regions of guinea pig ($n = 4$) cartilage are as follows: patellar cartilage (59.6 ± 4.4 ms), femoral cartilage load-bearing (43.8 ± 4.6 ms) and femoral cartilage nonload-bearing (65.2 ± 5.4 ms). These results, although preliminary, demonstrate the feasibility of obtaining $T_{1\rho}$ relaxation maps in guinea pig cartilage.

Clinical $T_{1\rho}$ MRI. Proton T_2- and $T_{1\rho}$-weighted images of healthy human knee joint acquired on a 1.5 T clinical scanner with a spin-locking amplitude of 500 Hz are shown in Figure 31. In the T_2-weighted image, the laminar appearance due to different signal intensity patterns corresponding to collagen fiber orientation, although not clearly observed owing to the lack of adequate resolution, is manifested as low signal intensity across the cartilage, whereas in the $T_{1\rho}$-weighted image the laminar appearance is substantially attenuated and results in a more homogeneous appearing and elevated signal intensity across cartilage (222).

Initial $T_{1\rho}$ relaxation studies on healthy human knee joints *in vivo* ($n = 6$) were performed with a $T_{1\rho}$-prepared FSE sequence at 1.5 T (26). Significant $T_{1\rho}$ dispersion (34–50 ms; $T_{1\rho}$ changes with spin-lock frequency) in the frequency range 0–375 Hz was observed. Quantitative comparison of T_2- and $T_{1\rho}$-weighted images has demonstrated a 25% higher signal-difference-to-noise ratio in a chondral lesion, in $T_{1\rho}$-weighted image than in comparable T_2-weighted images *in vivo*.

Clinical $T_{1\rho}$ relaxation mapping studies were also performed in femoral–tibial cartilage and wrist joint *in vivo* at 1.5 T, using home-built bird-cage coils (234,235). In both these studies a single-slice $T_{1\rho}$ prepared FSE sequence was used with a spin locking frequency ranging from 0 to 500 Hz. It was found that the average $T_{1\rho}$ (at $B_1 = 500$ Hz) in the weight-bearing and nonweight-bearing regions of the femoral condyle were 42.2 ± 3.6 and 55.7 ± 2.3 ms, respectively. In wrist joint cartilage, at 500 Hz spin-locking amplitude, $T_{1\rho}$ ranged from 40.5 ± 0.9 to 56.6 ± 4.8 ms. Both studies demonstrated 20–30% higher SNR of cartilage in T_1-weighted images compared with T_2-weighted images. It was suggested that the primary purpose of these studies was to demonstrate the feasibility of quantifying relaxation maps in these complicated structures.

Three-dimensional $T_{1\rho}$ mapping of human knee cartilage was performed at 1.5 T on both healthy and symptomatic osteoarthritic subjects (180,236). Average $T_{1\rho}$ values (at spin locking amplitude of 440 Hz) obtained from eight healthy volunteers (all male with age range 22–45 years) with three-dimensional $T_{1\rho}$ mapping was 49.7 ± 3.2 ms (mean $\pm$ SD) and that obtained from two-dimensional $T_{1\rho}$ mapping was 48.5 ± 2.6 ms (mean $\pm$ SD). In all the symptomatic subjects ($n = 6$, four men and two women, age range 28–63 years) none had radiographic OA except one. $T_{1\rho}$ relaxation times were elevated compared with healthy subjects. In symptomatic subjects, $T_{1\rho}$ values (at 440 Hz spin lock
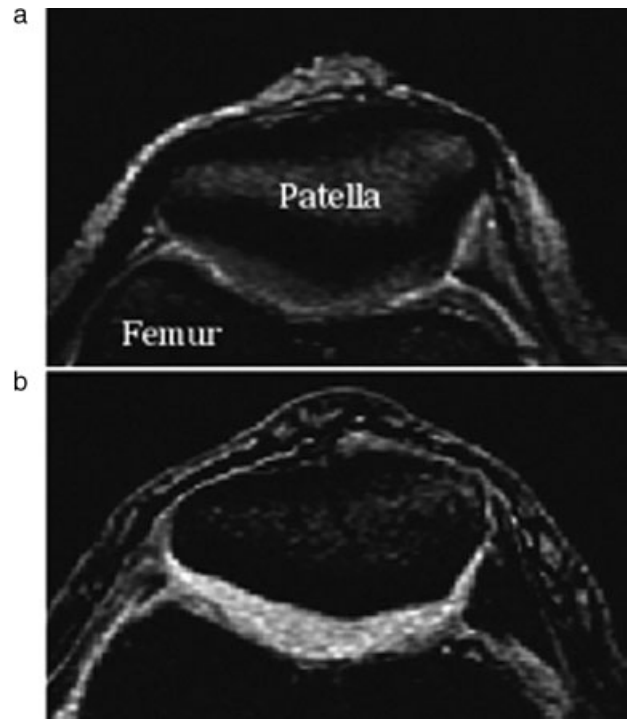

Figure 31. In vivo T_2- and $T_{1\rho}$-weighted images from a healthy human knee joint. The imaging parameters were TR 3 s, FOV $= 10$ cm $\times$ 10 cm, slice thickness $= 3$ mm, matrix $= 256$ 128 (a) T_2-weighted image, TE $= 16$ ms (b) $T_{1\rho}$-weighted image, TE $+$ TSL $= 16$ ms, $B_1 = 500$ Hz.

amplitude) varied from 63 ± 4 to 95 ± 12 ms (mean $\pm$ SD) depending on the degree of cartilage degeneration (Table 4). Although this study was performed on a limited number of subjects, it still demonstrates the potential of $T_{1\rho}$ as a surrogate marker for pre-radiographic OA. Study of a larger group of subjects is required to further evaluate the sensitivity and specificity issue of the method.

$T_{1\rho}$ MRI of osteoarthritic subjects. Figure 32 shows a $T_{1\rho}$-weighted image (in gray-scale) of the knee from a clinically-diagnosed OA subject (38-year-old female). These images were read by a radiologist and confirmed the presence of minor irregularities on cartilage surface. In this $T_{1\rho}$-weighted image, $TSL + TE = 60$ ms and the spin-lock power employed is 500 Hz, with an in-plane resolution of $\sim$390 μm and a 3 mm slice. The lateral side of the $T_{1\rho}$ map (overlaid in color) shows larger region of elevated $T_{1\rho}$ values (indicated with an oval). Although, there is an increase in $T_{1\rho}$ across the cartilage compared with the values from healthy controls, in the elliptical ROI, $T_{1\rho}$ is elevated by $\sim$44% compared with the healthy-appearing region.
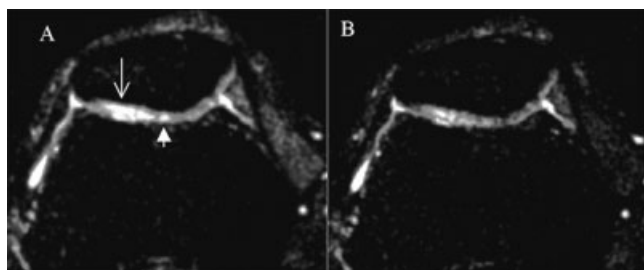
Figure 33 shows $T_{1\rho}$-weighted images from a clinically diagnosed OA patient (40-year-old female) with an absence of cartilage abnormalities on radiographs. A rheumatologist and an orthopedist diagnosed the subject with osteoarthritis and the subject has been on medication
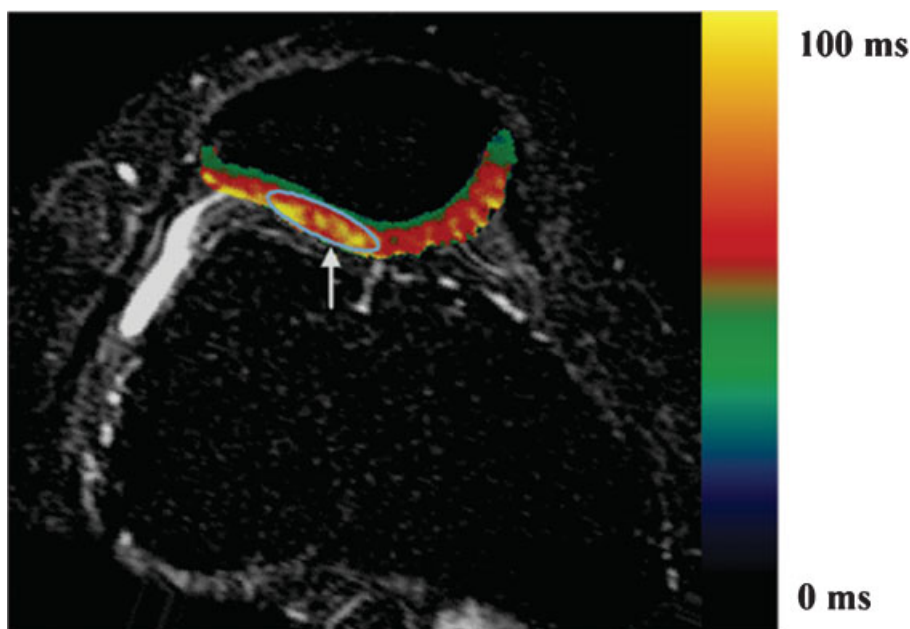
Figure 32. $T_{1\rho}$-weighted image (gray-scale) and corresponding overlaid color map of a clinically diagnosed OA subject's knee joint. This patient *did not* display OA in radiographic images. The region indicated by the oval in the patellar–femoral cartilage indicates a region of elevated $T_{1\rho}$ (>60 ms) and could be a sign of early OA.
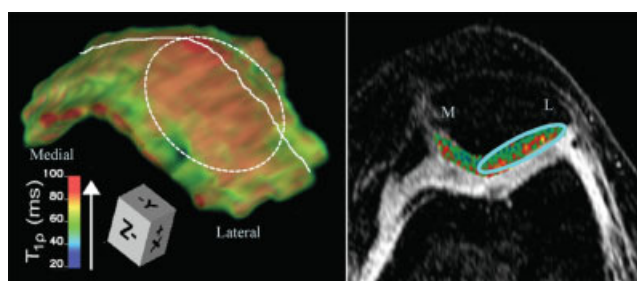
for about one year. A practicing radiologist read these images and diagnosed that the patient has cartilage softening on the lateral side without any surface irregularities. Without the knowledge of imaging sequence used, he found that the $T_{1\rho}$ image had superior contrast and excellent delineation of the lesion. Figure 32 (A) and (B) shows $T_{1\rho}$ images acquired with an effective echo time $(TSL + TE)$ of 45 and 60 ms, respectively. In both $T_{1\rho}$ images, the lateral side of cartilage (indicated by thin arrow) shows elevated signal (in these images, white, yellow and red represent high, medium and low signal intensities, respectively).

$T_{1\rho}$ MRI of a chondromalacia subject. In Figure 34, a three-dimensional surface-rendered $T_{1\rho}$ map and a cross-sectional image of patella of an osteoarthritic human subject who has undergone arthroscopy is

presented. At arthroscopy, grade I chondromalacia was identified on the lateral facet of the patellar cartilage while the medial facet was identified with grade 0. The lateral facet of the $T_{1\rho}$ relaxation map (dashed oval indicates the arthroscopically identified chondromalacia region) clearly shows the elevated $T_{1\rho}$ numbers compared with that of medial facet. Red and yellow voxels in this region indicate substantial increase in the $T_{1\rho}$. These data clearly demonstrate that, in cartilage regions of chondromalacia, $T_{1\rho}$ is increased by $\sim$46% compared with healthy cartilage. The cross sectional image shows the $T_{1\rho}$ map of one of the slices overlaid on the $T_{1\rho}$-weighted

Figure 33. $T_{1\rho}$-weighted images of a symptomatic OA subject without any radiographic OA. (A) and (B) represent the images obtained with an effective weighting of 45 and 60 ms respectively. Elevated signal intensity demonstrates a lesion on cartilage.

Figure 34. Preliminary results from an OA subject arthroscopically diagnosed with grade I chondromalacia in the lateral facet of the patella. The left-hand side figure shows the three-dimensional $T_{1\rho}$ relaxation map of patellar cartilage. The color scale shows a volume-rendered representation of the $T_{1\rho}$ numbers. The image on the right shows a slice of the $T_{1\rho}$ map at the position indicated by a line on the $T_{1\rho}$ surface (on the left) overlaid on the patellar cartilage of the proton density-weighted image. The dashed elliptical region on image on the left is the arthroscopically confirmed region of chondromalacia.
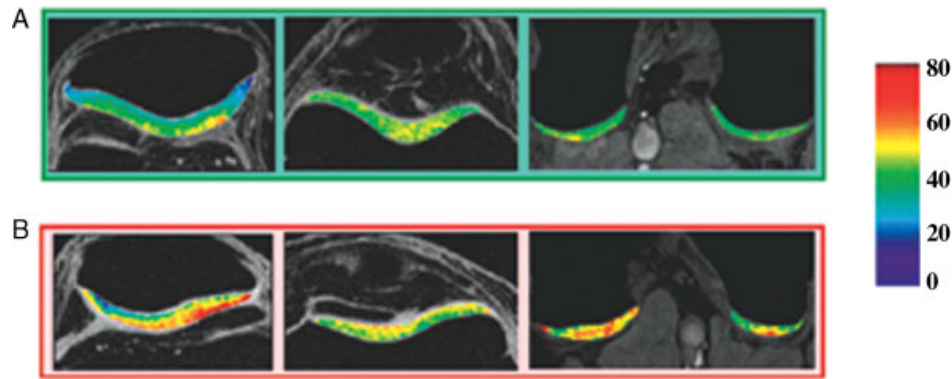
Figure 35. Colour-coded $T_{1\rho}$ maps overlaid on SPGR images. Left: patellar cartilage; middle: anterior femoral (trochlea) cartilage; right: posterior femoral cartilage. (a) a healthy volunteer, male, 30; (b) a patient with early OA, female, 27. The $T_{1\rho}$ values were 40.05 ± 11.43 ms in the volunteer and 50.56 ms ± 19.26 ms in the patient, respectively.

image. In this map, elevated $T_{1\rho}$ across the cartilage depth can be visualized. These results show the feasibility of computing $T_{1\rho}$ maps of grade I chondromalacia of cartilage *in vivo*. Although arthroscopy is a semi-quantitative technique which provides information about cartilage softening, it is a subjective and invasive procedure and not suitable for longitudinal follow-up studies. However, the relaxation maps presented here are quantitative and noninvasive.

A multi-slice spin-lock (MS-SL) pulse sequence was developed and implemented on clinical scanner. Its utility in a clinical setting was demonstrated by measuring $T_{1\rho}$ maps of the knee joints of six healthy human subjects (237). Since MS-SL $T_{1\rho}$ measurements are confounded by the saturation effects due to the $T_{2\rho}$ process, strategies to compensate for these saturation effects are presented. $T_{2\rho}$-compensated $T_{1\rho}$ maps were computed from multi-slice data from human cartilage tissue. These values differed by 5% when compared with the 'gold-standard' single-slice $T_{1\rho}$ values. Although this sequence is superior in SNR and contrast, when compared with three-dimensional FGRE based sequence, it needs a separate $T_{2\rho}$ map or at least a T_2 map of the same section to compensate for $T_{2\rho}$ saturation and compute the actual $T_{1\rho}$ map. Hence its temporal resolution is lower than that of three-dimensional $T_{1\rho}$ mapping sequence.

Another version of a multi-slice $T_{1\rho}$ MRI pulse sequence was developed by integrating the spin-lock preparation with a spiral readout (183,238). Studies were performed on healthy as well as osteoarthritic human patients on a 3 T clinical scanner (Figure 35). $T_{1\rho}$ values obtained with this sequence were validated by comparison with those obtained with a single-slice version of the sequence. In this study, precision of the $T_{1\rho}$ imaging was shown to be $\sim$4.8%. The increase of average $T_{1\rho}$ in cartilage from controls to the patients was 19.1% [43.9 ms for controls ($n = 5$) and 52.3 ms for osteoarthritic patients ($n = 7$; 52 ± 28 ms)], while the increase of was 9.6% for the average T_2 (34.9 ms for controls and 38.3 ms for patients). The difference in average $T_{1\rho}$ in cartilage

between controls and patients was significant ($p = 0.003$), while it was not significant for average T_2 ($p = 0.202$). In this study, although there was significant correlation between $T_{1\rho}$ and T_2, the average $T_{1\rho}$ and T_2 have shown a nonpoint-to-point relationship. This relationship implies that $T_{1\rho}$ and T_2 may give complementary information in detecting cartilage degeneration and injuries. One of the interesting features of this study is that there is a clear demarcation in $T_{1\rho}$ numbers of healthy subjects and OA patients (Figure 36). Results suggest that $T_{1\rho}$ relaxation time may be a promising clinical tool for measuring biochemical changes of the cartilage matrix and treatment monitoring in OA.

Summary

Although early $T_{1\rho}$ experiments on cartilage were spectroscopic, later on these were extended to single-slice imaging and this was followed by the development of three-dimensional and multi-slice imaging methods. Studies on phantoms and isolated matrix components show that both PG and collagen contribute to $T_{1\rho}$. *Ex vivo* studies on bovine specimens subjected to sequential PG depletion have shown a strong correlation between $1/T_{1\rho}$ and [GAG], although correlation between $1/T_2$ and [GAG] was rather poor. *Ex vivo* bovine studies and *in vivo* studies on animal models have shown that treatment with IL-1β elevated the $T_{1\rho}$. In osteoarthritic human specimens, there was a strong correlation between percentage change in FCD measured from sodium MR and percentage change in $1/T_{1\rho}$. The $T_{1\rho}$ rate also strongly correlates with mechanical properties of tissue. However, in studies on a small number of human specimens at 8.5 T, conflicting results were observed. In some specimens elevated $T_{1\rho}$ was observed in GAG-depleted region and in some other specimens it remained almost unchanged. Similarly, in studies (at 8.5 T) on a small group of bovine specimens subjected to IL-1β, $T_{1\rho}$ was found to be unchanged.
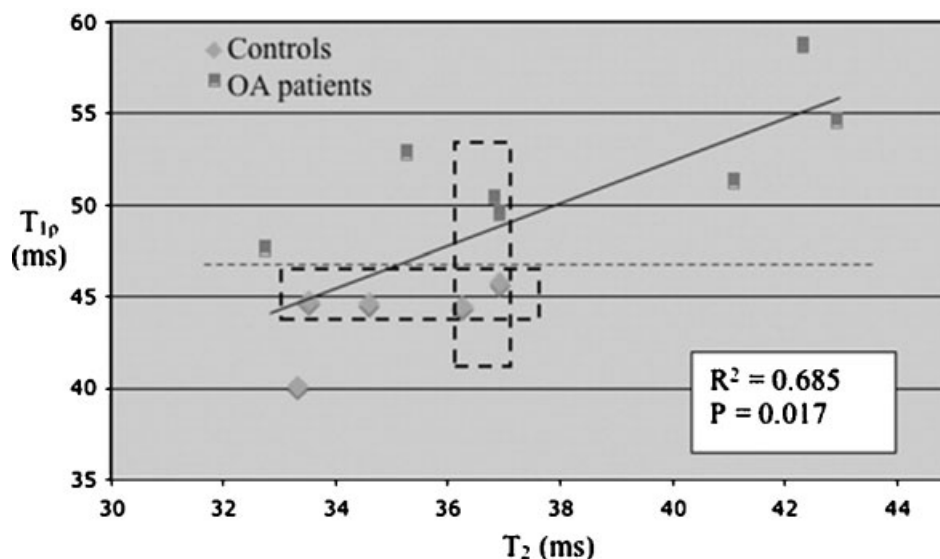
Figure 36. Correlation between $T_{1\rho}$ and T_2 values in 12 subjects (five healthy controls and seven patients with OA). Although the correlation is significant, there is a nonpoint-to-point relationship, that is, patients with similar T_2 values may show different $T_{1\rho}$ values, as shown in the vertical dashed box, or vice versa, as shown in the horizontal dashed box. The dashed line shows a clear-cut difference of the average $T_{1\rho}$ between healthy controls and OA patients, while there is a significant overlap of average T_2 values. A significant difference was found in average $T_{1\rho}$ ($p = 0.003$) but not in T_2 values ($p = 0.2002$) between healthy controls and patients (183).

Existing results to date suggest that contributions to $T_{1\rho}$ dispersion are predominantly due to dipolar interaction of water molecules associated with collagen and they are influenced by the orientation of cartilage. Although the proton exchange between amide and hydroxyl protons on GAG molecules and bulk water may also contribute to the dispersion, its contribution is relatively small at lower fields.

Based on the current data, it appears that the strong correlation between [GAG] and $1/T_{1\rho}$ may be predominantly due to concentration effect in bovine cartilage. The fact that a similar trend is observed in IL-1β-treated specimens, and in human OA specimens, in which some collagen changes are expected, suggests that, in addition to PG contribution, there may be a (small) contribution from collagen as well to the observed $T_{1\rho}$. In other words, $T_{1\rho}$ in addition to measuring PG changes, may also be affected by collagen structural and content changes (if any) present in early OA. Since $T_{1\rho}$ dispersion in cartilage is predominantly due to dipolar interaction of water protons associated with oriented collagen, a dispersion map computed from images obtained as a function of SL pulse amplitude, B_1, at a constant SL length may reflect the changes in collagen structure and content.

When compared with healthy subjects, OA patients presented elevated $T_{1\rho}$ even when their radiographic images did not indicate OA. Measured *in vivo*, $T_{1\rho}$ was found to have a stronger correlation with severity of OA, while differences in T_2 were not statistically significant. $T_{1\rho}$ was also elevated in a patient with arthroscopically confirmed grade I chondromalacia but without radiographic OA. These results clearly indicate that $T_{1\rho}$ may

serve as a surrogate marker for molecular changes (pre-radiographic) in cartilage and may be useful in longitudinal studies. So far the $T_{1\rho}$ studies have been mostly 'demonstration of feasibility' in nature, involving a very limited number of healthy and OA subjects. $T_{1\rho}$ studies on a large group of OA specimens with varying degree of degeneration are needed to determine the correlation between $T_{1\rho}$ rate and OA disease severity as determined by histopathology. Similarly, studies on a large group of OA subjects with mild to moderate OA (with a different degree of radiographic OA) and age-matched healthy subjects are needed to address the issues regarding the precision of $T_{1\rho}$ measurement, the effect of age and disease severity on these measurements and the capability to longitudinally measure OA disease progression.

Acknowledgments

REFERENCES

1. Felson DT. Epidemiology of hip and knee osteoarthritis. *Epidemiol. Prev.* 1988; **10**: 1–28.
2. Felson DT. The incidence and natural history of knee osteoarthritis in the elderly. The Farmingham Osteoarthritis Study. *Arthritis Rheum.* 1995; **38**: 1500–1505.

3. Guccione AA, Felson DT, Anderson JJ, Anthony JM, Zhang Y, Wilson PW, Kelly-Hayes M, Wolf PA, Kreger BE, Kamel WB. The effects of specific medical conditions on the functional limitations of elders in the Farmingham Study. *Am. J. Public Health* 1994; **84**: 351–358.

4. Yelin E. The economics of osteoarthritis. In *Osteoarthritis*, Brandt K, Doherty M, Lohmander LS (eds). Oxford Medical: Oxford, 1998; 23–30.

5. Stanton H, Rogerson FM, East CJ, Golub SB, Lawlor KE, Meeker CT, Little CB, Last K, Farmer PJ, Campbell IK, Fourie AM, Fosang AJ. ADAMTS5 is the major aggrecanase in mouse cartilage *in vivo* and *in vitro*. *Nature* 2005; **434**(7033): 648–652.

6. Glasson SS, Askew R, Sheppard B, Carito B, Blanchet T, Ma HL, Flannery CR, Peluso D, Kanki K, Yang Z, Majumdar MK, Morris EA. Deletion of active ADAMTS5 prevents cartilage degradation in a murine model of osteoarthritis. *Nature* 2005; **434**(7033): 644–648.

7. Smith HE, Mosher TJ, Dardzinski BJ, Collins BG, Collins CM, Yang QX, Schmithorst VJ, Smith MB. Spatial variation in cartilage T_2 of the knee. *J. Magn. Reson. Imag.* 2001; **14**(1): 50–55.

8. Dardzinski BJ, Mosher TJ, Li SZ, VanSlyke MA, Smith MB. Spatial variation of T_2 in human articular cartilage. *Radiology* 1997; **205**(2): 546–550.

9. David-Vaudey E, Ghosh S, Ries M, Majumdar S. T_2 relaxation time measurements in osteoarthritis. *Magn. Reson. Imag.* 2004; **22**(5): 673–682.

10. Glaser C. New techniques for cartilage imaging: T_2 relaxation time and diffusion-weighted MR imaging. *Radiol. Clin. N. Am.* 2005; **43**(4): 641–653, vii.

11. Mosher TJ, Smith H, Dardzinski BJ, Schmithorst VJ, Smith MB. MR imaging and T_2 mapping of femoral cartilage: *in vivo* determination of the magic angle effect. *AJR Am. J. Roentgenol.* 2001; **177**(3): 665–669.

12. Mosher TJ, Dardzinski BJ. Cartilage MRI T_2 relaxation time mapping: overview and applications. *Semin. Musculoskelet. Radiol.* 2004; **8**(4): 355–368.

13. Mosher TJ, Smith HE, Collins C, Liu Y, Hancy J, Dardzinski BJ, Smith MB. Change in knee cartilage T_2 at MR imaging after running: a feasibility study. *Radiology* 2005; **234**(1): 245–249.

14. Van Breuseghem I. Ultrastructural MR imaging techniques of the knee articular cartilage: problems for routine clinical application. *Eur. Radiol.* 2004; **14**(2): 184–192.

15. Van Breuseghem I, Bosmans HT, Elst LV, Maes F, Pans SD, Brys PP, Geusens EA, Marchal GJ. T_2 mapping of human femorotibial cartilage with turbo mixed MR imaging at 1.5 T: feasibility. *Radiology* 2004; **233**(2): 609–614.

16. Van Breuseghem I, Palmieri F, Peeters RR, Maes F, Bosmans HT, Marchal GJ. Combined T_1–T_2 mapping of human femoro-tibial cartilage with turbo-mixed imaging at 1.5 T. *J. Magn. Reson. Imag.* 2005; **22**(3): 368–372.

17. Dunn TC, Lu Y, Jin H, Ries MD, Majumdar S. T_2 relaxation time of cartilage at MR imaging: comparison with severity of knee osteoarthritis. *Radiology* 2004; **232**(2): 592–598.

18. Nieminen MT, Rieppo J, Toyras J, Hakumaki JM, Silvennoinen J, Hyttinen MM, Helminen HJ, Jurvelin JS. T_2 relaxation reveals spatial collagen architecture in articular cartilage: a comparative quantitative MRI and polarized light microscopic study. *Magn. Reson. Med.* 2001; **46**(3): 487–493.

19. Nieminen MT, Menezes NM, Williams A, Burstein D. T_2 of articular cartilage in the presence of Gd-DTPA2. *Magn. Reson. Med.* 2004; **51**(6): 1147–1152.

20. Watrin-Pinzano A, Ruaud JP, Olivier P, Grossin L, Gonord P, Blum A, Netter P, Guillot G, Gillet P, Loeuille D. Effect of proteoglycan depletion on T_2 mapping in rat patellar cartilage. *Radiology* 2005; **234**(1): 162–170.

21. Bashir A, Gray ML, Burstein D. Gd-DTPA^{2-} as a measure of cartilage degradation. *Magn. Reson. Med.* 1996; **36**: 665–673.

22. Bashir A, Gray ML, Boutin RD, Burstein D. Glycosaminoglycan in articular cartilage: *in vivo* assessment with delayed Gd(DTPA)$^{2-}$-enhanced MR imaging. *Radiology* 1997; **205**(2): 551–558.

23. Reddy R, Insko EK, Kaufman JH, Bolinger L, Kneeland JB, Leigh JS. MR imaging of cartilage under spin-locking. In *Proceedings of International Society of Magnetic Resonance Medicine*, Nice, 1995; 1535.

24. Duvvuri U, Reddy R, Patel SD, Kaufman JH, Kneeland JB, Leigh JS. $T_{1\rho}$-relaxation in articular cartilage: effects of enzymatic degradation. *Magn. Reson. Med.* 1997; **38**(6): 863–867.

25. Akella SV, Reddy Regatte R, Gougoutas AJ, Borthakur A, Shapiro EM, Kneeland JB, Leigh JS, Reddy R. Proteoglycan-induced changes in $T_{1\rho}$-relaxation of articular cartilage at 4 T. *Magn. Reson. Med.* 2001; **46**(3): 419–423.

26. Duvvuri U, Charagundla SR, Kudchodkar SB, Kaufman JH, Kneeland JB, Rizi R, Leigh JS, Reddy R. Human knee: *in vivo* $T_1(_\rho)$-weighted MR imaging at 1.5 T—preliminary experience. *Radiology* 2001; **220**(3): 822–826.

27. Reddy R, Insko EK, Noyszewski EA, Dandora R, Kneeland JB, Leigh JS. Sodium MRI of human articular cartilage *in vivo*. *Magn. Reson. Med.* 1998; **39**(5): 697–701.

28. Borthakur A, Shapiro EM, Beers J, Kudchodkar S, Kneeland JB, Reddy R. Sensitivity of MRI to proteoglycan depletion in cartilage: comparison of sodium and proton MRI. *Osteoarthritis Cartilage* 2000; **8**(4): 288–293.

29. Shapiro EM, Borthakur A, Dandora R, Kriss A, Leigh JS, Reddy R. Sodium visibility and quantitation in intact bovine articular cartilage using high field ^{23}Na MRI and MRS. *J. Magn. Reson.* 2000; **142**(1): 24–31.

30. Wheaton AJ, Borthakur A, Shapiro EM, Regatte RR, Akella SV, Kneeland JB, Reddy R. Proteoglycan Loss in Human Knee Cartilage: Quantitation with Sodium MR Imaging—Feasibility Study. *Radiology* 2004; **231**(3): 900–905.

31. Goodwin DW, Dunn JF. MR imaging and T_2 mapping of femoral cartilage. *AJR Am. J. Roentgenol.* 2002; **178**(6): 1568–1569; author reply 1569–1570.

32. Burstein D, Gray M. New MRI techniques for imaging cartilage. *J. Bone Joint Surg. Am.* 2003; **85**(A Suppl. 2): 70–77.

33. Gray ML, Burstein D. Molecular (and functional) imaging of articular cartilage. *J. Musculoskelet. Neuronal Interact.* 2004; **4**(4): 365–368.

34. Gray ML, Eckstein F, Peterfy C, Dahlberg L, Kim YJ, Sorensen AG. Toward imaging biomarkers for osteoarthritis. *Clin. Orthoped. Relat. Res.* 2004 (427 Suppl): S175–181.

35. Gatehouse PD, Thomas RW, Robson MD, Hamilton G, Herlihy AH, Bydder GM. Magnetic resonance imaging of the knee with ultrashort *TE* pulse sequences. *Magn. Reson. Imag.* 2004; **22**(8): 1061–1067.

36. Gold GE, McCauley TR, Gray ML, Disler DG. What's new in cartilage? *Radiographics* 2003; **23**(5): 1227–1242.

37. Gold GE, Reeder SB, Beaulieu CF. Advanced MR imaging of the shoulder: dedicated cartilage techniques. *Magn. Reson. Imag. Clin. N. Am.* 2004; **12**(1): 143–159, vii.

38. Gold GE, Hargreaves BA, Reeder SB, Vasanawala SS, Beaulieu CF. Controversies in protocol selection in the imaging of articular cartilage. *Semin. Musculoskelet. Radiol.* 2005; **9**(2): 161–172.

39. Hall BK, Newman S. *Cartilage: Molecular Aspects*. CRC Press: Boca Raton, FL, 1991.

40. Recht MP, Goodwin DW, Winalski CS, White LM. MRI of articular cartilage: revisiting current status and future directions. *AJR Am. J. Roentgenol.* 2005; **185**(4): 899–914.

41. Peterfy CG. Imaging of the disease process. *Curr. Opin. Rheumatol.* 2002; **14**(5): 590–596.

42. Young IR, Bydder GM. Magnetic resonance: new approaches to imaging of the musculoskeletal system. *Physiol. Msmt* 2003; **24**(4): R1–23.

43. Winalski CS, Gupta KB. Magnetic resonance imaging of focal articular cartilage lesions. *Top. Magn. Reson. Imag.* 2003; **14**(2): 131–144.

44. Makin HJ, Mow VC, Buckwalter JA. Form and function of articular cartilage. In *Orthopedic Basic Sciences*, Simon SR (ed.). American Academy of Orthopedic Surgeons: Philadelphia, PA, 1994; 3–44.

45. Harris ED, Ruddy S, Kelley WN. *Kelley's Textbook of Rheumatology*. Elsevier/Saunders: Philadelphia, PA, 2005.

46. Pritzker KP, Gay S, Jimenez SA, Ostergaard K, Pelletier JP, Revell PA, Salter D, van den Berg WB. Osteoarthritis cartilage histopathology: grading and staging. *Osteoarthritis Cartilage* 2006; **14**(1): 13–29.

47. Fernandez-Madrid F, Karvonen RL, Teitge RA, Miller PR, Negendank WG. MR features of osteoarthritis of the knee. *Magn. Reson. Imag.* 1994; **12**(5): 703–709.

48. Bonnet CS, Walsh DA. Osteoarthritis, angiogenesis and inflammation. *Rheumatology (Oxford)* 2005; **44**(1): 7–16.

49. Smith RJ, Rohloff NA, Sam LM, Justen JM, Deibel MR, Cornette JC. Recombinant human interleukin–1 alpha and recombinant human interleukin-1 beta stimulate cartilage matrix degradation and inhibit glycosaminoglycan synthesis. *Inflammation* 1989; **13**(4): 367–382.

50. McGuire-Goldring MB, Meats JE, Wood DD, Ihrie EJ, Ebsworth NM, Russell RG. *In vitro* activation of human chondrocytes and synoviocytes by a human interleukin-1-like factor. *Arthritis Rheum.* 1984; **27**(6): 654–662.

51. Meulenbelt I, Seymour AB, Nieuwland M, Huizinga TW, van Duijn CM, Slagboom PE. Association of the interleukin-1 gene cluster with radiographic signs of osteoarthritis of the hip. *Arthritis Rheum.* 2004; **50**(4): 1179–1186.

52. Leppavuori J, Kujala U, Kinnunen J, Kaprio J, Nissila M, Heliovaara M, Klinger N, Partanen J, Terwilliger JD, Peltonen L. Genome scan for predisposing loci for distal interphalangeal joint osteoarthritis: evidence for a locus on 2q. *Am. J. Hum. Genet.* 1999; **65**(4): 1060–1067.

53. Forster T, Chapman K, Marcelline L, Mustafa Z, Southam L, Loughlin J. Finer linkage mapping of primary osteoarthritis susceptibility loci on chromosomes 4 and 16 in families with affected women. *Arthritis Rheum.* 2004; **50**(1): 98–102.

54. Wheaton AJ, Dodge GR, Borthakur A, Kneeland JB, Schumacher HR, Reddy R. Detection of changes in articular cartilage proteoglycan by $T(1rho)$ magnetic resonance imaging. *J. Orthoped. Res.* 2005; **23**(1): 102–108.

55. Dinarello CA. The IL-1 family and inflammatory diseases. *Clin. Exp. Rheumatol.* 2002; **20**(5 Suppl. 27): S1–13.

56. Mosley B, Urdal DL, Prickett KS, Larsen A, Cosman D, Conlon PJ, Gillis S, Dower SK. The interleukin-1 receptor binds the human interleukin-1 alpha precursor but not the interleukin-1 beta precursor. *J. Biol. Chem.* 1987; **262**(7): 2941–2944.

57. Lo YY, Conquer JA, Grinstein S, Cruz TF. Interleukin-1 beta induction of c-fos and collagenase expression in articular chondrocytes: involvement of reactive oxygen species. *J. Cell Biochem.* 1998; **69**(1): 19–29.

58. Nietfeld JJ, Wilbrink B, Den Otter W, Huber J, Huber-Bruning O. The effect of human interleukin 1 on proteoglycan metabolism in human and porcine cartilage explants. *J. Rheumatol.* 1990; **17**(6): 818–826.

59. Ku G, Faust T, Lauffer LL, Livingston DJ, Harding MW. Interleukin-1 beta converting enzyme inhibition blocks progression of type II collagen-induced arthritis in mice. *Cytokine* 1996; **8**(5): 377–386.

60. Koshy PJ, Lundy CJ, Rowan AD, Porter S, Edwards DR, Hogan A, Clark IM, Cawston TE. The modulation of matrix metalloproteinase and ADAM gene expression in human chondrocytes by interleukin-1 and oncostatin M: a time-course study using real-time quantitative reverse transcription-polymerase chain reaction. *Arthritis Rheum.* 2002; **46**(4): 961–967.

61. Primakoff P, Myles DG. The ADAM gene family: surface proteins with adhesion and protease activity. *Trends Genet.* 2000; **16**(2): 83–87.

62. Tortorella MD, Burn TC, Pratta MA, Abbaszade I, Hollis JM, Liu R, Rosenfeld SA, Copeland RA, Decicco CP, Wynn R, Rockwell A, Yang F, Duke JL, Solomon K, George H, Bruckner R, Nagase H, Itoh Y, Ellis DM, Ross H, Wiswall BH, Murphy K, Hillman MC Jr, Hollis GF, Newton RC, Magolda RL, Trzaskos JM, Arner EC. Purification and cloning of aggrecanase-1: a member of the ADAMTS family of proteins. *Science* 1999; **284**(5420): 1664–1666.

63. Abbaszade I, Liu RQ, Yang F, Rosenfeld SA, Ross OH, Link JR, Ellis DM, Tortorella MD, Pratta MA, Hollis JM, Wynn R, Duke JL, George HJ, Hillman MC, Jr. Murphy K, Wiswall BH, Copeland RA, Decicco CP, Bruckner R, Nagase H, Itoh Y, Newton RC, Magolda RL, Trzaskos JM, Burn TC. Cloning and characterization of ADAMTS11, an aggrecanase from the ADAMTS family. *J. Biol. Chem.* 1999; **274**(33): 23443–23450.

64. Sandy JD, Neame PJ, Boynton RE, Flannery CR. Catabolism of aggrecan in cartilage explants. Identification of a major cleavage site within the interglobular domain. *J. Biol. Chem.* 1991; **266**(14): 8683–8685.

65. Sandy JD, Flannery CR, Neame PJ, Lohmander LS. The structure of aggrecan fragments in human synovial fluid. Evidence for the involvement in osteoarthritis of a novel proteinase which cleaves the Glu 373–Ala 374 bond of the interglobular domain. *J. Clin. Invest.* 1992; **89**(5): 1512–1516.

66. Bartholomew JS, Handley CJ, Lowther DA. The effects of trypsin treatment on proteoglycan biosynthesis by bovine articular cartilage. *Biochem. J.* 1985; **227**(2): 429–437.

67. Berg A, Singer T, Moser E. High-resolution diffusivity imaging at 3.0 T for the detection of degenerative changes: a trypsin-based arthritis model. *Invest. Radiol.* 2003; **38**(7): 460–466.

68. Malemud CJ, Shuckett R, Goldberg VM. Changes in proteoglycans of human osteoarthritic cartilage maintained in explant culture: implications for understanding repair in osteoarthritis. *Scand. J. Rheumatol. Suppl.* 1988; **77**: 7–12.

69. Gaboriaud C, Serre L, Guy-Crotte O, Forest E, Fontecilla-Camps JC. Crystal structure of human trypsin 1: unexpected phosphorylation of Tyr151. *J. Mol. Biol.* 1996; **259**(5): 995–1010.

70. Basser PJ, Schneiderman R, Bank RA, Wachtel E, Maroudas A. Mechanical properties of the collagen network in human articular cartilage as measured by osmotic stress technique. *Arch. Biochem. Biophys.* 1998; **351**(2): 207–219.

71. Xia Y, Farquhar T, Burtonwurster N, Verniersinger M, Lust G, Jelinski LW. Self-diffusion monitors degraded cartilage. *Arch. Biochem. Biophys.* 1995; **323**(2): 323–328.

72. Duda GN, Kleemann RU, Bluecher U, Weiler A. A new device to detect early cartilage degeneration. *Am. J. Sports Med.* 2004; **32**(3): 693–698.

73. Yoshioka H, Haishi T, Uematsu T, Matsuda Y, Itai Y, Kose K. MR microscopy of the articular cartilage with a 1.0 T permanent magnet portable MR system: preliminary results. *Magn. Reson. Med. Sci.* 2003; **2**(1): 51–55.

74. Abragam A. *The Principles of Nuclear Magnetism.* Clarendon Press: Oxford, 1961.

75. Slichter CP. *Principles of Magnetic Resonance.* Springer: Berlin, 1996.

76. Das TP, Hahn EL. *Nuclear Quadrupole Resonance Spectroscopy.* Academic Press: New York, 1958.

77. Haeberlen U. *High Resolution NMR in Solids: Selective Averaging*, Waugh JH (ed.). Academic Press: London, 1976.

78. Jerschow A. From nuclear structure to the quadrupolar NMR interaction and high-resolution spectroscopy. *Prog. Nucl. Magn. Reson. Spectrosc.* 2005; **46**(1): 63.

79. Mehring M. *High Resolution NMR in Solids.* Springer: Berlin, 1976.

80. Ashbrook SE, Wimperis S. High-resolution NMR of quadrupolar nuclei in solids: the satellite-transition magic angle spinning (STMAS) experiment. *Prog. Nucl. Magn. Reson. Spectrosc.* 2004; **45**(1–2): 53.

81. Donald EW. NMR relaxation of spin-3/2 nuclei: effects of structure, order, and dynamics in aqueous heterogeneous systems. *Conc. Magn. Reson.* 2001; **13**(5): 294–325.

82. Jaccard G, Wimperis S, Bodenhausen G. Multiple quantum NMR spectroscopy of $S = 3/2$ spins in isotropic phase: a new probe for multiexponential relaxation. *J. Chem. Phys.* 1986; **85**(11): 6282–6293.

83. Johan RCvdM. Thermal relaxation and coherence dynamics of spin 3/2. I. Static and fluctuating quadrupolar interactions in the multipole basis. *Conc. Magn. Reson. Pt A* 2003; **19A**(2): 97–116.

84. Johan RCvdM. Thermal relaxation and coherence dynamics of spin 3/2. II. Strong radio-frequency field. *Conc. Magn. Reson. Pt A* 2003; **19A**(2): 117–133.

85. Kemp-Harper R, Wickstead B, Wimperis S. Sodium ions in ordered environments in biological systems: analysis of ^{23}Na NMR spectra. *J. Magn. Reson.* 1999; **140**(2): 351–362.

86. Navon G, Shinar H, Eliav U, Seo Y. Multiquantum filters and order in tissues. *NMR Biomed.* 2001; **14**(2): 112–132.

87. Rooney WD, Springer CS Jr. A comprehensive approach to the analysis and interpretation of the resonances of spins 3/2 from living systems. *NMR Biomed.* 1991; **4**(5): 209–226.

88. Rooney WD, Springer CS Jr. The molecular environment of intracellular sodium: ^{23}Na NMR relaxation. *NMR Biomed.* 1991; **4**(5): 227–245.

89. Hilal SK, Maudsley AA, Simon HE, Perman WH, Bonn J, Mawad ME, Silver AJ, Ganti SR, Sane P, Chien IC. *In vivo* NMR imaging of tissue sodium in the intact cat before and after acute cerebral stroke. *AJNR Am. J. Neuroradiol.* 1983; **4**(3): 245–249.

90. Hilal SK, Maudsley AA, Ra JB, Simon HE, Roschmann P, Wittekoek S, Cho ZH, Mun SK. *In vivo* NMR imaging of sodium-23 in the human head. *J. Comput. Assist. Tomogr.* 1985; **9**(1): 1–7.

91. Maudsley AA, Hilal SK. Biological aspects of sodium-23 imaging. *Br. Med. Bull.* 1984; **40**(2): 165–166.

92. van der Maarel JRC. Relaxation of spin $S = 3/2$ in the doubly rotating tilted frame. *J. Chem. Phys.* 1989; **91**(3): 1446.

93. Eliav U, Navon G. Analysis of double-quantum-filtered NMR spectra of ^{23}Na in biological tissues. *J. Magn. Reson.* 1994; **B103**(1): 19–29.

94. van der Maarel JRC. Relaxation of spin 3/2 in a non-zero average electric field gradient. *Chem. Phys. Lett.* 1989; **155**: 288–296.

95. Woessner DE, Bansal N. Temporal characteristics of NMR signals from spin 3/2 nuclei of incompletely disordered systems. *J. Magn. Reson.* 1998; **133**: 21–35.

96. Chun-wa C, Wimperis S. Optimum detection of spin–3/2 biexponential relaxation using multiple-quantum filtration techniques. *J. Magn. Reson.* 1990; **88**(2): 440.

97. Muller N, Bodenhausen G, Ernst RR. Relaxation-induced violations of coherence transfer selection rules in nuclear magnetic resonance. *J. Magn. Reson.* 1987; **75**(2): 297.

98. Redfield AG. On the theory of relaxation processes. *IBM J. Res. Devl.* 1957; **1**(1): 19.

99. Redfield AG. The theory of relaxation processes. In *Advances in Magnetic Resonance*, Waugh JS (ed.), Vol. 1. Academic Press: New York, 1965; 1–32.

100. Hubbard PS. Nonexponential relaxation of rotating three-spin systems in molecules of a liquid. *J. Chem. Phys.* 1970; **52**(2): 563–568.

101. Pekar J, Leigh JS Jr. Detection of biexponential relaxation in sodium-23 facilitated by double-quantum filtering. *J. Magn. Reson.* 1986; **69**(3): 582.

102. Pekar J, Renshaw PF, Leigh JS Jr. Selective detection of intracellular sodium by coherence-transfer NMR. *J. Magn. Reson.* 1987; **72**(1): 159.

103. Eliav U, Shinar H, Navon G. The formation of a second-rank tensor in ^{23}Na double-quantum-filtered NMR as an indicator for order in a biological tissue. *J. Magn. Reson.* 1992; **98**(1): 223.

104. Reddy R, Bolinger L, Shinnar M, Noyszewski E, Leigh JS. Detection of residual quadrupolar interaction in human skeletal muscle and brain *in vivo* via multiple quantum filtered sodium NMR spectra. *Magn. Reson. Med.* 1995; **33**(1): 134.

105. Shinar H, Knubovets T, Eliav U, Navon G. Sodium interaction with ordered structures in mammalian red blood cells detected by Na-23 double quantum NMR. *Biophys. J.* 1993; **64**(4): 1273.

106. Reddy R, Shinnar M, Wang Z, Leigh JS. Multiple-quantum filters of spin-3/2 with pulses of arbitrary flip angle. *J. Magn. Reson., Ser. B* 1994; **104**(2): 148.

107. Reddy R, Shuchun L, Noyszewski EA, Kneeland JB, Leigh JSf. *In vivo* sodium multiple quantum spectroscopy of human articular cartilage. *Magn. Reson. Med.* 1997; **38**(2): 207.

108. Kemp-Harper R, Brown SP, Hughes CE, Styles P, Wimperis S. ^{23}Na NMR methods for selective observation of sodium ions in ordered environments. *Prog. Nucl. Magn. Reson. Spectrosc.* 1997; **30**(3–4): 157.

109. Borthakur A, Shapiro EM, Beers J, Kudchodkar S, Kneeland JB, Reddy R. Effect of IL-1beta-induced macromolecular depletion on residual quadrupolar interaction in articular cartilage. *J. Magn. Reson. Imag.* 2002; **15**(3): 315–323.

110. Kemp-Harper R, Wimperis S. Detection of the interaction of sodium ions with ordered structures in biological systems. Use of the Jeener–Broekaert experiment. *J. Magn. Reson. Ser. B* 1993; **102**(3): 326.

111. Hancu I, van der Maarel JRC, Boada FE. Detection of sodium ions in anisotropic environments through spin-lock NMR. *Magn. Reson. Med.* 2002; **47**(1): 68.

112. Eliav U, Keinan-Adamsky K, Navon G. A new method for suppressing the central transition in $I = 3/2$ NMR spectra with a demonstration for ^{23}Na in bovine articular cartilage. *J. Magn. Reson.* 2003; **165**(2): 276–281.

113. Ling W, Jerschow A. Frequency-selective quadrupolar MRI contrast. *Solid St. Nucl. Magn. Reson.* 2006; **29**(1–3): 227–231.

114. Ling W, Jerschow A. Selecting ordered environments in NMR of spin 3/2 nuclei via frequency-sweep pulses. *J. Magn. Reson.* 2005; **176**(2): 234–238.

115. Choy J, Ling W, Jerschow A. Selective detection of ordered sodium signals via the central transition. *J. Magn. Reson.* 2006; **180**(1): 105–109.

116. Thulborn KR, Davis D, Adams H, Gindin T, Zhou J. Quantitative tissue sodium concentration mapping of the growth of focal cerebral tumors with sodium magnetic resonance imaging. *Magn. Reson. Med.* 1999; **41**(2): 351–359.

117. Clayton DB, Lenkinski RE. MR imaging of sodium in the human brain with a fast three-dimensional gradient-recalled-echo sequence at 4 T. *Acad. Radiol.* 2003; **10**(4): 358–365.

118. Bartha R, Menon RS. Long component time constant of ^{23}Na T_2^* relaxation in healthy human brain. *Magn. Reson. Med.* 2004; **52**(2): 407–410.

119. Boada FE, Laverde G, Jungreis C, Nemoto E, Tanase C, Hancu I. Loss of cell ion homeostasis and cell viability in the brain: what sodium MRI can tell us. *Curr. Top. Devl. Biol.* 2005; **70**: 77–101.

120. Stobbe R, Beaulieu C. *In vivo* sodium magnetic resonance imaging of the human brain using soft inversion recovery fluid attenuation. *Magn. Reson. Med.* 2005; **54**(5): 1305–1310.

121. Duvvuri U, Leigh JS, Reddy R. Detection of residual quadrupolar interaction in the human breast *in vivo* using sodium-23 multiple quantum spectroscopy. *J. Magn. Reson. Imag.* 1999; **9**(3): 391–394.

122. Navon G. Complete elimination of the extracellular ^{23}Na NMR signal in triple quantum filtered spectra of rat hearts in the presence of shift reagents. *Magn. Reson. Med.* 1993; **30**(4): 503–506.

123. Neuberger T, Greiser A, Nahrendorf M, Jakob PM, Faber C, Webb AG. ^{23}Na microscopy of the mouse heart in vivo using density-weighted chemical shift imaging. *Magma* 2004; **17**(3–6): 196–200.

124. Pabst T, Sandstede J, Beer M, Kenn W, Neubauer S, Hahn D. Evaluation of sodium T_1 relaxation times in human heart. *J. Magn. Reson. Imag.* 2003; **17**(6): 726–729.

125. Pabst T, Sandstede J, Beer M, Kenn W, Greiser A, von Kienlin M, Neubauer S, Hahn D. Optimization of ECG-triggered 3D (23)Na MRI of the human heart. *Magn. Reson. Med.* 2001; **45**(1): 164–166.

126. Bottomley PA, Lee RF, Constantinides CD, Ouwerkerk R, Weiss RG. Quantification and imaging of myocardial sodium and creatine kinase metabolites. *Magma* 2000; **11**(1–2): 39–41.

127. Constantinides CD, Kraitchman DL, O'Brien KO, Boada FE, Gillen J, Bottomley PA. Noninvasive quantification of total sodium concentrations in acute reperfused myocardial infarction using ^{23}Na MRI. *Magn. Reson. Med.* 2001; **46**(6): 1144–1151.

128. Babsky A, Hekmatyar S, Wehrli S, Doliba N, Osbakken M, Bansal N. Influence of ischemic preconditioning on intracellular sodium, pH, and cellular energy status in isolated perfused heart. *Exp. Biol. Med. (Maywood)* 2002; **227**(7): 520–528.

129. Bansal N, Szczepaniak L, Ternullo D, Fleckenstein JL, Malloy CR. Effect of exercise on (23)Na MRI and relaxation characteristics of the human calf muscle. *J. Magn. Reson. Imag.* 2000; **11**(5): 532–538.

130. Constantinides CD, Gillen JS, Boada FE, Pomper MG, Bottomley PA. Human skeletal muscle: sodium MR imaging and quantification-potential applications in exercise and disease. *Radiology* 2000; **216**(2): 559–568.

131. Aronen HJ, Ramadan UA, Peltonen TK, Markkola AT, Tanttu JI, Jaaskelainen J, Hakkinen AM, Sepponen R. 3D spin-lock imaging of human gliomas. *Magn. Reson. Imag.* 1999; **17**(7): 1001–1010.

132. Kline RP, Wu EX, Petrylak DP, Szabolcs M, Alderson PO, Weisfeldt ML, Cannon P, Katz J. Rapid *in vivo* monitoring of

chemotherapeutic response using weighted sodium magnetic resonance imaging. *Clin. Cancer Res.* 2000; **6**(6): 2146–2156.

133. Schepkin VD, Ross BD, Chenevert TL, Rehemtulla A, Sharma S, Kumar M, Stojanovska J. Sodium magnetic resonance imaging of chemotherapeutic response in a rat glioma. *Magn. Reson. Med.* 2005; **53**(1): 85–92.

134. Reddy R, Insko EK, Leigh JS. Triple quantum sodium imaging of articular cartilage. *Magn. Reson. Med.* 1997; **38**(2): 279–284.

135. Duvvuri U, Kaufman JH, Patel SD, Bolinger L, Kneeland JB, Leigh JS, Reddy R. Sodium multiple quantum spectroscopy of articular cartilage: effects of mechanical compression. *Magn. Reson. Med.* 1998; **40**(3): 370–375.

136. Lesperance LM, Gray ML, Burstein D. Determination of fixed charge-density in cartilage using nuclear-magnetic–resonance. *J. Orthoped. Res.* 1992; **10**(1): 1–13.

137. Borthakur A. *Sodium NMR: a Noninvasive Probe for Proteoglycan Macromolecules*. University of Pennsylvania: Philadelphia, PA, 2000.

138. Horn M. ^{23}Na magnetic resonance imaging for the determination of myocardial viability: the status and the challenges. *Curr. Vasc. Pharmac.* 2004; **2**(4): 329–333.

139. Kohler SJ, Kolodny NH. Sodium magnetic resonance imaging and chemical shift imaging. *Progr. Nucl. Magn. Reson. Spectrosc.* 1992; **24**: 411.

140. Rooney WD, Springer CS, Jr. The molecular environment of intracellular sodium: ^{23}Na NMR relaxation. *NMR Biomed.* 1991; **4**(5): 227.

141. Shapiro E. *Multi-nuclear magnetic resonance methods for evaluating cartilage degeneration*. University of Pennsylvania: Philadelphia, PA, 2001.

142. Reddy R, Insko EK, Leigh JS. Triple quantum sodium imaging of articular cartilage. *Magn. Reson. Med.* 1997; **38**(2): 279–284.

143. Borthakur A, Hancu I, Boada FE, Shen GX, Shapiro EM, Reddy R. *In vivo* triple quantum filtered twisted projection sodium MRI of human articular cartilage. *J. Magn. Reson.* 1999; **141**(2): 286–290.

144. Kemp-Harper R, Wickstead B, Wimperis S. Sodium ions in ordered environments in biological systems: analysis of ^{23}Na NMR spectra. *J. Magn. Reson.* 1999; **140**(2): 351.

145. Maroudas A, Muir H, Wingham J. The correlation of fixed negative charge with glycosaminoglycan content of human articular cartilage. *Biochim Biophys Acta* 1969; **177**(3): 492–500.

146. Paul PK, O'Byrne EM, Gupta RK, Jelicks LA. Detection of cartilage degradation with sodium NMR (letter). *Br. J. Rheumatol.* 1991; **30**: 318.

147. Jelicks LA, Paul PK, O'Byrne E, Gupta RK. H-1, Na-23, and C-13 MR spectroscopy of cartilage degradation *in vitro*. *J. Magn. Reson. Imag.* 1993; **3**(4): 565–568.

148. Insko EK, Kaufman JH, Leigh JS, Reddy R. Sodium NMR evaluation of articular cartilage degradation. *Magn. Reson. Med.* 1999; **41**: 30–34.

149. Granot J. Sodium imaging of human body organs and extremities *in vivo*. *Radiology* 1988; **167**: 547–550.

150. Kaufman JH, Regatte RR, Bolinger L, Kneeland JB, Reddy R, Leigh JS. A novel approach to observing articular cartilage deformation *in vitro* via magnetic resonance imaging. *J. Magn. Reson. Imag.* 1999; **9**(5): 653–662.

151. Borthakur A, Shapiro EM, Beers J, Kudchodkar S, Kneeland JB, Reddy R. Sensitivity of MRI to proteoglycan depletion in cartilage: comparison of sodium and proton MRI. *Osteoarthritis Cartilage* 2000; **8**(4): 288–293.

152. Shapiro EM, Borthakur A, Gougoutas A, Reddy R. ^{23}Na MRI accurately measures FCD in articular cartilage. *Magn. Reson. Med.* 2002; **47**(2): 284–291.

153. Borthakur A, Shapiro EM, Akella SV, Gougoutas A, Kneeland JB, Reddy R. Quantifying sodium in the human wrist *in vivo* by using MR imaging. *Radiology* 2002; **224**: 598–602.

154. Wheaton AJ, Borthakur A, Dodge GR, Kneeland JB, Schumacher HR, Reddy R. Sodium magnetic resonance imaging of proteoglycan depletion in an *in vivo* model of osteoarthritis. *Acad Radiol.* 2004; **11**(1): 21–28.

155. Burstein D, Velyvis J, Scott KT, Stock KW, Kim YJ, Jaramillo D, Boutin RD, Gray ML. Protocol issues for delayed Gd(DTPA)$^{2-}$-enhanced MRI (dGEMRIC) for clinical evaluation of articular cartilage. *Magn. Reson. Med.* 2001; **45**(1): 36–41.

156. Pruessmann KP, Weiger M, Scheidegger MB, Boesiger P. SENSE: sensitivity encoding for fast MRI. *Magn. Reson. Med.* 1999; **42**(5): 952–962.

157. Sodickson DK, Manning WJ. Simultaneous acquisition of spatial harmonics (SMASH): fast imaging with radiofrequency coil arrays. *Magn. Reson. Med.* 1997; **38**(4): 591–603.

158. Hoult DI, Chen CN, Sank VJ. The field dependence of NMR imaging. II. Arguments concerning an optimal field strength. *Magn. Reson. Med.* 1986; **3**(5): 730–746.

159. Chen CN, Sank VJ, Cohen SM, Hoult DI. The field dependence of NMR imaging. I. Laboratory assessment of signal-to-noise ratio and power deposition. *Magn. Reson. Med.* 1986; **3**(5): 722–729.

160. Wen H, Chesnick AS, Balaban RS. The design and test of a new volume coil for high field imaging. *Magn. Reson. Med.* 1994; **32**(4): 492–498.

161. Ugurbil K, Adriany G, Andersen P, Chen W, Garwood M, Gruetter R, Henry PG, Kim SG, Lieu H, Tkac I, Vaughan T, Van De Moortele PF, Yacoub E, Zhu XH. Ultrahigh field magnetic resonance imaging and spectroscopy. *Magn. Reson. Imag.* 2003; **21**(10): 1263–1281 .

162. Wolff SD, Balaban RS. Magnetization transfer contrast (MTC) and tissue water proton relaxation *in vivo*. *Magn. Reson. Med.* 1989; **10**(1): 135–144.

163. Rommel E, Kimmich R, Korperich H, Kunze C, Gersonde K. $T_{1\rho}$ dispersion imaging and localized $T_{1\rho}$ dispersion relaxometry: application *in vivo* to mouse adenocarcinoma. *Magn. Reson. Med.* 1992; **24**(1): 149–157.

164. Santyr GE, Fairbanks EJ, Kelcz F, Sorenson JA. Off-resonance spin locking for MR imaging. *Magn. Reson. Med.* 1994; **32**(1): 43–51.

165. Charagundla SR, Stolpen AH, Leigh JS, Reddy R. Off-resonance proton T_{1r} dispersion imaging of ^{17}O-enriched tissue phantoms. *Magn. Reson. Med.* 1998; **39**(4): 588–595.

166. Palmer AG, 3rd, Kroenke CD, Loria JP. Nuclear magnetic resonance methods for quantifying microsecond-to-millisecond motions in biological macromolecules. *Meth. Enzymol.* 2001; **339**: 204–238.

167. Bull TE. Relaxation in the rotating frame in liquids. *Prog. NMR Spectrosc.* 1992; **24**: 377.

168. Kimmich R. Nuclear magnetic relaxation spectroscopy in solutions of bovine hemoglobin. *Z. Naturforsch. B* 1971; **266**(11): 1168–1170.

169. Santyr GE, Henkelman RM, Bronskill MJ. Spin locking for magnetic resonance imaging with application to human breast. *Magn. Reson. Med.* 1989; **12**(1): 25–37.

170. Lamminen AE, Tanttu JI, Sepponen RE, Pihko H, Korhola OA. T_{1r} dispersion imaging of diseased muscle tissue. *Br. J. Radiol.* 1993; **66**(789): 783–787.

171. Dixon WT, Oshinski JN, Trudeau JD, Arnold BC, Pettigrew RI. Myocardial suppression *in vivo* by spin locking with composite pulses. *Magn. Reson. Med.* 1996; **36**(1): 90–94.

172. Markkola AT, Aronen HJ, Paavonen T, Hopsu E, Sipila LM, Tanttu JI, Sepponen RE. $T_{1\rho}$ dispersion imaging of head and neck tumors: a comparison to spin lock and magnetization transfer techniques. *J. Magn. Reson. Imag.* 1997; **7**(5): 873–879.

173. Mlynarik V, Trattnig S, Huber M, Zembsch A, Imhof H. The role of relaxation times in monitoring proteoglycan depletion in articular cartilage. *J. Magn. Reson. Imag.* 1999; **10**(4): 497–502.

174. Grohn OHJ, Kettunen MI, Makela HI, Penttonen M, Pitkanen A, Lukkarinen JA, Kauppinen RA. Early detection of irreversible cerebral ischemia in the rat using dispersion of the magnetic resonance imaging relaxation time, $T_{1\rho}$. *J. Cereb. Blood Flow Metab.* 2000; **20**(10): 1457–1466.

175. Poptani H, Duvvuri U, Miller CG, Mancuso A, Charagundla S, Fraser NW, Glickson JD, Leigh JS, Reddy R. $T_{1\rho}$ imaging of murine brain tumors at 4 T. *Acad. Radiol.* 2001; **8**(1): 42–47.

176. Borthakur A, Wheaton AJ, Gougoutas AJ, Akella SV, Regatte RR, Charagundla SR, Reddy R. In vivo measurement of $T_{1\rho}$ dispersion in the human brain at 1.5 tesla. *J. Magn. Reson. Imag.* 2004; **19**(4): 403–409.

177. Wheaton AJ, Casey FL, Gougoutas AJ, Dodge GR, Borthakur A, Lonner JH, Schumacher HR, Reddy R. Correlation of $T_{1\rho}$ with fixed charge density in cartilage. *J. Magn. Reson. Imag.* 2004; **20**(3): 519–525.

178. Hulvershorn J, Borthakur A, Bloy L, Gualtieri EE, Reddy R, Leigh JS, Elliott MA. $T_{1\rho}$ contrast in functional magnetic resonance imaging. *Magn. Reson. Med.* 2005; **54**(5): 1155–1162.

179. Johannessen W, Auerbach JD, Wheaton AJ, Kurji A, Borthakur A, Reddy R, Elliott DM. Assessment of human disc degeneration and proteoglycan content using $T_{1\rho}$-weighted magnetic resonance imaging. *Spine* 2006; **31**(11): 1253–1257.

180. Borthakur A, Wheaton AJ, Charagundla SR, Shapiro EM, Regatte RR, Akella SVS, Kneeland JB, Reddy R. Three-dimensional $T_{1\rho}$-weighted MRI at 1.5 Tesla. *J. Magn. Reson. Imag.* 2003; **17**(6): 730–736.

181. Wheaton AJ, Borthakur A, Charagundla SR, Reddy R. Pulse sequence for multislice $T_{1\rho}$-weighted MRI. *Magn. Reson. Med.* 2004; **51**(2): 362–369.

182. Wheaton AJ. *Quantitative Spin-lock Magnetic Resonance Imaging: Technical Development and Biomedical Applications.* University of Pennsylvania: Philadelphia, PA 2005.

183. Li X, Han ET, Ma CB, Link TM, Newitt DC, Majumdar S. In vivo 3T spiral imaging based multi-slice T(1rho) mapping of knee cartilage in osteoarthritis. *Magn. Reson. Med.* 2005; **54**(4): 929–936.

184. Schmitz B, Hagen T, Reith W. Three-dimensional true FISP for high-resolution imaging of the whole brain. *Eur. Radiol.* 2003; **13**(7): 1577–1582.

185. Collins CM, Li S, Smith MB. SAR and B_1 field distributions in a heterogeneous human head model within a birdcage coil. *Magn. Reson. Med.* 1998; **40**(6): 847–856.

186. Wheaton AJ, Borthakur A, Corbo M, Charagundla SR, Reddy R. Method for reduced SAR $T_{1\rho}$-weighted MRI. *Magn. Reson. Med.* 2004; **51**(6): 1096–1102.

187. Wheaton AJ, Borthakur A, Reddy R. Application of the keyhole technique to $T_{1\rho}$ relaxation mapping. *J. Magn. Reson. Imag.* 2003; **18**(6): 745–749.

188. Redfield AG. Nuclear magnetic resonance saturation and rotary saturation in solids. *Phys. Rev.* 1955; **98**(6): 1787.

189. Redfield AG. Nuclear spin thermodynamics in the rotating frame. *Science* 1969; **164**(3883): 1015.

190. Koenig SH, Brown RD, III. Field-cycling relaxometry of protein solutions and tissue. Implications for MRI. *Prog. NMR Spectrosc.* 1990; **22**(pt 6): 487.

191. Kelly SW, Sholl CA. A relationship between nuclear spin relaxation in the laboratory and rotating frames for dipolar and quadrupolar relaxation. *J. Phys.: Condensed Matter* 1992; **4**(12): 3317.

192. Knispel RR. NMR study of the two-phase equilibrium in cysteine hydrochloride monohydrate. II. *J. Chem. Phys.* 1974; **61**(3): 1125.

193. Meiboom S, Hewitt RC. High resolution NMR probe suitable for use in a superconducting solenoid. *Rev. Sci. Instrum.* 1965; **36**(10): 1509.

194. Carver JP, Richards RE. A general two-site solution for the chemical exchange produced dependence of T_2 upon the Carr-Purcell pulse separation. *J. Magn. Reson.* 1972; **6**(1): 89.

195. Allerhand A, Gutowsky HS. Spin-echo studies of chemical exchange. II. Closed formulas for two sites. *J. Chem. Phys.* 1965; **42**(5): 587.

196. Stevens A, Paschalis P, Schleich T. Sodium-23 and potassium-39 nuclear magnetic resonance relaxation in eye lens. Examples of quadrupole ion magnetic relaxation in a crowded protein environment. *Biophys. J.* 1992; **61**(5): 1061.

197. Chopra S, McClung RED, Jordan RB. Rotating-frame relaxation rates of solvent molecules in solutions of paramagnetic ions undergoing solvent exchange. *J. Magn. Reson.* 1984; **59**(3): 361.

198. Belton PS, Ring SG, Botham RL, Hills BP. Multinuclear NMR studies of water in solutions of simple carbohydrates. II. Oxygen-17 relaxation. *Mol. Phys.* 1991; **72**(5): 1123–1134.

199. Hills BP, Wright KM, Belton PS. Proton NMR studies of chemical and diffusive exchange in carbohydrate systems. *Mol. Phys.* 1989; **67**(6): 1309–1326.

200. Hills BP, Takacs SF, Belton PS. The effects of proteins on the proton NMR transverse relaxation time of water. II. Protein aggregation. *Mol. Phys.* 1989; **67**(4): 919–937.

201. Hills BP, Takacs SF, Belton PS. The effects of proteins on the proton NMR transverse relaxation times of water. I. Native bovine serum albumin. *Mol. Phys.* 1989; **67**(4): 903–918.

202. Hills BP, Duce SL. The influence of chemical and diffusive exchange on water proton transverse relaxation in plant tissues. *Magn. Reson. Imag.* 1990; **8**(3): 321–331.

203. Hills BP. Multinuclear NMR studies of water in solutions of simple carbohydrates. I. Proton and deuterium relaxation. *Mol. Phys.* 1991; **72**(5): 1099–1121.

204. Virta A, Komu M, Kormano M. $T_{1\rho}$ of protein solutions at very low fields: dependence on molecular weight, concentration, and structure. *Magn. Reson. Med.* 1997; **37**(1): 53–57.

205. Virta A, Komu M, Lundbom N, Jaaskelainen S, Kalimo H, Airio A, Alanen A, Kormano M. Low field $T_{1\rho}$ imaging of myositis. *Magn. Reson. Imag.* 1998; **16**(4): 385–391.

206. Trott O, Palmer AG, III. R1rho relaxation outside of the fast-exchange limit. *J. Magn. Reson.* 2002; **154**(1): 157.

207. Trott O, Abergel D, Palmer AG, III. An average-magnetization analysis of R1rho relaxation outside of the fast exchange limit. *Mol. Phys.* 2003; **101**(6): 753.

208. Mlynarik V, Szomolanyi P, Toffanin R, Vittur F, Trattnig S. Transverse relaxation mechanisms in articular cartilage. *J. Magn. Reson.* 2004; **169**(2): 300–307.

209. Reddy R, Stolpen AH, Leigh JS. Detection of ^{17}O by proton T_{1r} dispersion imaging. *J. Magn. Reson. B* 1995; **108**(3): 276–279.

210. Solomon I. Magnetic relaxation in liquids in the presence of a high frequency field. *C. R. Hebdomad. Seances Acad. Sci.* 1959; **249**(17): 1631.

211. Tsoref L, Shinar H, Seo Y, Eliav U, Navon G. Proton double-quantum filtered MRI—a new method for imaging ordered tissues. *Magn. Reson. Med.* 1998; **40**(5): 720–726.

212. Chaumette H, Grandclaude D, Brondeau J, Werbelow L, Canet D. Rotating-frame spin-lattice relaxation measurements $T_{1\rho}$ with weak spin–locking fields in the presence of homonuclear dipolar coupling. *Mol. Phys.* 2003; **101**(12): 1919.

213. Chaumette H, Grandclaude D, Brondeau J, Werbelow L, Canet D. Rotating-frame spin-lattice relaxation measurements $T_{1\rho}$ with weak spin-locking fields in the presence of homonuclear dipolar coupling. *Molecular Physics* 2003; **101**: 1919.

214. Akella SV, Regatte RR, Wheaton AJ, Borthakur A, Reddy R. Reduction of residual dipolar interaction in cartilage by spin-lock technique. *Magn. Reson. Med.* 2004; **52**(5): 1103–1109.

215. Xia Y. Relaxation anisotropy in cartilage by NMR microscopy (μMRI) at 14-μm resolution. *Magn. Reson. Med.* 1998; **39**(6): 941–949.

216. Rubenstein JD, Kim JK, Henkelman RM. Effects of compression and recovery on bovine articular cartilage: appearance on MR images. *Radiology* 1996; **201**(3): 843–850.

217. Mlynarik V, Degrassi A, Toffanin R, Vittur F, Cova M, Pozzi-Mucelli RS. Investigation of laminar appearance of articular cartilage by means of magnetic resonance microscopy. *Magn. Reson. Imag.* 1996; **14**(4): 435–442.

218. Regatte RR, Akella SV, Borthakur A, Kneeland JB, Reddy R. Proteoglycan depletion-induced changes in transverse relaxation maps of cartilage: comparison of T_2 and $T_{1\rho}$. *Acad. Radiol.* 2002; **9**(12): 1388–1394.

219. Menezes NM, Gray ML, Hartke JR, Burstein D. T_2 and $T_{1\rho}$ MRI in articular cartilage systems. *Magn. Reson. Med.* 2004; **51**(3): 503–509.

220. Shinar H, Keinan-Adamsky K, Navon G. The biexponential nature of T_2 decay in articular cartilage. In *Proceedings of the International Society of Magnetic Resonance Medicine*, Kyoto, 2004; 2395.

221. Duvvuri U, Goldberg AD, Kranz JK, Hoang L, Reddy R, Wehrli FW, Wand AJ, Englander SW, Leigh JS. Water magnetic relaxation dispersion in biological systems: the contribution of proton exchange and implications for the noninvasive detection of cartilage degradation. *Proc. Natl Acad. Sci. USA* 2001; **98**(22): 12479–12484.

222. Reddy R, Insko EK, Kaufman JH, Bolinger L, Kneeland JB, Leigh JS. MR imaging of cartilage under spin-locking. In

Proceedings of the International Society of Magnetic Resonance Medicine, Nice, 1995; 1535.

223. Duvvuri U, Kudchodkar S, Reddy R, Leigh JS. *T*(1rho) relaxation can assess longitudinal proteoglycan loss from articular cartilage *in vitro*. *Osteoarthritis Cartilage* 2002; **10**(11): 838–844.

224. Mankin HJ, Brandt KD. Biochemistry and metabolism of articular cartilage in osteoarthritis. In *Osteoarthritis: Diagnosis and Medical/surgical Management*, Moskowitz RW, Howell DS, Goldberg VM, Mankin HJ (eds). W. B. Saunders: Philadelphia, PA, 1992; 109–154.

225. Watson PJ, Carpenter TA, Hall LD, Tyler JA. MR protocols for imaging the guinea pig knee. *Magn. Reson. Imag.* 1997; **15**(8): 957–970.

226. Regatte RR, Akella SV, Wheaton AJ, Borthakur A, Kneeland JB, Reddy R. *T*1rho-relaxation mapping of human femoral-tibial cartilage *in vivo*. *J. Magn. Reson. Imag.* 2003; **18**(3): 336–341.

227. Akella SV, Regatte RR, Borthakur A, Kneeland JB, Leigh JS, Reddy R. $T_{1\rho}$ MR imaging of the human wrist *in vivo*. *Acad. Radiol.* 2003; **10**(6): 614–619.

228. Regatte RR, Akella SV, Borthakur A, Kneeland JB, Reddy R. *In vivo* proton MR three-dimensional $T_{1\rho}$ mapping of human articular cartilage: initial experience. *Radiology* 2003; **229**(1): 269–274.

229. Wheaton AJ, Borthakur A, Kneeland JB, Regatte RR, Akella SV, Reddy R. *In vivo* quantification of *T*(1rho) using a multislice spin-lock pulse sequence. *Magn. Reson. Med.* 2004; **52**(6): 1453–1458.

230. Lozano J, Li X, Link TM, Safran M, Majumdar S, Ma CB. Detection of posttraumatic cartilage injury using quantitative $T_{1\rho}$ magnetic resonance imaging. A report of two cases with arthroscopic findings. *J. Bone Joint Surg. Am.* 2006; **88**(6): 1349–1352.

231. Regatte RR, Akella SV, Wheaton AJ, Lech G, Borthakur A, Kneeland JB, Reddy R. 3D-*T*(1rho)-relaxation mapping of articular cartilage; *in vivo* assessment of early degenerative changes in symptomatic osteoarthritic subjects(1). *Acad. Radiol.* 2004; **11**(7): 741–749.

232. Akella SV, Regatte RR, Wheaton A, Borthakur A, Reddy R. Measurement of dipolar oscillations in articular cartilage using spin-lock technique. In *Proceedings of the International Society of Magnetic Resonance Medicine*, Kyoto, 2004; 824.

233. Wheaton AJ, Dodge GR, Elliott DM, Nicoll SB, Reddy R. Quantification of cartilage biomechanical and biochemical properties via $T_{1\rho}$ magnetic resonance imaging. *Magn. Reson. Med.* 2005; **54**(5): 1087–1093.